

MECHANICS AND DYNAMICS OF SERRATED END MILLS

by

ŞÜKRÜ DORUK MERDOL

B. A. Sc. (Mechanical Engineering)
Middle East Technical University, Turkey, 2000

A THESIS SUBMITTED IN PARTIAL FULFILMENT OF
THE REQUIREMENTS FOR THE DEGREE OF

MASTER OF APPLIED SCIENCE

in

THE FACULTY OF GRADUATE STUDIES

MECHANICAL ENGINEERING

We accept this thesis as conforming
to the required standard

THE UNIVERSITY OF BRITISH COLUMBIA

January 2003

© Şükrü Doruk Merdol, 2003

In presenting this thesis in partial fulfilment of the requirements for an advanced degree at the University of British Columbia, I agree that the Library shall make it freely available for reference and study. I further agree that permission for extensive copying of this thesis for scholarly purposes may be granted by the head of my department or by his or her representatives. It is understood that copying or publication of this thesis for financial gain shall not be allowed without my written permission.

Department of MECHANICAL ENGINEERING

The University of British Columbia
Vancouver, Canada

Date 11.02.2003

Abstract

Roughing, semi-finishing and finish milling operations constitute most significant portion in manufacturing aerospace parts. Thermally resistant materials, such as Titanium and Nickel alloys are rough milled using end mills with serrated or wavy profiles on their cutting edges. The serrations must be designed to have a phase shift from one flute to another in order to prevent unstable, self excited chatter vibrations during machining. Finish milling is usually required in peripheral milling of thin aircraft webs with long end mills where the structures are flexible and radial depth of cuts are small. The spindle speed and depth of cut must be selected optimally to avoid both forced and chatter vibrations in order to produce the parts within specified tolerances.

The thesis presents mathematical model of serrated cutter profiles and their influence on chip load, force, torque, power and vibrations. The waves ground on the flutes are represented mathematically by cubic splines. The chip load distribution is predicted by integrating spline representation of flutes and previously developed kinematic model of dynamic milling which considers the structural vibrations. The cutting forces, torque, power, vibrations and surface form errors are predicted using time domain solution of the process.

The chatter vibration stability is studied both in time and frequency domain when the radial immersion is small in milling operations. The physics behind the use of average and multiple harmonics of directional coefficients are explained in frequency domain solution of stability lobes. It is shown that multiple harmonics of the directional factors predict extra stability lobes at odd multiples of half tooth passing frequencies. The analytical solution favorably is verified by exact,

time domain solution of the dynamic problem. The solution is also compared against specially designed milling experiments.

Table of Contents

Abstract	ii
Table of Contents	iv
List of Tables	vii
List of Figures	viii
Acknowledgment	xi
Nomenclature	xii
1. Introduction	1
2. Literature Review	3
2.1.Overview	3
2.2.Kinematics of Milling	3
2.3.Modeling of Milling Forces	5
2.4.Serrated Cutters	6
2.5.Chatter Stability	8
3. Multi Frequency Chatter Stability in Milling Operations	23
3.1.Introduction	23
3.2.Dynamics of Milling	26

3.3.Formulation of Stability Equation	30
3.4.Solution of Stability Equation	37
3.5.Simulations	41
3.5.1.Low Radial Width of Cut I (One Dimensional - Y only)	42
3.5.2.Low Radial Width of Cut II (One Dimensional - X only)	53
3.6.Further Analysis on Number of Harmonics	60
4. Geometric Modeling of Serrated Cutters	63
4.1.Introduction	63
4.2.Serrated Cutter with Straight Flutes	63
4.3.Serrated Cutter with Helical Flutes	71
4.4.Tapered Helical Ball End Mill with Serrated Flutes	77
4.4.1. Constant Helix Case	78
4.4.2. Constant Lead Case	89
5. Modeling of Milling Forces	91
5.1.Introduction	91
5.2.Mechanics of Milling	92
5.3.Linear-Edge Force Model	95
5.4.Cutting Force Coefficient Identification	95
5.5.Orthogonal to Oblique Cutting Transformation	97
5.6.Mechanics of Milling with Serrated Cutters	99
5.7.Experimental Verification of Cutting Forces	101

5.8.Chatter Stability	106
5.9.Experimental Verification of Chatter Stability	112
Conclusions	118
Future Research Directions	120
Bibliography	121

List of Tables

3.1 :Spindle Speed vs Number of Harmonics.	62
5.1 :Cutters Used for Experimental Verification.	102
5.2 :Dynamic Parameters in X and Y Directions.	114

List of Figures

2.1 :Types of Milling Operations: (a) Up Milling, (b) Down Milling, (c) Face Milling.	4
2.2 :Picture of a Cylindrical Serrated Cutter.	8
2.3 :Wave Generation in Turning.	9
2.4 :A Regular Cutter.	12
2.5 :Dynamic Modeling for Milling.	15
2.6 :Vibration Frequencies [44].	18
2.7 :Power Spectra of Experimental Microphone Signals, Hopf Bifurcation, Unstable.	21
2.8 :Power Spectra of Experimental Microphone Signals, Flip Bifurcation, Unstable.	21
3.1 :A Single-Degree-of-Freedom Vibration System.	25
3.2 :Dynamics of Milling.	27
3.3 :Switching Function.	30
3.4 :Directional Coefficient $a_{xx} \cdot \phi_{st} = 153^\circ$, $\phi_{ex} = 180^\circ$, $N=3$, $n=10000$ rpm, $K_r = 0.3$.	39
3.5 :Flow Chart of Multi Frequency Solution.	40
3.6 :Real Part of Transfer Function and Its First Harmonics.	41
3.7 :Low Radial Immersion Milling.	43
3.8 :Stability Lobes for Low Immersion Down Milling.	44
3.9 :New Stability Pocket, Comparison of Time and Frequency Domain Results.	45
3.10 :Time Domain Simulation of Cutting Force and Tool Vibration in Y Direction, Point A: $n=30000$ rpm, $a=2$ mm, Unstable.	47
3.11 :Time Domain Simulation of Cutting Force and Tool Vibration in Y Direction, Point B: $n=34000$ rpm, $a=3$ mm, Stable.	48
3.12 :Time Domain Simulation of Cutting Force and Tool Vibration in Y Direction, Point C: $n=38000$ rpm, $a=2$ mm, Unstable.	49

3.13 :Real and Imaginary Parts of Transfer Function, $hr=3$, 30000 rpm.	52
3.14 :Real and Imaginary Parts of Transfer Function, $hr=3$, 38000 rpm.	53
3.15 :Low Immersion Centre Milling.	54
3.16 :Stability Lobes by Stepan & Bayly et al. [44].	55
3.17 :Comparison of Stability Lobes.	55
3.18 :Time Domain Simulation of Cutting Force and Tool Vibration in X Direction, Point A: $n=3200$ rpm, $a=2.5$ mm, Unstable.	57
3.19 :Time Domain Simulation of Cutting Force and Tool Vibration in X Direction, Point B: $n=3540$ rpm, $a=2.5$ mm, Stable.	58
3.20 :Time Domain Simulation of Cutting Force and Tool Vibration in X Direction, Point C: $n=3600$ rpm, $a=2.5$ mm, Unstable.	59
3.21:Real Part of Transfer Function and Its Harmonics at 36897 rpm	61
4.1 :Typical Serrated Cutter Tooth Profile.	64
4.2 :Clamped Spline Examples.	69
4.3 :Representation of a Straight Flute Milling Cutter.	70
4.4 :Angle Representations.	71
4.5 :Important Vectors for Mathematical Model of a Cylindrical Cutter.	72
4.6 :Simulated Cylindrical, Helical Serrated Cutter.	74
4.7 :Schematic Representation of κ Angle.	75
4.8 :Constant Lead, Constant Helix Tapered End Mills.	78
4.9 :Serrated Tapered Ball End Mill.	80
4.10 :Vector Definitions for Tapered Cutters.	83
4.11 :Representation of $\vec{\eta}_{rot}$.	85
4.12 :Rotated Spline.	87
5.1 :(a) Milling Operation, (b) General Milling Force Diagram.	92
5.2 :Orthogonal and Oblique Cutting Geometry [25].	97
5.3 :(a) Direction Convention, (b) Force Diagram, Chip Thickness.	100

5.4 :Full Immersion at 1500 rpm, (a) 7 mm Axial Depth of Cut, 0.02 mm/tooth.rev Feed Rate; (b) 8 mm Axial Depth of Cut, 0.08 mm/tooth.rev Feed Rate.	103
5.5 :Half Immersion Down Milling at 1600 rpm, 8 mm Axial Depth of Cut (a) 0.08 mm/tooth.rev Feed Rate; (b) 0.10 mm/tooth.rev Feed Rate.	103
5.6 :Half Immersion Down Milling at 1600 rpm, 0.08 mm/tooth.rev Feed Rate (a) 4 mm Axial Depth of Cut; (b) 6 mm Axial Depth of Cut.	104
5.7 :Full Immersion at 1500 rpm, (a) 7 mm Axial Depth of Cut, 0.02 mm/tooth.rev Feed Rate; (b) 8 mm Axial Depth of Cut, 0.08 mm/tooth.rev Feed Rate.	104
5.8 :Full Immersion, 15 mm Depth of Cut, 0.04 mm/tooth.rev at 1000 rpm.	105
5.9 :Simulated Cutting Forces: 4 Fluted Cylindrical Helical Endmill,1500 rpm, 0.05 mm/ tooth.rev, 10 mm depth of cut.	106
5.10 :Static and Dynamic Chip.	108
5.11 :Flow Chart of Time Domain Simulation.	110
5.12 :Exact Chip Thickness Determination in Time Domain Simulation.	111
5.13 :Spindle Model.	112
5.14 :Transfer Functions Obtained at the Tool Tip.	114
5.15:Measured and Simulated Stability Lobes for 3 Fluted Cylindrical Serrated Endmill, $c=0.04$ mm/rev.tooth, Material: Al 7050, Experimental Results.	116
5.16 :Experimental Results: Force and FFT at 4300 (A) and 5400 rpm (B), $a=10.5$ mm	117
5.17 :Effect of Serrations on Depth of Cut.	117

Acknowledgment

I would like express my gratitude to my research supervisor Dr. Yusuf Altintas for the valuable instruction, guidance, and support which he has provided throughout my research and coursework. I would also like to thank to my friends. First, to my life long friends, thanks for being with me especially during rough times. I have always felt your support despite the geographical differences. Second, to my friends in Canada. Amongst the most special ones, I can name Carmen, Vinay, Kemal and Emre. It was pleasing to have all of you around. You made my studies enjoyable. I am very fortunate to have met all of you. And lastly I want to thank to my friends at MAL. Every single one of you is a brilliant person with excellent skills. You have made me realise that there are many more subjects to be discovered in the field of manufacturing.

Finally, I would like to thank my beloved family for their unwavering support and patience regarding my graduate study abroad and the long absence from my home. I dedicate this work to my mother (Mucella), my father (Erdal), my sister (Asu Ceylan) and especially to my unborn niece/nephew. I wish you a long life in a world where peace is more important than weapons, humanity is more valuable than money, and the value of a human is not measured with his race, language or religion.

“I wish to say such a word

That leaves not one outside ... “

O. Asaf (Turkish Poet)

Nomenclature

a	axial depth of cut
b	radial depth of cut
c	feed rate
D	cutter diameter
G	transfer function
h	instantaneous chip thickness
i_0	helix angle
i_s	nominal helix angle
$[I]$	identity matrix
k	stiffness
K	cutting force coefficient
$lead$	lead of the cutter
n	spindle speed
N	number of teeth
r_c	chip ratio
T	tooth period
z	axial height
α_n	normal rake angle
α_r	rake angle
β	half-apex taper angle
β_a	friction angle
ζ	damping ratio
κ	axial immersion angle
Λ	eigenvalue

Λ_I	imaginary part of eigenvalue
Λ_R	real part of eigenvalue
ϕ	tooth immersion
ϕ_c	shear angle
ϕ_n	normal shear angle
ϕ_o	rotation angle
ϕ_p	pitch angle
ψ	local helix angle
Ω	spindle speed
ω_c	chatter frequency
ω_n	natural frequency
ω_T	tooth passing frequency

Chapter 1

Introduction

Metal cutting is the most dominant type of operation in manufacturing industry. Current manufacturing research is mostly aimed at increasing productivity and developing automated operations. In many of the cases, the rate of production, which is dependent on the cutting conditions, is controlled by trial and error type of methods and the inefficient outcome becomes inevitable. However, satisfactory production rates can easily be achieved by modeling the key aspects of machining operations like dimensional tolerance, machine tool vibrations, tool breakage, positioning accuracy and thermal effects.

Among all different metal cutting techniques, milling is one of the most widely used cutting operation due to its flexibility in producing wide range of shapes from deep pockets on the die and molds to contours on aerospace parts. When high volume machining is considered, such as in aerospace and automotive industries, roughing operation cycle times need to be reduced. The purpose of this research is to investigate and model the mechanics and dynamics of serrated cutters which are used in roughing operations. Main issues related to this problem are the prediction of cutting forces and chatter stability analysis. Both involves comprehensive geometric analysis of the cutting tool as well as the dynamic characteristics of the machine/ cutting tool dynamics.

The thesis investigates mathematical modeling of finish milling operations with small radial depth of cuts, and roughing with serrated cutters.

Chapter 2 is the Literature Review providing necessary background information on milling analysis. The fundamentals of milling process, researches done on serrated cutters, milling process dynamics including time domain chatter stability for serrated cutters and frequency domain stability for low immersion milling operations are discussed.

Chapter 3 discusses Multi Frequency Solution of chatter stability, which is applicable in finish milling operations. The number of tooth passing frequency harmonics involved in the cutting process increases as the radial immersion is decreased. This leads to change of the stability lobe diagram at certain spindle speeds. The Multi Frequency Solution proposed by Budak [1] is analyzed in detail for low immersion milling.

Chapter 4 presents the geometric modeling of serrated cutters. The generalized model enabling design of any serrated cutter is proposed. Simulation results are compared against experimental ones for verification of the proposed analytical model.

In Chapter 5, force modeling, i.e. mechanics of milling is investigated. Linear edge force model as well as orthogonal to oblique transformation method for determination of cutting force coefficients are presented in detail. Moreover, time domain analysis used to construct chatter stability lobes diagram is given. The chapter also includes experimental verification of the proposed models.

The thesis is concluded with a short summary of the main results and contributions.

Chapter 2

Literature Review

2.1. Overview

Milling process is extensively used in manufacturing for metal cutting; therefore, significant amount of work has been done on modelling mechanics and dynamics of milling. In this chapter, literature survey related to the kinematics of milling, mechanics and dynamics of serrated cutters and chatter stability is presented.

2.2. Kinematics of Milling

Milling is an intermittent multi-point cutting operation in which each tooth is in contact with the workpiece for a fraction of one spindle period. The contact time for a tooth is a function of width of cut, spindle speed and the number of teeth. Although in turning, chip thickness is constant, it varies with the angular position of the cutter in milling and follows a trochoidal path as proven by Martellotti [2,3]. There are two different categories of milling operations: peripheral and face milling. Peripheral milling is divided into two cases namely down (climb) and up (conventional) milling. These cases are shown in Figure 2.1. The only difference between these two conditions is the chip thickness variation. In down milling the initial chip thickness, where tool enters into the workpiece, is at its maximum and decreases until it leaves the workpiece at zero chip thickness. However, in up milling, chip thickness increases as cutter rotates. Since cutting forces are proportional to the chip thickness, the main focus of earlier researches were on the chip

formation mechanisms and spindle power estimation [4,5,6,7,8,9]. When rotation angle (ϕ) is defined as angle measured from Y axis in clockwise direction, face milling can be described as a milling operation where entry angle is greater than zero and exit angle is less than 180 degrees.

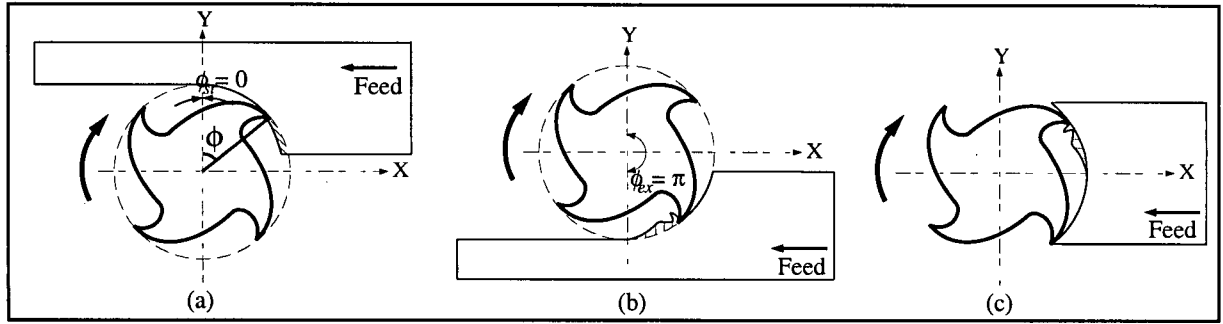


Figure 2.1 : Types of Milling Operations: (a) Up Milling, (b) Down Milling, (c) Face Milling.

Since the trochoidal path modelled by Martellotti is complex to model and computationally costly, the chip thickness can be approximated when radius of the cutter is large compared to the feed as:

$$h(\phi) = c \sin \phi$$

where h is the instantaneous chip thickness, c is the feed rate and ϕ is the tooth immersion angle.

This circular approximation is not sufficient for an accurate prediction of the process during the presence of vibrations and small radial depth of cut. Altintas et al. [10,11,13] contributed significantly to the dynamics of milling operation where true kinematics of milling is considered. During digitization, surface and cutter locations are divided into small elements and kept as separate arrays, exact chip thickness at each flute is determined by finding the difference between

these two surfaces at each time step. Their model fully considers the dynamics of cutter and workpiece as well as the kinematics of chip thickness during milling. The true kinematics model also considers non-linearities such as tool jumping out of the cut, the influence of vibrations, feed and tool geometry.

2.3. Modeling of Milling Forces

Depending on geometry of cutting process, the cutting operations can be classified as orthogonal or oblique. In orthogonal case, cutting edge is straight and the relative velocity of the tool with respect to workpiece is perpendicular to the cutting edge. Due to this perpendicularity, only two orthogonal forces are generated, one in feed direction and the other in tangential direction. Unlike orthogonal case, the cutting edge is inclined with a certain inclination angle which is equal to helix angle for milling cutters in oblique cutting. Oblique angle generates cutting forces in three orthogonal directions. Early research was focused on relating the cutting forces to process dependent parameters such as cutting coefficients, feed rate and axial depth of cut. Tlustý and McNeil [20], Kline et al. [16], Sutherland and DeVor [14] and Montgomery and Altintas [10] have contributed to the modeling of milling forces. In this thesis, linear edge force model used by Armarego and Epp [12] to formulate milling forces is used. Linear edge force model expresses the cutting force as a function of cutting coefficients (K_e, K_c), axial depth of cut (a) and feed rate (c) as:

$$F_{\text{Cutting Force}} = K_e a + K_c a c$$

In order to calculate the cutting forces by using the equation above, the cutting force coefficients need to be known. One of widely studied model for the determination of cutting force coefficients is the mechanistic model [14-17, 20]. The cutting coefficients are evaluated by evaluating cutting forces measured under same immersion but varying feed rates. Linear regression is applied to fit an approximate line to the experimentally measured average forces which leads to identification of cutting forces [18]. Since geometric properties of the cutter such as helix angle, rake angle, relief angle; workpiece material and other variables are all embedded in cutting coefficients, the identified cutting coefficients are only valid for specific cutter and workpiece combination. The identification of cutting coefficients from milling tests is called mechanistic approach.

Another approach in determining the cutting coefficients is based on orthogonal to oblique cutting transformation. In this model, the cutting force coefficients are obtained from orthogonal cutting database and become function of shear stress, shear angle and friction angle [18,19] which are later used for the transformation of orthogonal data to oblique one. During the transformation, tool geometry, cutting conditions such as cutting speed are taken into account; therefore, this method removes all the limits imposed by mechanistic model at the expense of preparation time of necessary orthogonal cutting database.

2.4. Serrated Cutters

Serrated cutters fall under the category of solid end mills which consists of cutters with numerous different geometries such as cylindrical, ball and tapered. An end mill can be either one of these shapes or the combination of them. The most comprehensive work in this field is done by

Engin and Altintas [26] who generalized the geometry of a milling cutter and proposed a unified force modeling methodology.

Serrated cutters differ from conventional end mills in having serrated rather than straight flutes. For example, the diameter of a cylindrical serrated cutter along the helix varies (Figure 2.2) whereas it remains constant for a regular cylindrical end mill. The serration on the flutes leads to increased stability and reduced cutting forces but generates poor surface finish. Therefore, they can be used only in roughing operations. The profile on the flute is periodic, and it has a phase shift from one flute to the other, which leads to non-uniform feed for each tooth at different axial levels of the cutter. At a certain axial height of the cutter, some flute may cut experience large chip load, whereas the others may cut none, hence tool wear for serrated cutters is faster compared to conventional ones.

For regular end mills, there are cases in which the radius of the cutter may change with respect to cutter axis such as in ball end mill and tapered end mill cases. However, this change occurs due to the shape of the envelope, in other words the flute is still kept straight but when it is wrapped around a ball or taper, the radius changes along the cutter axis. The main difference between the serrated cutter and regular end mill is the flute geometry. Unlike in regular end mills, flutes for serrated cutters are not straight but have a certain shape like a sinusoidal curve, hence the geometric modeling of them becomes challenging. It is basically a contour imposed perpendicular to the flute.

Although significant work has been reported in modeling the mechanics and dynamics of milling [21], there has not been many studies on serrated cutters. In their research report, Tlustý, Ismail and Zaton [22] mainly focused on the chatter stability with serrated cutters. They used ser-

rations with straight edges in their analysis. In parallel to this research, Campomanes [23] presented modeling of serrated cutters with only sinusoidal profiles; however, he did not take the effect of full geometry on cutting process into account. Merdol and Altintas [24] generalized the geometry for serrated cutters; therefore, they were able to model any cutter geometry in three dimensional space. This research is presented in this thesis.



Figure 2.2 : Picture of a Cylindrical Serrated Cutter.

2.5. Chatter Stability

There are two types of forces in cutting; static and dynamic. In static case, the system is vibration free and therefore the forces are at steady state. When the structural dynamics are taken into account, cutting forces become time-dependent, harmonic or periodic and contain the effects of vibration. This type of forces is called dynamic forces and they lead to chatter vibrations. Chatter is a self excited type of vibration which occurs in milling due to the dynamic characteristics of

the machine tool, workpiece and cutting process and can be best explained by a phenomenon called regeneration of waviness. When one of the flutes is in cut, due to the dynamics, it starts to leave a wavy surface behind and that wavy surface is cut by the next flute which also vibrates and leaves another wavy surface (see Figure 2.3.). The resulting chip has two waves on each side of the chip which determines its thickness. "Depending on the phase shift between the two successive waves, the maximum chip thickness may exponentially grow while oscillating at a chatter frequency that is close but not equal to a dominant structural mode in the system" [25]. Chatter vibrations leave a wavy and poor surface behind and lead to increased cutting forces which may destroy the workpiece, tool, tool holder and even spindle.

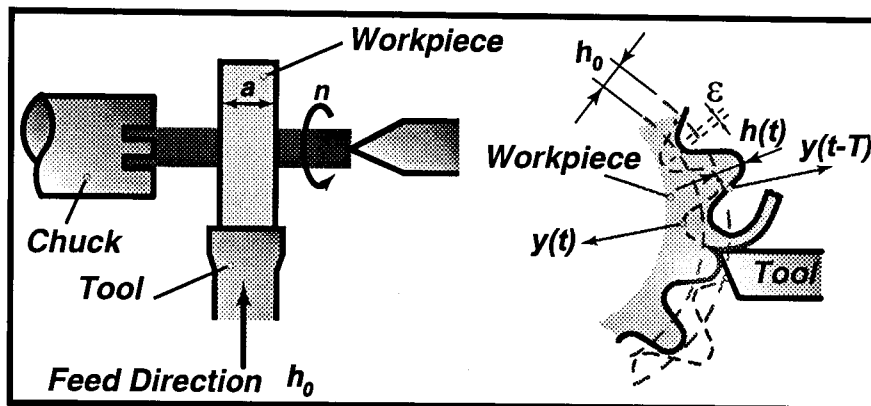


Figure 2.3 : Wave Generation in Turning.

The regeneration phenomenon was first explained by Tlusty [27] and Tobias [28]. Later, Merritt [29] used feedback control theory to verify the theory developed by Tlusty [27] and Tobias [28]. Tobias also developed stability lobes by relating the phase of vibrations to the spindle speed [28]. There are some difficulties in the solution of milling stability like directional coefficients which orient the cutting forces and change the direction of excitation. Tlusty approached this

problem by applying his orthogonal cutting stability formulation to milling with an average directional coefficient as well as an oriented transfer function. He showed the chatter free axial depth of cut as;

$$a_{lim} = \frac{-1}{2K_s \frac{bN}{d^2} G_{min} \alpha} \quad (2.1)$$

where K_s is the cutting coefficient, b is radial depth of cut, N is the number of teeth. The term $G_{min} \alpha$ is the oriented transfer function in the oriented direction. Note that this type of solution is similar to the turning. Two coupled directions were reduced into one directional flexibility with necessary adjustments on the transfer function G as shown in Eq.(2.1).

Minis and Yanushevsky [30] successfully solved the two dimensional milling problem, however this solution was obtained numerically requiring a number of iterations. Later, Budak and Altintas [31] obtained analytical solution for the milling operation. Unlike Tlustý, they used two dimensional structure in their solution and obtained chatter free-axial depth of cut as;

$$a_{lim} = \frac{-2\pi\Lambda_R}{NK_s} \left(1 + \left(\frac{\Lambda_I}{\Lambda_R} \right)^2 \right) \quad (2.2)$$

where K_s is the cutting coefficient, N is the number of teeth. Λ_R and Λ_I are real and imaginary values of Λ which is obtained as an eigenvalue of the following equation:

$$\det\{[I] + \Lambda[G][\alpha]\} = 0 \quad (2.3)$$

where $[G][\alpha]$ is the oriented transfer function of the machine tool and workpiece in feed direction and the one perpendicular to it. Note that this time the solution becomes an eigenvalue solution which is obtained by considering two orthogonal directions.

Lately, Hutton et al. [32] included the gyroscopic effects of the rotating spindle in the solution. Muller optimization algorithm was used to find the eigenvalues of the characteristic equation by specifying an axial depth of cut and rotating speed.

Chatter vibrations for milling operations with serrated cutters have not been studied in detail, however there are few researches focused on this problem. Tlustý, Ismail and Zaton [22] studied the influence of serration on the total axial contact of flutes in cut on chatter stability. In their report, following points were assumed: the milling machine structure shown in Figure 2.4 is uni-directional with a single degree of freedom; the motion of the tool is rectilinear and all teeth are engaged simultaneously in the cut. In the light of these assumptions, they obtained the limit of stability condition for regular end mills as:

$$\frac{Na_{lim}K_s}{k} = \frac{1}{\left| \frac{\vec{Y}}{\vec{F}} \right|} \frac{1}{|\vec{C}|} \quad (2.4)$$

where a_{lim} is the chatter free axial depth of cut, \vec{Y} is the vibration of the tool relative to the workpiece in the current cut, \vec{F} is the cutting force, K_s is the cutting stiffness, N is the number of

teeth, k is the stiffness of the structure and " $|\cdot|$ " designates the length of a vector. Vector \vec{C} for a regular cutter was defined as:

$$\vec{C} = \left[\begin{array}{c} \sum_{i=1}^n \vec{Y}_{oi} \\ \frac{1}{n|\vec{Y}|} - \frac{\vec{Y}}{|\vec{Y}|} \end{array} \right] \quad (2.5)$$

where \vec{Y}_{oi} is the undulation on the surface due to the vibration of the tool relative to the workpiece in the previous cut of tooth i .

Note that, at the limit of stability, vibrations neither increase nor decrease, i.e.

$$|\vec{Y}_{o1}| = |\vec{Y}_{o2}| = \dots = |\vec{Y}_{on}| = |\vec{Y}| \quad (2.6)$$

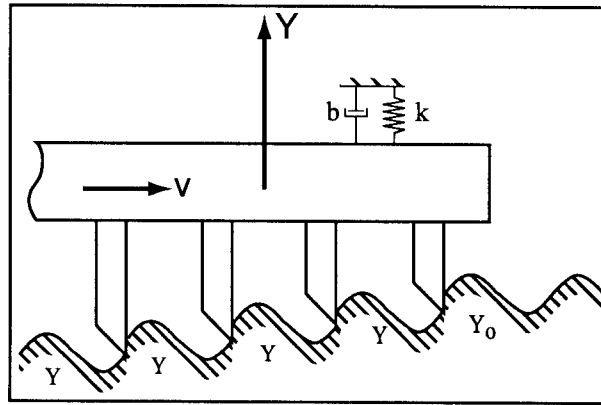


Figure 2.4 : A Regular Cutter.

When a serrated cutter is considered, the flute may not be fully in contact with the workpiece if the chip thickness is smaller than the radial amplitude of serration on the edge. Tlustý et al. proposed that the following modification of vector \vec{C} in Eq.(2.4) would be enough to obtain the stability condition for serrated cutters:

$$\vec{C} = \left[\frac{\sum_{i=1}^{n_t} ss_i \vec{Y}_{oi}}{|\vec{Y}|} - \frac{s^* \vec{Y}}{|\vec{Y}|} \right] \quad (2.7)$$

where n_t is the number of teeth which forms the pattern of the undeformed chip to be cut by one repetitive section and ss_i is an overlapping factor. s^* is equal to apparent over actual depth of cut for one repetitive segment of the profile and defined as $s^* = \sum ss_i$ for $i = 1, n_t$. Unfortunately, there was no generalized formulation provided for the determination of these parameters. Some simulations were run and stability lobes were obtained for serrated cutters. When these lobes were compared with the ones for regular cutters, it was concluded that the increase in stability was in the order of actual over apparent depth of cut ratio.

Later on, Campomanes [23] showed that the chatter stability improves considerably when the straight flutes are replaced by sinusoidally varying serrated cutting edges. He used average cutting force coefficients and approximate chip thickness model as presented by Altintas [25]. In his geometric model, the radial offset of the cutting edge along the cutter axis (z) is defined as:

$$\Delta r_j = A \left(1 - \sin \left(2\pi \left(\frac{z}{\lambda} + \frac{j}{N} \right) \right) \right) \quad (2.8)$$

where A and λ are the amplitude and length of the serration wave, respectively; N is the number of flutes and $j = 1, N$. This geometric modeling is very specific and only valid for cutters with sinusoidal undulations. Serrations including corners can not be modelled with Eq.(2.8). Another important assumption is done about the helix angle. The radial offset due to undulations should involve the effect of helix as it is defined along the cutter axis. Although the helix angle can be ignored for the solution of the analytical stability lobes proposed by Budak and Altintas [31], it needs to be taken into account for the force calculations.

Campomanes used the same model for regular cylindrical cutters in order to construct cutting forces for serrated cutters. In this model, the axial immersion angle is 90 degrees, which implies that the flutes are perpendicular to the normal of the cutter envelope like in cylindrical end mill case. However, in reality, the axial immersion angle which contributes to the axial force is in effect and changing along the cutter, therefore, it has to be considered in the calculation for an accurate prediction of cutting forces generated by serrated cutters. For the chatter stability of the serrated cutters, he used the model of Budak and Altintas [31] to define regenerative forces as:

$$\{F\} = \frac{1}{2} a B [A(\phi)] [G(i\omega_c)] \{F\} \quad (2.9)$$

where $\{F\}$ is the regenerative force vector, a is axial depth of cut, $[A(\phi)]$ is the directional coefficients matrix and $[G(i\omega_c)]$ is the workpiece-tool transfer function at chatter frequency. B is

regeneration coefficient and defined as $(1 - e^{-i\omega_c T})$ for regular cutters, where T - tooth period is constant for all flutes. The dynamic model can be seen in Figure 2.5. Since tooth period changes in the case of serrated cutters, regeneration coefficient is varying along the cutter axis. In order to overcome this problem, Campomanes applied an approach similar to the one applied for variable pitch cutters by Altintas et al. [43]. He first found an average coefficient for each flute and then obtained an effective coefficient by summing these average coefficients.

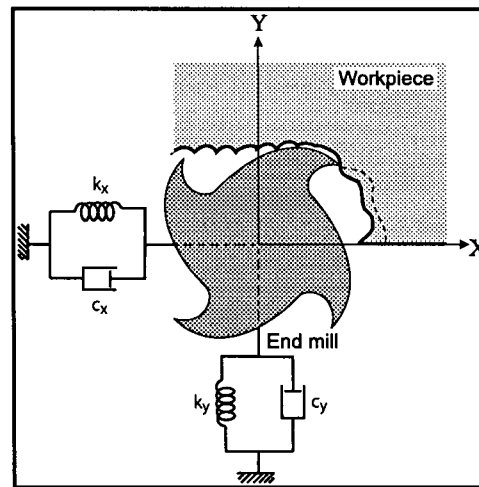


Figure 2.5 : Dynamic Modeling for Milling.

After formulating the problem, he ran simulations for cutting force prediction and chatter stability. Comparison of the simulated cutting forces with serrated cutters appeared to be 30 to 70% less than the ones with regular endmill. For the chatter stability, he concluded that the maximum chatter free axial depth of cut increased with the use of a serrated cutter, however, this improvement started to diminish with an increase in the feed rate.

In multi frequency solution, Minis and Yanushevsky [30] applied the theory of periodic differential equations. The resulting characteristic equation of infinite order is:

$$\det \left[\delta_{rk} [I] - \frac{1}{2} a K_t (1 - e^{-\lambda T}) [W_{r-k}(\lambda + ik\omega_T)] \right] = 0 \quad (2.10)$$

where δ_{rk} is the Kronecker delta, $[I]$ is the $(2m+1) \times (2m+1)$ identity matrix, a is the depth of cut, K_t is the cutting force coefficient in tangential direction, (r,k) are harmonic numbers, i.e. $r, k = 0, \pm 1, \pm 2, \dots \pm m$, ω_T is the tooth passing frequency and W is the oriented transfer function which consists of directional milling coefficients and two dimensional transfer functions. The equation above is truncated and numerically solved to determine eigenvalues. Later, Budak and Altintas [31] managed to solve Eq. (2.10) analytically, by considering only average coefficient of Fourier series ($k=0$) and $\lambda = \pm i\omega_c$ for the limit of stability (marginal stability). However, in these two articles, intermittent machining is not analysed from stability point of view.

Stepan & Bayly et al. [44] studied intermittent machining by modeling the dynamics only in one direction and described the equation of motion:

$$m_x \frac{d^2}{dt^2} x(t) + c_x \frac{d}{dt} x(t) + k_x x(t) = -a q(t) (x(t) - x(t-T))^{x_F} + k_x v t + c_x v \quad (2.11)$$

where v is the constant velocity of the tool due to the feed motion, T is the tooth period, a is the axial depth of cut, $q(t)$ is a T periodic function and m_x, c_x, k_x are the modal parameters of the

machine tool in x direction. x_F is taken as 0.8 which is considered to be a typical value [45].

Assuming the tool motion in the form:

$$x(t) = vt + x_p(t) + \mu(t) \quad (2.12)$$

where vt is the motion due to feed, $x_p(t)$ is the T periodic unperturbed motion (when no self-excited vibrations arise) and $\mu(t)$ is the perturbation. Note that, for ideal case, $\mu(t) = 0$ and Eq. (2.11) reduces to Linear System with Periodic Excitation:

$$m_x \frac{d^2}{dt^2} x_p(t) + c_x \frac{d}{dt} x_p(t) + k_x x_p(t) = -a(vt)^{x_F} q(t) \quad (2.13)$$

Substituting Eqs. (2.12) and (2.13) into Eq. (2.11), expanding the non linear term into Taylor Series and neglecting the higher order terms, the stability equation for perturbation reduces to:

$$m_x \frac{d^2}{dt^2} \mu(t) + c_x \frac{d}{dt} \mu(t) + k_x \mu(t) = -ax_F (vT)^{x_F-1} q(t)(\mu(t) - \mu(t-T)) \quad (2.14)$$

The solution of Eq.(2.14) with Floquet theory at the border stability leads to determination of two different set of frequencies during chatter. The first set of frequencies refers to Hopf bifurcation and defined as $\{(\omega_H = \omega_c \pm n\omega_T), \quad n = 0, 1, 3 \dots\}$ where ω_c is the dominant chatter frequency and $\omega_T = 2\pi/T$ is the tooth passing frequency. The second set refers to Period

Doubling Bifurcation which leads to $\{(\omega_{PD} = (\omega_T/2) \pm n\omega_T), n = 0, 1, 3 \dots\}$. In addition to Hopf Bifurcation, which is the type of bifurcation seen in traditional chatter, Period Doubling (Flip Bifurcation) was shown to be a typical way of stability loss in intermittent milling process. Their results are presented in Figure 2.6.

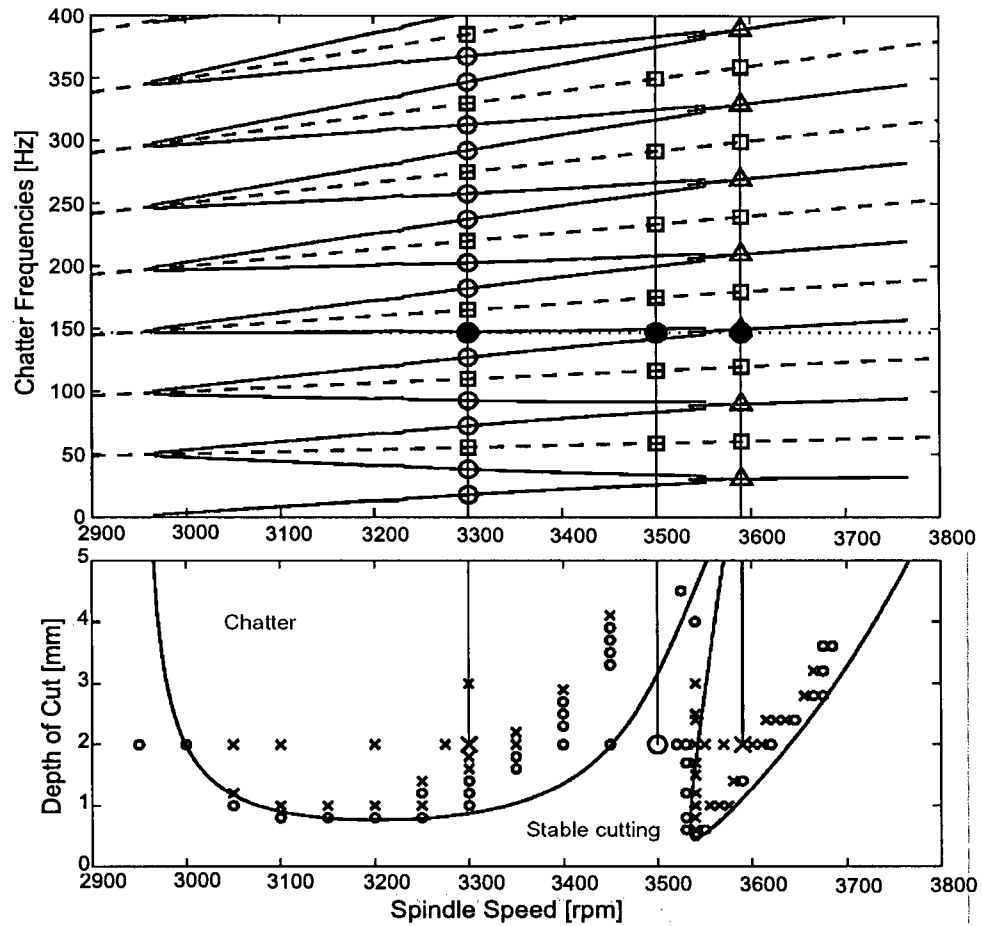


Figure 2.6 : Vibration Frequencies [44] ($\circ - \omega_H$, $\square - \omega_{PD}$, $\Delta - \omega_T$, $\bullet - \omega_d$), ω_d is the damped natural frequency.

Davies et al. [46] also modelled intermittent milling. In this model, structural flexibilities are restricted to one direction -Y axis in Figure 2.5- due to very low radial width of cut. Furthermore,

the angle ϕ between the engaged flute and Y axis is so small that $\sin(\phi) \approx \phi$ and $\cos(\phi) \approx 1$.

Having made these assumptions, the equations of motion are reduced to:

$$\frac{d^2 y}{dt^2} + 2\xi\omega_n \frac{dy}{dt} + \omega_n^2 y = \begin{cases} 0 & \text{if the tool is out of cut} \\ -\frac{a}{m}(K_c \Delta y + K_t f_0)\phi - \frac{aK_t}{m}\Delta y & \text{if the tool is in cut} \end{cases} \quad (2.15)$$

where a is the axial depth of cut, $K_{t,c}$ are the cutting coefficients, f_0 is the feed rate, m is the modal mass and Δy is the difference between current vibration in Y direction and one tooth period (T) before, i.e. $\Delta y = y(t) - y(t - T)$.

The cutter is considered to be under free vibrations when it is out of cut, and delayed force vibrations within cut, as the ratio of time spent cutting to the spindle period is very small for low immersion milling (highly intermittent milling). Combining these two conditions - one becomes the boundary condition of the other - the forced periodic motion of the tool for intermittent milling is obtained. The stability of this equation is then determined by the following equation:

$$\lambda^2 - Tr([B])\lambda + |[B]| = 0 \quad (2.16)$$

where λ are the eigenvalues of $[B]$, $Tr([B])$ and $|[B]|$ are the trace and determinant of $[B]$ and $[B]$, 2x2 matrix, whose elements are function of spindle speed (Ω), natural frequency (ω_n), damping (ζ) and cutting ratio (ρ):

$$[B] = \begin{bmatrix} A_{1,1} & A_{1,2} \\ A_{2,1} + \frac{K_t \rho \omega}{m \Omega} (1 - A_{1,1}) & A_{2,2} - \frac{K_t \rho \omega}{m \Omega} A_{1,2} \end{bmatrix} \quad (2.17)$$

where ρ is the ratio of time spent in cutting to the spindle period and $A_{i,j}$ is member of $[A]$ at the i^{th} row and j^{th} column:

$$[A] = e^{\frac{-\zeta \omega_n}{\Omega}} \begin{bmatrix} \frac{\zeta \omega_n}{\omega_d} \sin\left(\frac{\omega_d}{\Omega}\right) + \cos\left(\frac{\omega_d}{\Omega}\right) & \frac{1}{\omega_d} \sin\left(\frac{\omega_d}{\Omega}\right) \\ \frac{-\omega_n^2}{\omega_d} \sin\left(\frac{\omega_d}{\Omega}\right) & \cos\left(\frac{\omega_d}{\Omega}\right) - \frac{\zeta \omega_n}{\omega_d} \sin\left(\frac{\omega_d}{\Omega}\right) \end{bmatrix} \quad (2.18)$$

The solution to Eq.(2.16) shows that there are two types of vibrations in the system that change the stability. The first one is Hopf Bifurcation with the emergence of a traditional chatter frequency only. The second is Period Doubling (Flip Bifurcation) seen at odd multiples of half-tooth passing frequency. The experimental results by Davies [46] clearly show the existence of those frequencies, which can be seen in Figures 2.7 and 2.8, respectively.

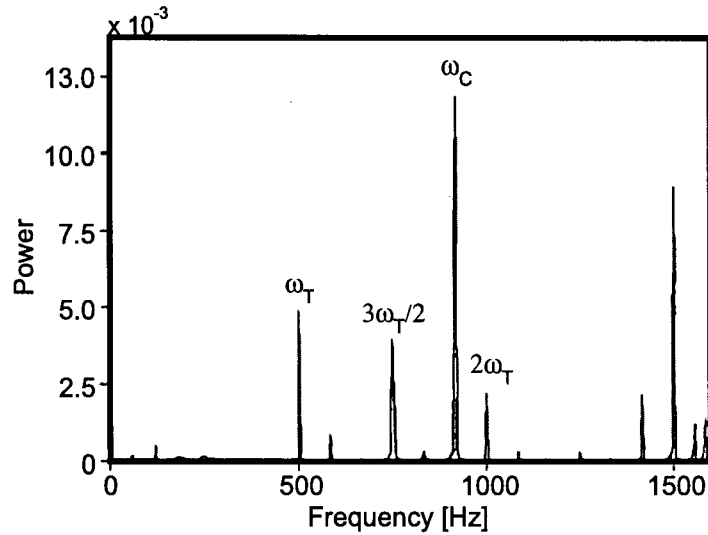


Figure 2.7 : Power Spectra of Experimental Microphone Signals, Hopf Bifurcation, Unstable [46].

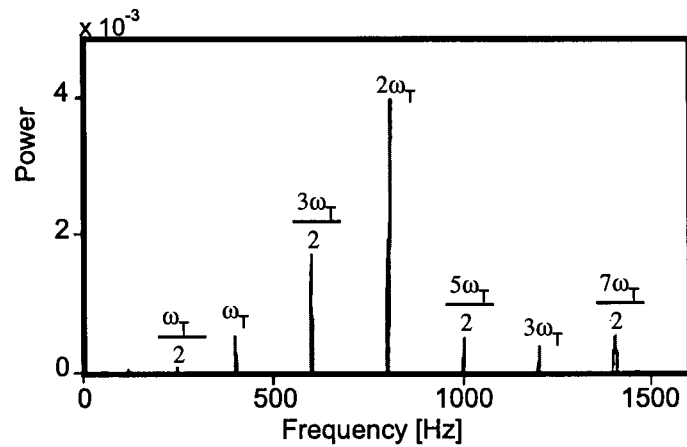


Figure 2.8 : Power Spectra of Experimental Microphone Signals, Flip Bifurcation, Unstable [46].

Both researches show that the frequency contents of unstable vibrations in Hopf and Flip Bifurcation zones are different. An unstable vibration in Hopf Bifurcation zone, as in the case for traditional chatter, contains both integer multiples of tooth passing frequency which is due to cut-

ting and a dominant frequency close to natural frequency of the structure which is solely due to the chatter vibrations. However, an unstable vibration in Flip Bifurcation zone contains integer multiples of half-tooth passing frequency only.

Stepan & Bayly et al. [44] and Davies et al. [46] claimed that the stability solution presented by Budak and Altintas [31] failed to predict the added stability lobes. Although Budak and Altintas did not notice the presence of added stability lobes, their multi frequency solution [31] is proven to predict them in this thesis with detailed analysis of the underlying physics.

Chapter 3

Multi Frequency Chatter Stability in Milling Operations

3.1. Introduction

Either self excited chatter or forced vibrations occur in milling operations. Time domain analysis, which is given in the previous chapter, is an accurate however time inefficient way of predicting chatter vibrations in milling. One alternative and faster method is to formulate a closed form, analytical solution for stability, which was initiated by Tobias [28] and Tlusty [27] in early 1950's. A detailed literature review of the past research was presented in Chapter 2 of the thesis.

Depending on the application, the vibrating system can vary from a single-degree-of-freedom/uni-directional system to a multi-degree-of-freedom/multi-directional one. For example, in turning operations, the cutting forces are constant and acting in a fixed direction, therefore, the dynamic system can be reduced to uni-directional system having flexibilities oriented to the direction of chip thickness generation. However, dynamic modeling in milling is more complicated as the tool experiences rotating cutting forces. The cutting forces change the direction of excitation which requires the consideration of two orthogonal degrees-of-freedom in the formulation of the problem. Cutter, workpiece and machine tool structures are subject to periodic and transient vibrations due to intermittent engagement of cutter teeth and periodically varying milling forces. The wave-forms of the milling forces have harmonic components of the tooth passing frequency depending on the width of cut and/or number of teeth. This dependency is such that the smaller

the width of cut and/or the less the number of teeth on the cutter, the higher the number of harmonics is involved in cutting forces for a given cutting tool. Therefore, the frequency domain solution for this type of problem should cover the wide spectrum of frequencies involved in the cutting process. In this chapter, multi frequency solution to dynamic milling equation, which includes the harmonics of tooth passing frequencies is analyzed and compared against single frequency solution. The objective is to identify stable, most ideal cutting conditions in finish milling operations where the radial width of cut is very small.

A single-degree-of-freedom vibration system as shown in Figure 3.1 is composed of an external force F acting on the mass m , a spring with a stiffness of k and a dashpot with a damping of c . This force F might be constant or varying with time $F=F(t)$. Application of Newton's second law in the direction of x yields:

$$m\ddot{x}(t) + c\dot{x}(t) + kx(t) = F(t) \quad (3.1)$$

Second order differential equation given in Eq.(3.1) has an analytical solution obtained by the superposition of the homogeneous and particular solutions where the former reflects the transient characteristics of the dynamic system, and the latter leads to steady-state behavior. Given the harmonically variable force, $F(t) = F_0 e^{j\omega t}$ with an amplitude of F_0 and a frequency of ω ; the steady-state response is obtained as,

$$x(t) = X e^{(j\omega t + j\phi)} \quad (3.2)$$

where X is the amplitude of response and ϕ is the phase shift between input (Force) and output (Displacement). By taking Laplace transform of Eq.(3.1) and replacing s (Laplace transform parameter) by $j\omega$, transfer function (TF) of the system in frequency domain is found as:

$$G(j\omega) = \frac{x}{F}(j\omega) = \frac{\omega_n^2/k}{(\omega_n^2 - \omega^2) + j2\xi\omega_n\omega} \quad (3.3)$$

where $\omega_n = \sqrt{k/m}$ is the natural frequency and $\xi = c/(2\sqrt{km})$ is the damping ratio.

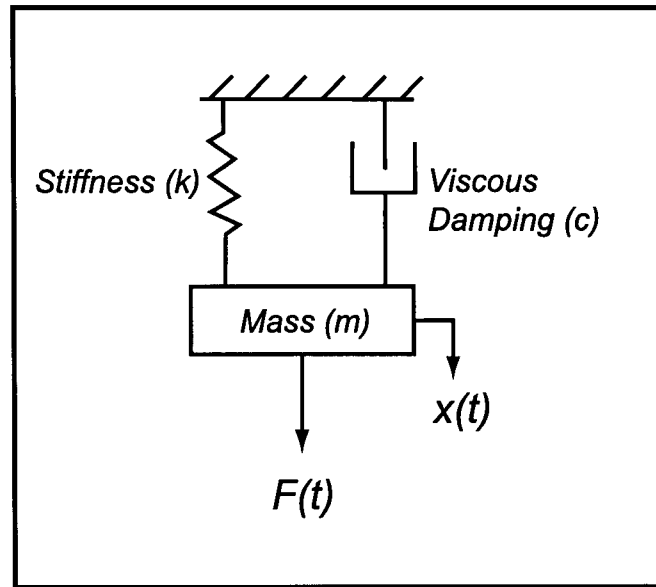


Figure 3.1 : A Single-Degree-of-Freedom Vibration System.

3.2. Dynamics of Milling

Figure 3.2 shows the illustration of an end mill rotating with a rotational speed of Ω [rad/sec]. Cutter with N number of teeth is fed into the workpiece with a feed rate of c . The radial immersion angle, ϕ , is measured from Y axis in clockwise direction, thus, depending on the width of cut, the start (ϕ_{st}) and exit (ϕ_{ex}) angles vary.

The helix angle is taken as zero since it has no effect on the stability of the milling operation [25]. The tangential and radial cutting forces generated by tooth j along the depth of cut (a) can be expressed as:

$$\begin{aligned} F_{tj}(\phi_j) &= K_t a h_j(\phi_j) \\ F_{rj}(\phi_j) &= K_r F_{tj}(\phi_j) \end{aligned} \quad (3.4)$$

where h_j is the dynamic chip thickness, ϕ_j is the rotational position of the tooth j , K_t and K_r are cutting coefficients in tangential and radial directions, respectively. Once cutting forces excite one of the structural modes of machine tool-workpiece system, the tool starts to vibrate and leaves a wavy surface behind. The chip thickness ($h_j(\phi_j)$) including static and dynamic parts can be expressed as follows:

$$h_j(\phi_j) = c \sin(\phi_j) + [u_{j-1} - u_j] \quad (3.5)$$

where c is feed per tooth and (u_j, u_{j-1}) are the dynamic displacements of the cutter in the direction of chip thickness at the present and previous tooth periods, respectively. The static part

$(c \sin(\phi_j))$ comes from the approximation of the trochoidal path, where $\phi_j = \phi_j(t) = \Omega t + j\phi_p$. ϕ_p is a pitch angle which is defined as the angle between two successive teeth. For an uniform pitch cutter, $\phi_p = 2\pi/N$.

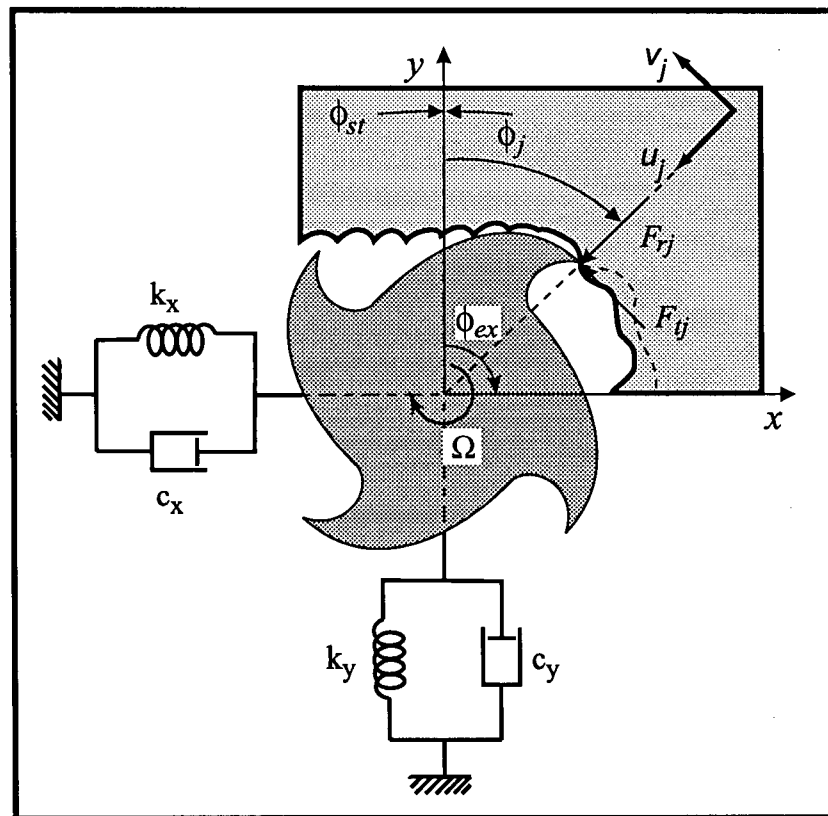


Figure 3.2 : Dynamics of Milling.

The dynamic displacements (u_j, u_{j-1}) at present and past tooth periods can be described in terms of two orthogonal directions (x, y) :

$$\begin{aligned} u_j &= -x(t) \sin \phi_j(t) + y(t) \cos \phi_j(t) \\ u_{j-1} &= -x(t-T) \sin \phi_j(t) + y(t-T) \cos \phi_j(t) \end{aligned} \quad (3.6)$$

where $T = \frac{1}{N\Omega}$ is the tooth period. Similarly, tangential (F_t) and radial (F_r) cutting forces are projected on x and y axes as:

$$\begin{aligned} F_{xj} &= -F_{tj} \cos \phi_j - F_{rj} \sin \phi_j \\ F_{yj} &= F_{tj} \sin \phi_j - F_{rj} \cos \phi_j \end{aligned} \quad (3.7)$$

Finally, total cutting force acting on the tool is found by summing all the forces contributed by each tooth;

$$F_x = \sum_{j=0}^{N-1} g(\phi_j) F_{xj}, \quad F_y = \sum_{j=0}^{N-1} g(\phi_j) F_{yj} \quad (3.8)$$

where $g(\phi_j)$ is the switching function which is equal to unity while cutting and zero otherwise (see Figure 3.3). Substitution of Eqs.(3.4) - (3.7) into Eq.(3.8) gives the dynamic forces as a result of vibrations in (x,y) directions:

$$\begin{Bmatrix} F_x \\ F_y \end{Bmatrix} = \frac{1}{2} a K_t \begin{bmatrix} a_{xx} & a_{xy} \\ a_{yx} & a_{yy} \end{bmatrix} \begin{Bmatrix} \Delta x \\ \Delta y \end{Bmatrix} \quad (3.9)$$

where difference vibrations are $\Delta q = q(t) - q(t - T)$, $q = x, y$. Note that the contribution of static part in chip variation is not considered in the derivation of dynamic milling forces as it does not have any effect on the stability of linear systems like this. Time-varying *directional coefficients* are defined as:

$$\begin{aligned}
 a_{xx} = a_{xx}(t) &= \sum_{j=0}^{N-1} a_{xx,j} = \sum_{j=0}^{N-1} -g_j [\sin 2\phi_j + K_r(1 - \cos 2\phi_j)] \\
 a_{xy} = a_{xy}(t) &= \sum_{j=0}^{N-1} a_{xy,j} = \sum_{j=0}^{N-1} -g_j [(1 + \cos 2\phi_j) + K_r \sin 2\phi_j] \\
 a_{yx} = a_{yx}(t) &= \sum_{j=0}^{N-1} a_{yx,j} = \sum_{j=0}^{N-1} g_j [(1 - \cos 2\phi_j) - K_r \sin 2\phi_j] \\
 a_{yy} = a_{yy}(t) &= \sum_{j=0}^{N-1} a_{yy,j} = \sum_{j=0}^{N-1} g_j [\sin 2\phi_j - K_r(1 + \cos 2\phi_j)]
 \end{aligned} \tag{3.10}$$

One important observation about directional coefficients is that they significantly change the direction of excitation as the tool rotates and this determines the fundamental difference between the dynamics of turning and milling. Eq.(3.9) can be expressed in time domain as

$$\{F(t)\} = \frac{1}{2} a K_t [A(t)] \{\Delta(t)\} \tag{3.11}$$

where vibration difference vector $\{\Delta(t)\} = \{\Delta x, \Delta y\}^T$, dynamic cutting forces vector $\{F(t)\} = \{F_x, F_y\}$ and $[A(t)]$ is equal to directional coefficient matrix.

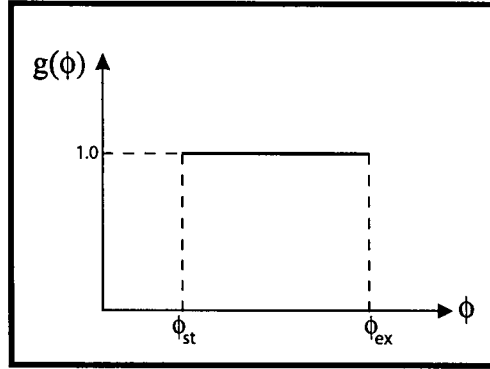


Figure 3.3 : Switching Function.

3.3. Formulation of Stability Equation

Similar to cutting forces, directional coefficient matrix, $[A(t)]$, is periodic at tooth passing frequency $\omega_T = N\Omega$ or at tooth period $T = 1/\omega_T$. Harmonic functions can easily be expressed by Fourier series [31]:

$$[A(t)] = \sum_{r=-\infty}^{\infty} [A_r] e^{ir\omega_T t}, [A_r] = \frac{1}{T} \int_0^T [A(t)] e^{-ir\omega_T t} dt \quad (3.12)$$

Generalized Fourier series for directional coefficients are determined as follows [31]:

$$[A_r] = \frac{1}{T} \int_0^T \left(\sum_{j=0}^{N-1} \begin{bmatrix} a_{xx,j} & a_{xy,j} \\ a_{yx,j} & a_{yy,j} \end{bmatrix} \right) e^{-ir\omega_T t} dt = \frac{1}{T} \int_0^T \left(\sum_{j=0}^{N-1} [A_j(t)] \right) e^{-ir\omega_T t} dt \quad (3.13)$$

Considering the following change of variables $\phi_j = \phi + j\phi_p = \Omega(t + jT) = \Omega\tau_j$ where $\tau_j = t + jT$:

$$[A_r] = \frac{1}{\Omega T} \int_{\phi_{st}}^{\phi_{ex}} [A(\theta)] e^{-irN\theta} d\theta = \frac{N}{2\pi} \int_{\phi_{st}}^{\phi_{ex}} [A(\theta)] e^{-irN\theta} d\theta = \frac{N}{2\pi} \begin{bmatrix} \alpha_{xx}^{(r)} & \alpha_{xy}^{(r)} \\ \alpha_{yx}^{(r)} & \alpha_{yy}^{(r)} \end{bmatrix} \quad (3.14)$$

where

$$\begin{aligned} \alpha_{xx}^{(r)} &= \frac{i}{2} [-c_0 K_r e^{-irN\theta} + c_1 e^{-ip_1\theta} - c_2 e^{ip_2\theta}]_{\phi_{st}}^{\phi_{ex}} \\ \alpha_{xy}^{(r)} &= \frac{1}{2} [-c_0 K_r e^{-irN\theta} + c_1 e^{-ip_1\theta} + c_2 e^{ip_2\theta}]_{\phi_{st}}^{\phi_{ex}} \\ \alpha_{yx}^{(r)} &= \frac{1}{2} [c_0 K_r e^{-irN\theta} + c_1 e^{-ip_1\theta} + c_2 e^{ip_2\theta}]_{\phi_{st}}^{\phi_{ex}} \\ \alpha_{yy}^{(r)} &= \frac{i}{2} [-c_0 K_r e^{-irN\theta} - c_1 e^{-ip_1\theta} + c_2 e^{ip_2\theta}]_{\phi_{st}}^{\phi_{ex}} \end{aligned} \quad (3.15)$$

$$\text{and } p_1 = 2 + Nr, p_2 = 2 - Nr, c_0 = \frac{2}{Nr}, c_1 = \frac{K_r - i}{p_1}, c_2 = \frac{K_r + i}{p_2}.$$

Note that the directional coefficients given above become infinity when $Nr = \pm 2$. This is solely due to the trigonometric conversions during the generalization of the integrals in Eq.(3.14). In such a case, the directional coefficients can be obtained by solving the integrals from its original form. For $Nr=2$, the following integrals obtained from Eq. (3.14) are to be solved:

$$\begin{aligned}
\alpha_{xx}^{(r)} &= - \int_{\phi_{st}}^{\phi_{ex}} [\sin 2\theta + K_r(1 - \cos 2\theta)] e^{-i2\theta} d\theta \\
\alpha_{xy}^{(r)} &= - \int_{\phi_{st}}^{\phi_{ex}} [(1 + \cos 2\theta) + K_r \sin \theta] e^{-i2\theta} d\theta \\
\alpha_{yx}^{(r)} &= \int_{\phi_{st}}^{\phi_{ex}} [(1 - \cos 2\theta) - K_r \sin \theta] e^{-i2\theta} d\theta \\
\alpha_{yy}^{(r)} &= \int_{\phi_{st}}^{\phi_{ex}} [\sin 2\theta - K_r(1 + \cos 2\theta)] e^{-i2\theta} d\theta
\end{aligned} \tag{3.16}$$

which leads to following coefficients:

$$\begin{aligned}
\alpha_{xx}^{(r)} &= \frac{1}{8} \{ 4\theta i + e^{-i4\theta} - K_r [(4e^{-i2\theta} - e^{-i4\theta})i - 4\theta] \} \\
\alpha_{xy}^{(r)} &= \frac{-1}{48} [(4e^{-i2\theta} + e^{-i4\theta})6i + 24\theta + 8K_r(3e^{-i\theta} - e^{-i3\theta})] \\
\alpha_{yx}^{(r)} &= \frac{1}{48} [(4e^{-i2\theta} - e^{-i4\theta})6i - 24\theta - 8K_r(3e^{-i\theta} - e^{-i3\theta})] \\
\alpha_{yy}^{(r)} &= \frac{1}{8} \{ -4\theta i - e^{-i4\theta} - K_r [(4e^{-i2\theta} + e^{-i4\theta})i + 4\theta] \}
\end{aligned} \tag{3.17}$$

The directional coefficients for $Nr=-2$ are simply equal to complex conjugates of the ones for $Nr=2$. For example, when $N=1$ and $r=2$, the directional coefficient in x direction will be:

$$\alpha_{xx}^{(2)} = \alpha_{xx, REAL}^{(2)} + i\alpha_{xx, IMAG}^{(2)} \tag{3.18}$$

where

$$\alpha_{xx, REAL}^{(2)} = \frac{1}{8} [\cos 4\theta - K_r (4(\sin 2\theta - \theta) - \sin 4\theta)] \Big|_{\phi_{st}}^{\phi_{ex}},$$

$$\alpha_{xx, IMAG}^{(2)} = \frac{1}{8} [4\theta - \sin 4\theta + K_r (\cos 4\theta - 4\cos 2\theta)] \Big|_{\phi_{st}}^{\phi_{ex}}.$$

Having expanded $[A(t)]$ into Fourier series and inserted into Eq.(3.11), right side of Eq.(3.11) becomes function of tooth passing frequencies which come from directional coefficients, and vibration (chatter) frequency due to vibration terms, $\{\Delta(t)\}$. Thus, dynamic milling forces ($\{F(t)\}$) should contain both tooth passing frequencies ($k\omega_T$) and chatter frequency, ω_c . According to Floquet's theorem which states that for a second order differential equation with periodic and piecewise continuous coefficients, the solution have the following form:

$$\{F(t)\} = e^{\lambda t} \{P(t)\} \quad (3.19)$$

where the $\{P(t)\}$ is a periodic function of tooth passing frequency (ω_T). The cutter and workpiece will vibrate with frequency at the chatter stability, thus, $\lambda = i\omega_c$ [31]. When periodic function $\{P(t)\}$ is expanded into Fourier series, the following expression is obtained for dynamic milling forces:

$$\{F(t)\} = e^{i\omega_c t} \sum_{k=-\infty}^{\infty} \{P_k\} e^{ik\omega_T t} = \sum_{k=-\infty}^{\infty} \{P_k\} e^{i(\omega_c + k\omega_T)t} \quad (3.20)$$

Dynamic displacements can be obtained by using the transfer function of the structure,

$$\begin{Bmatrix} x \\ y \end{Bmatrix} = [G]\{F(t)\} = \sum_{k=-\infty}^{\infty} [G(i(\omega_c + k\omega_T))]\{P_k\}e^{i(\omega_c + k\omega_T)t} \quad (3.21)$$

where $[G(i\omega)]$ is the transfer function of the structure both in (x,y) directions:

$$[G(i\omega)] = \begin{bmatrix} G_{xx}(i\omega) & G_{xy}(i\omega) \\ G_{yx}(i\omega) & G_{yy}(i\omega) \end{bmatrix} \quad (3.22)$$

In Eq.(3.22), diagonal elements are direct transfer functions in the respective directions, whereas off-diagonal elements are cross transfer functions. The dynamics along the cutter or work piece do not change much unless there is a special condition like thin wall machining; therefore, measurement of the transfer functions at the tool tip is enough for most cases.

Substituting Eqs. (3.12), (3.20) and (3.21) into Eq.(3.11):

$$\sum_{k=-\infty}^{\infty} \{P_k\}e^{ik\omega_T t} = \frac{1}{2}aK_t(1 - e^{-i\omega_c T}) \sum_{r=-\infty}^{\infty} \sum_{k=-\infty}^{\infty} [A_r][G(i(\omega_c + k\omega_T))]\{P_k\}e^{i(r+k)\omega_T t} \quad (3.23)$$

Multiplying both sides of the equation by $1/Te^{-ip\omega_T t}$ and integrating from 0 to T , the following is obtained by using orthogonality principle [31]:

$$\{P_p\} = \frac{1}{2}aK_t(1 - e^{-i\omega_c T}) \sum_{k=-\infty}^{\infty} [A_{p-k}][G(i(\omega_c + k\omega_T))]\{P_k\} \quad (3.24)$$

Hence, the nontrivial solution is reduced to an eigenvalue problem as:

$$\det[[I] + \Lambda[A_{p-k}][G(i(\omega_c + k\omega_T))]] = 0 \quad (3.25)$$

where $\Lambda = -\frac{1}{2}aK_f(1 - e^{-i\omega_c T})$, (p, k) are harmonics, i.e., $(p, k) = 0, \pm 1, \pm 2, \dots$, $[I]$ is an identity matrix and $[A_{p-k}]$ is obtained from Eq. (3.14) for $r=p-k$.

Defining $[G_o(i\omega)] = [A_{p-k}][G(i(\omega_c + k\omega_T))]$ as *oriented transfer function*:

$$[G_o(i\omega)] = \left(\begin{array}{c} k=0 \ 1 \ -1 \ \dots \ h_r \ -h_r \end{array} \right) \left\{ \begin{array}{c} [G_o^{(0,0)}] \ [G_o^{(-1,1)}] \ [G_o^{(1,-1)}] \ \dots \ . \\ [G_o^{(1,0)}] \ [G_o^{(0,1)}] \ [G_o^{(2,-1)}] \ \dots \ . \\ [G_o^{(-1,0)}] \ [G_o^{(-2,1)}] \ [G_o^{(0,-1)}] \ \dots \ . \\ . \quad . \quad . \quad \dots \quad . \\ . \quad . \quad . \quad \dots \quad . \\ . \quad . \quad . \quad \dots \quad [G_o^{((p-k),k)}] \end{array} \right\} \begin{array}{c} p= \\ 0 \\ 1 \\ -1 \\ . \\ . \\ h_r \\ -h_r \end{array} \quad (3.26)$$

where

$$[G_o^{((p-k),k)}] = \frac{N}{2\pi} \begin{bmatrix} \alpha_{xx}^{(p-k)} G_{xx}(i(\omega_c + k\omega_T)) & \alpha_{xy}^{(p-k)} G_{yy}(i(\omega_c + k\omega_T)) \\ \alpha_{yx}^{(p-k)} G_{xx}(i(\omega_c + k\omega_T)) & \alpha_{yy}^{(p-k)} G_{yy}(i(\omega_c + k\omega_T)) \end{bmatrix} \quad (3.27)$$

Defining h_r as the total number of harmonics of tooth passing frequency taken into account, $2(2h_r + 1)$ complex eigenvalues are obtained from Eq.(3.25). For example, if only first harmonic $(-\omega_T, \omega_T)$ is considered, $h_r = 1$ and the matrices in Eq.(3.25) become 6 by 6 leading to 6 complex eigenvalues.

Critical depth of cuts can be solved in terms of eigenvalues Λ as:

$$a_{lim,q} = \frac{-2\Lambda_q}{K_t(1 - e^{-i\omega_c T})} = a_{R,q} + ia_{I,q} \quad (3.28)$$

where $\Lambda_q = \Lambda_{R,q} + i\Lambda_{I,q}$, $q = 1 \dots 2(2h_r + 1)$ and subscripts R and I represent real and imaginary parts, respectively. Substituting $e^{-i\omega_c T} = \cos(\omega_c T) - i\sin(\omega_c T)$ into Eq.(3.28),

$$a_{R,q} = \frac{-1}{K_t} \left[\frac{\Lambda_{R,q}(1 - \cos(\omega_c T)) + \Lambda_{I,q}\sin(\omega_c T)}{1 - \cos(\omega_c T)} \right] \quad (3.29)$$

$$a_{I,q} = \frac{-1}{K_t} \left[\frac{\Lambda_{I,q}(1 - \cos(\omega_c T)) - \Lambda_{R,q}\sin(\omega_c T)}{1 - \cos(\omega_c T)} \right] \quad (3.30)$$

In order to obtain a physical depth of cut, imaginary part of the limiting depth of cut must be equated to zero, i.e. $a_{I,q} = 0$, which result in the following relationship:

$$\frac{\Lambda_{I,q}}{\Lambda_{R,q}} = \frac{\sin(\omega_c T)}{1 - \cos(\omega_c T)} \quad (3.31)$$

Using half-angle trigonometric conversion for $(\omega_c T)$:

$$\tan \psi = \frac{\Lambda_{I,q}}{\Lambda_{R,q}} = \frac{\cos\left(\frac{\omega_c T}{2}\right)}{\sin\left(\frac{\omega_c T}{2}\right)} = \tan\left(\frac{\pi}{2} - \frac{\omega_c T}{2} + \pi k\right) \quad (3.32)$$

where $k = 0, 1, 2, \dots$. From Eq.(3.32),

$$\omega_c T = 2\pi k + \varepsilon \quad (3.33)$$

where $\varepsilon = \pi - 2\psi$ is the phase angle between current and previous vibration marks. Spindle speed, $n[rpm]$, can be obtained from tooth period T as:

$$n = \frac{60\omega_c}{N(2\pi k + \varepsilon)} \quad (3.34)$$

And the physical depth of cut corresponding to this set of spindle speeds is:

$$a_{R,q} = \frac{-1}{K_t} \Lambda_{R,q} \left[1 + \left(\frac{\Lambda_{I,q}}{\Lambda_{R,q}} \right)^2 \right] \quad (3.35)$$

Note that, positive depth of cut can only be possible, if and only if $\Lambda_{R,q} < 0$.

3.4. Solution of Stability Equation

In the previous section, it is shown that eigenvalues (Λ) need to be calculated to obtain chatter free depth of cuts and corresponding spindle speeds for a given machine tool-workpiece sys-

tem and cutting conditions (radial depth of cut, cutting force coefficients,...). However, from Eq.(3.25) it can be seen that chatter (ω_c) and tooth passing (ω_T) frequencies have to be known for a successful accomplishment. Unlike single frequency solution - which considers only the average coefficient of directional coefficient matrix, $[A_0]$, the multi frequency solution requires scanning of both chatter and tooth passing frequencies. A computer algorithm is developed to solve the multi frequency chatter problem. The flow chart of this program is given in Figure 3.5.

The algorithm for stability lobes - stable depth of cut vs. spindle speed - follows the sequence given below:

- (*) Cutter immersion angles (entrance & exit), machine/workpiece dynamics and number of teeth on the cutter are specified.
- (*) Spindle speed range at which the stability lobes are desired and spindle speed increment are specified.
- (*) Chatter frequency range is determined as $\omega_{c,min} \leq \omega_c \leq \omega_{c,max}$, where $\omega_{c,min}$ is selected as 20% of the minimum, and $\omega_{c,max}$ as 150% of the maximum of all natural frequencies of machine tool-workpiece system. Chatter frequency resolution ($\Delta\omega_c$) must be small enough for the accuracy of the solution. In the simulations for this thesis, $\Delta\omega_c = 0.1Hz$.
- (*) Total number of tooth passing frequency harmonics, i.e. h_r , is selected. Higher h_r leads to better approximation of directional coefficients by Fourier series which in turn improves the accuracy of the solution. However, computation time increases drastically due to its direct effect on the number of solutions (eigenvalues). Figure 3.4 shows how the Fourier approximation for one of the time dependant directional coefficients changes with respect to number of harmonics taken into account.

For a two orthogonal degree-of-freedom system, directional coefficient matrix becomes $(4h_r+2) \times (4h_r+2)$ which results in $2 \times (2h_r+1)$ eigenvalues obtained from Eq.(3.25).

- (*) Tooth passing frequency and tooth period are calculated at the start value of spindle speed and eigenvalues are determined.
- (*) For each eigenvalue (Λ_q), conditions $\Lambda_{R,q} < 0$ and $\Lambda_{I,q} = 0$ are checked. Minimum $a_{lim,q}$ is determined within the eigenvalues satisfying those conditions is stored in a temporary array.
- (*) After calculating all local minimum limiting depths of cut (a_{local_lim}) for each frequency, global minimum for that particular spindle speed is selected as the smallest among those. The chatter frequency becomes the corresponding frequency for that a_{lim} .
- (*) The steps are followed until full range of spindle speeds is covered.

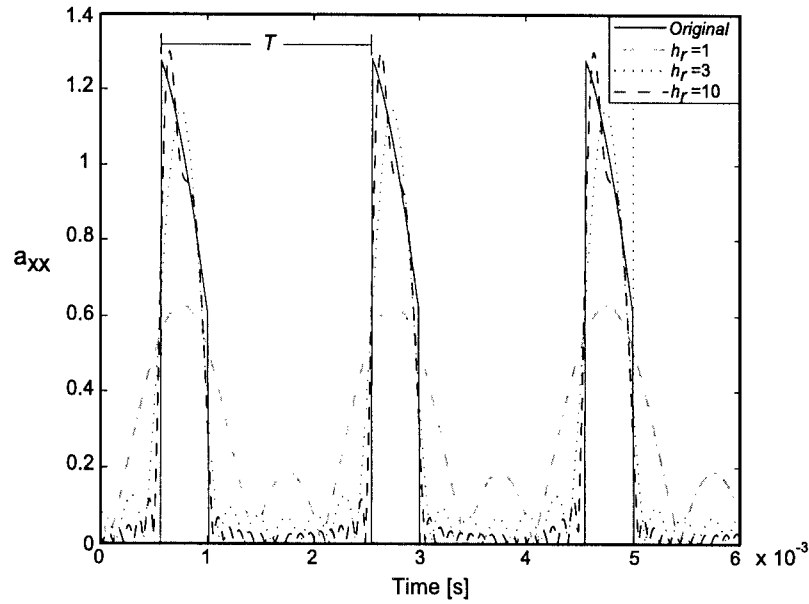


Figure 3.4 : Directional Coefficient, a_{xx} . $\phi_{st} = 153^\circ$, $\phi_{ex} = 180^\circ$, $N=3$, $n=10000$ rpm, $K_r = 0.3$.

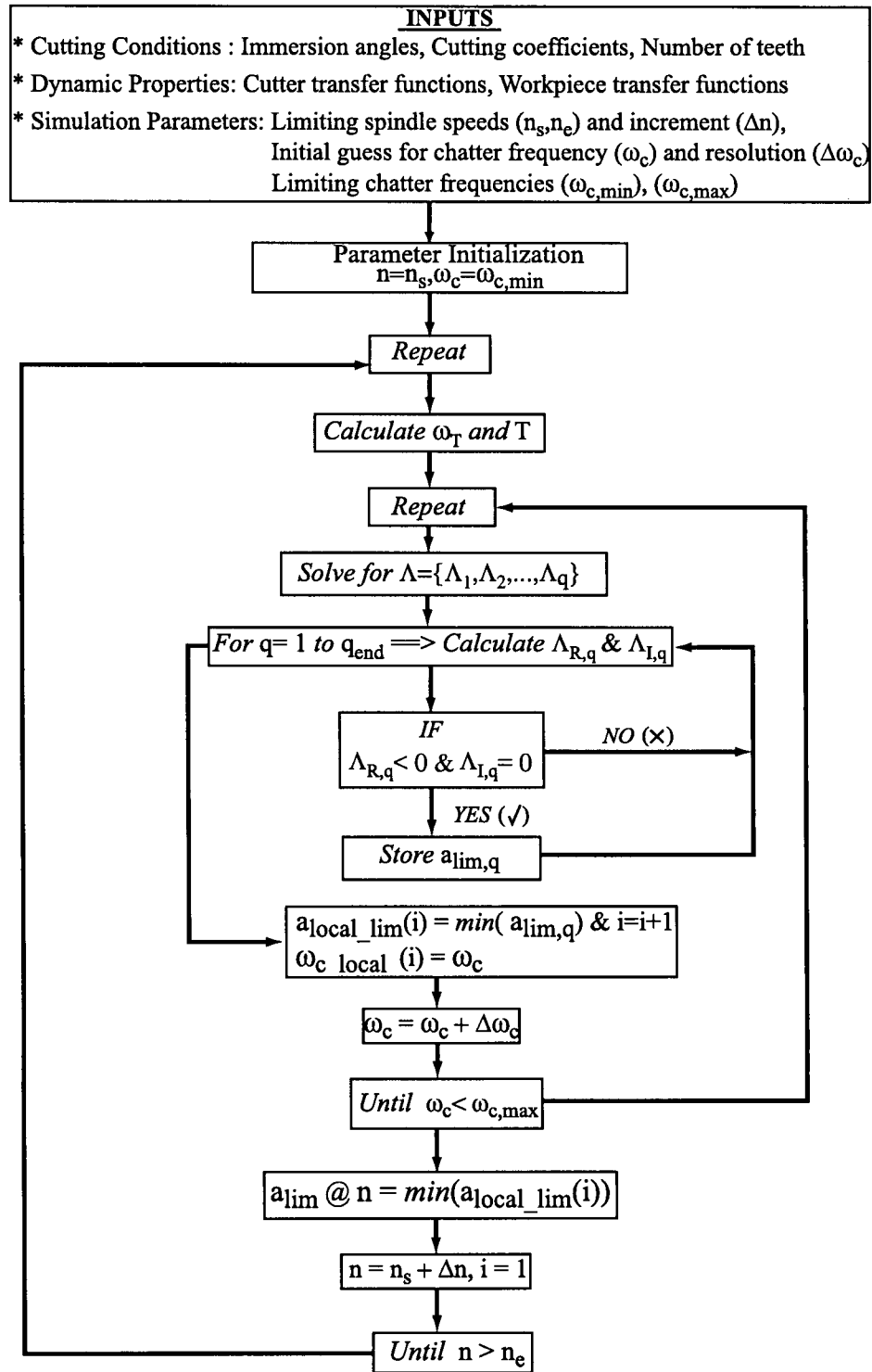


Figure 3.5 : Flow Chart of Multi Frequency Solution.

In the case of multi frequency chatter stability, iterative solution as given in the flow chart is inevitable to obtain stability lobes due to dependency of transfer function on the spindle speed. The transfer function at its harmonics, i.e. $G(i(\omega + k\omega_T))$, is simply the shifted form of original transfer function, $G(i\omega)$, in frequency domain. For positive harmonics, transfer function shifts to the left, whereas for negative ones, it shifts to the right. This is shown for real part of the transfer function in Figure 3.6. Note that transfer function is symmetric with respect to $\omega = 0$ line (*y-axis*). Although frequencies less than zero are not scanned during the solution, Figure 3.6 including both positive and negative frequency ranges is given for reference.

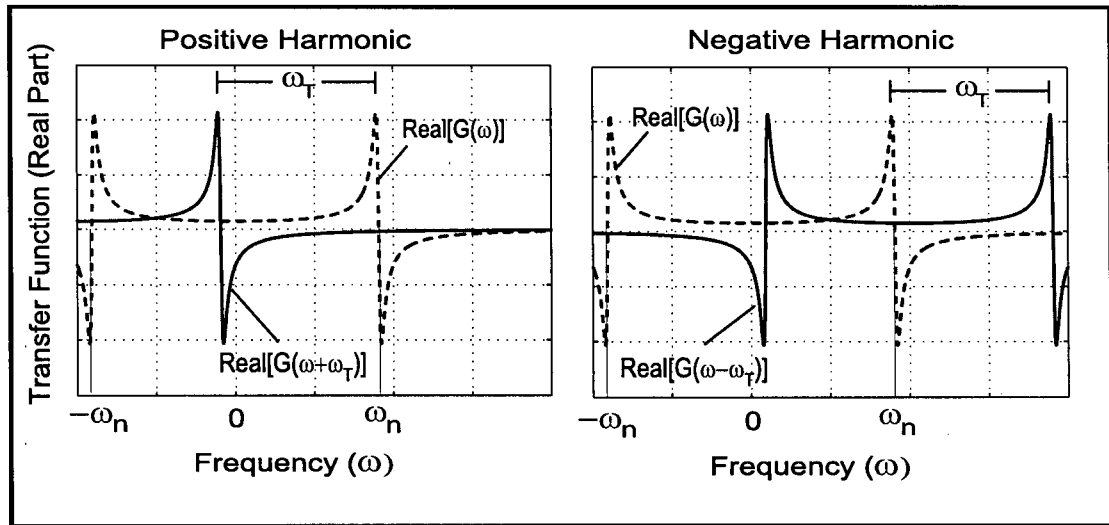


Figure 3.6 : Real Part of Transfer Function and its First Harmonics.

3.5. Simulations

The formulation given above is coded in a computer program and run under different cutting conditions. The radial width of cut is selected to be small which leads to highly intermittent milling forces with high number of harmonics. The results are compared against time domain simula-

tion which considers the complete physics without any approximation used in frequency domain. The Fast Fourier Transforms (FFTs) of simulated cutting forces and tool vibrations are used to interpret whether the dynamic system is under chatter vibrations (unstable) or not (stable). The details of the identification process can be found in the following section where individual cutting points are assessed.

3.5.1. Low Radial Width of Cut I (One Dimensional - Y only)

In this simulation, end mill with 23.6 mm diameter and 3 flutes is used with a feedrate of 0.120 mm/rev.tooth and a radial immersion of 1.256 mm. The material is assumed to be Al6061 with $K_t = 500N/mm^2$ and $K_r = 0.3$. Since the radial width of cut is too small, the structure is assumed to have flexibilities only in Y direction, i.e., $G_{xx} = 0$. As mentioned earlier, more harmonics are required within the solution in order to take intermittent cutting due to small immersion into account. In this particular example, the stability lobes are obtained by considering only up to three harmonics of tooth passing frequency, i.e. $h_r=3$. For one directional flexibility and three harmonics ($h_r=3$), stability equation (Eq. (3.25)) reduces to:

$$\det \left\{ [I]_{7 \times 7} + \Lambda \frac{N}{2\pi} [G_{o,yy}] \right\} = 0 \quad (3.36)$$

where

$$[G_{o,yy}] = \begin{bmatrix} \alpha_{yy}^{(0)} G_{yy}(i\omega_c) & \alpha_{yy}^{(-1)} G_{yy}(i(\omega_c + \omega_T)) & \dots & \dots & \dots \\ \alpha_{yy}^{(1)} G_{yy}(i\omega_c) & \alpha_{yy}^{(0)} G_{yy}(i(\omega_c + \omega_T)) & \dots & \dots & \dots \\ \alpha_{yy}^{(-1)} G_{yy}(i\omega_c) & \alpha_{yy}^{(-2)} G_{yy}(i(\omega_c + \omega_T)) & \dots & \dots & \dots \\ \dots & \dots & \dots & \dots & \alpha_{yy}^{(0)} G_{yy}(i(\omega_c - 3\omega_T)) \end{bmatrix}_{7 \times 7} \quad (3.37)$$

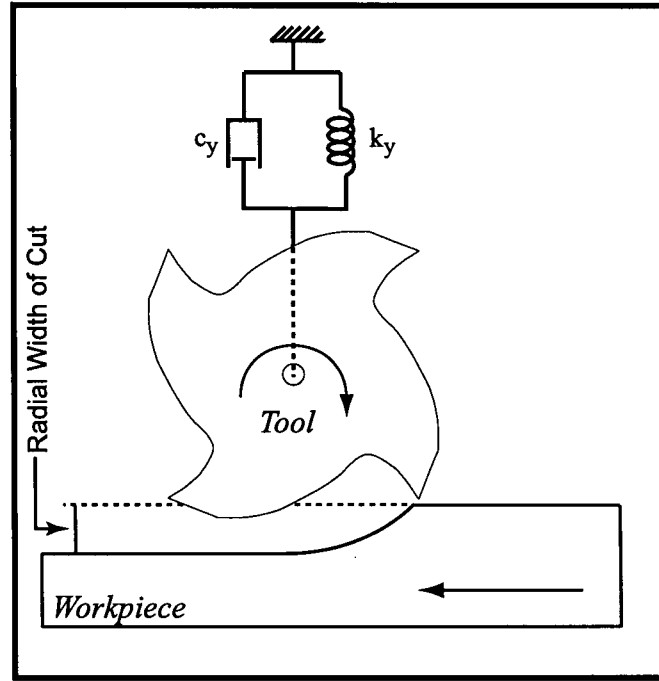


Figure 3.7 : Low Radial Immersion Milling.

After solving the stability equation, stability lobes are obtained as shown in Figure 3.8. Traditional lobes, where $h_r=0$, are plotted for comparison purposes. In traditional approach, only the average term of Fourier Series, i.e. $[A_0]$, is used to model the directional cutting force coefficients which is enough for most of the cases.

The most noticeable difference between two lobes is the added stability pockets at certain spindle speed range. The cutting operation around 36000 rpm is analyzed by selecting couple of cutting conditions such as *A*, *B* and *C* and comparing them against time domain simulations. The tool vibration and cutting forces obtained at these points are presented in Figures 3.10-3.12.

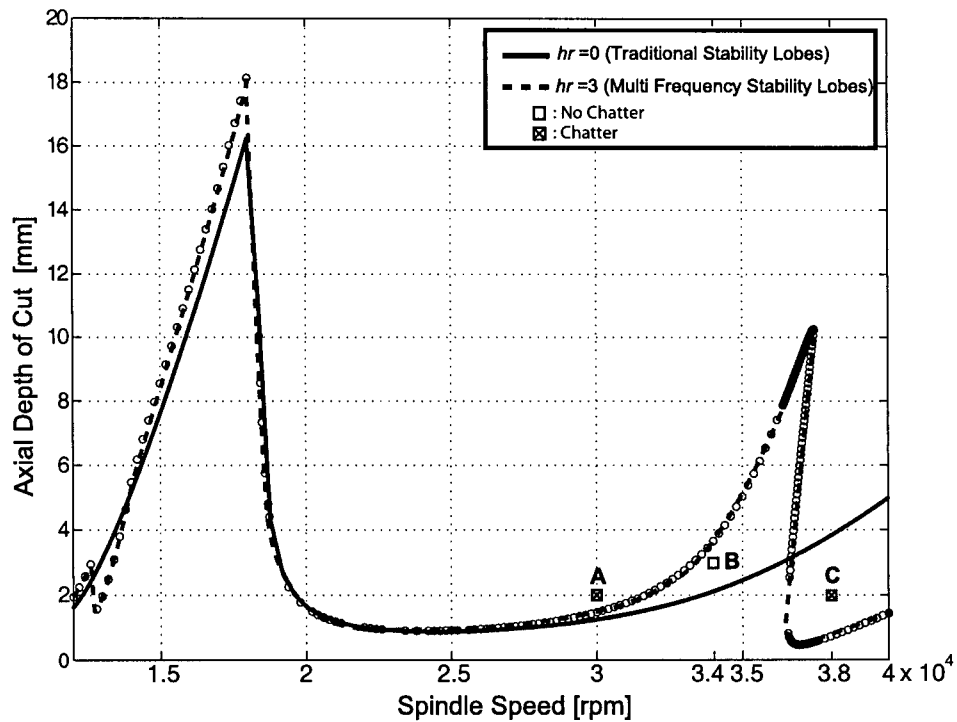


Figure 3.8 : Stability Lobes for Low Immersion Down Milling,
Dynamic Parameters: $\omega_n = 907 \text{ Hz}$, $k = 1.4 \text{e}6 \text{ N/m}$, $\zeta = 0.017$.

The detailed view of added stability pocket is presented in Figure 3.9. Sample cutting conditions are simulated and defined as either stable or unstable.

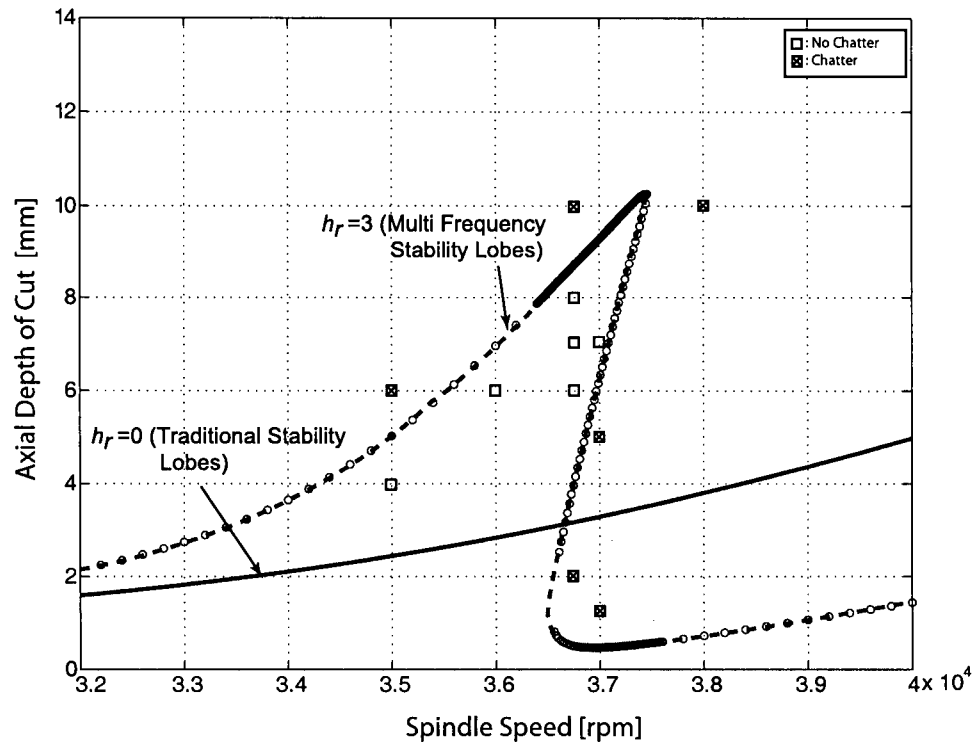


Figure 3.9 : New Stability Pocket, Comparison of Time and Frequency Domain Results.

At point A ($n = 30000$ rpm , $a = 2$ mm), both traditional and multi frequency solutions give chatter, and both solutions, i.e. depth of cuts, are almost equal to each other. The reason why those two solutions converge each other will be elaborated later. Cutting simulation is conducted under specified cutting conditions, and some of the results are presented in Figure 3.10. It can be seen that there is only one dominant frequency in the spectrum of vibrations in Y direction, which is chatter vibration frequency. From Time Domain Simulation (TDS) and Multi Frequency Solution (MFS), it is obtained as $\omega_{c,TDS} = 947.23Hz$, $\omega_{c,MFS} = 946.9Hz$, respectively. In Literature Review section, this type of vibration is named as Hopf Bifurcation.

Point **B** ($n = 34000$ rpm , $a = 3$ mm) is located above the traditional but below the multi frequency stability lobes, that is why it is expected to be unstable for the former condition as opposed to stable for the latter. Time domain simulation, presented in Figure 3.11, shows that the dominant frequencies of both the tool vibration and cutting force are only at the tooth passing frequency (ω_T) and its integer harmonics which is due to the periodic behavior of milling process.

Point **C** ($n = 38000$ rpm , $a = 2$ mm) is selected as the opposite of Point **B**. This point is expected to be unstable since an additional stability pocket is obtained from multi frequency solution. Point **C** is simulated in time domain, and the results are presented in Figure 3.12. The cutting forces and tool vibration indicate instability due to growing amplitudes predicted by the time domain solution. According to common knowledge of traditional chatter, this cutting point must result in the unstable vibration of the process at a frequency close to natural frequency. However, the outcome of the simulation is quite different. It can be seen that only tooth passing frequency & its harmonics ($k\omega_T$), as well as half tooth passing frequency & its odd harmonics ($(2k+1)(\omega_T/2)$) are dominant, where k is a positive integer number. This type of vibration is called Flip Bifurcation and explained in Chapter 2 of the thesis. The multi frequency solution calculates the most dominant vibration frequency as $\omega_{c,MFS} = 950.5Hz$ which is almost equal to $\omega_{c,TDS} = \omega_T/2 = 950Hz$ (dominant frequency of the simulated tool vibration). Note that the harmonic component close to the natural frequency of the structure is determined to be the dominant frequency for the tool vibration. This is expected as the vibration of the tool is mostly driven by the frequency close to natural frequency of the structure.

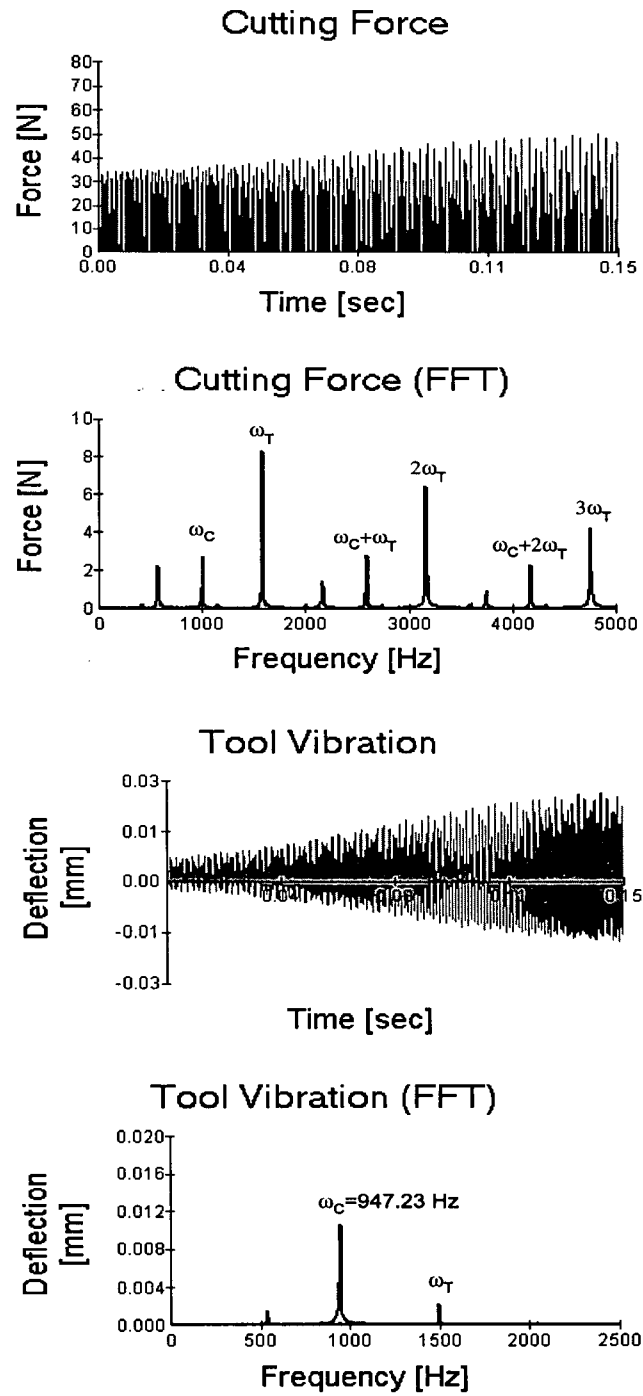


Figure 3.10 : Time Domain Simulation of Cutting Force and Tool Vibration in Y direction, Point A: $n=30000 \text{ rpm}$, $a=2 \text{ mm}$, Unstable.

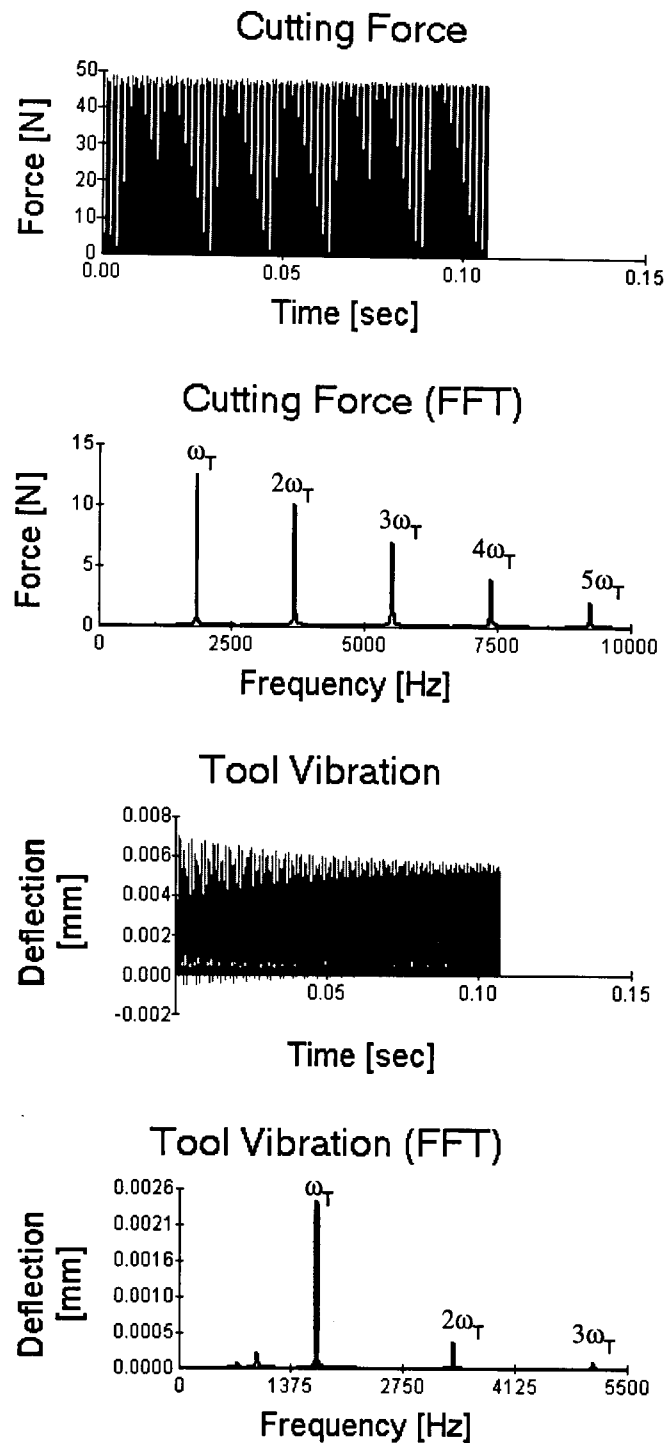


Figure 3.11 : Time Domain Simulation of Cutting Force and Tool Vibration in Y direction, Point B: $n=34000$ rpm, $a=3$ mm, Stable.

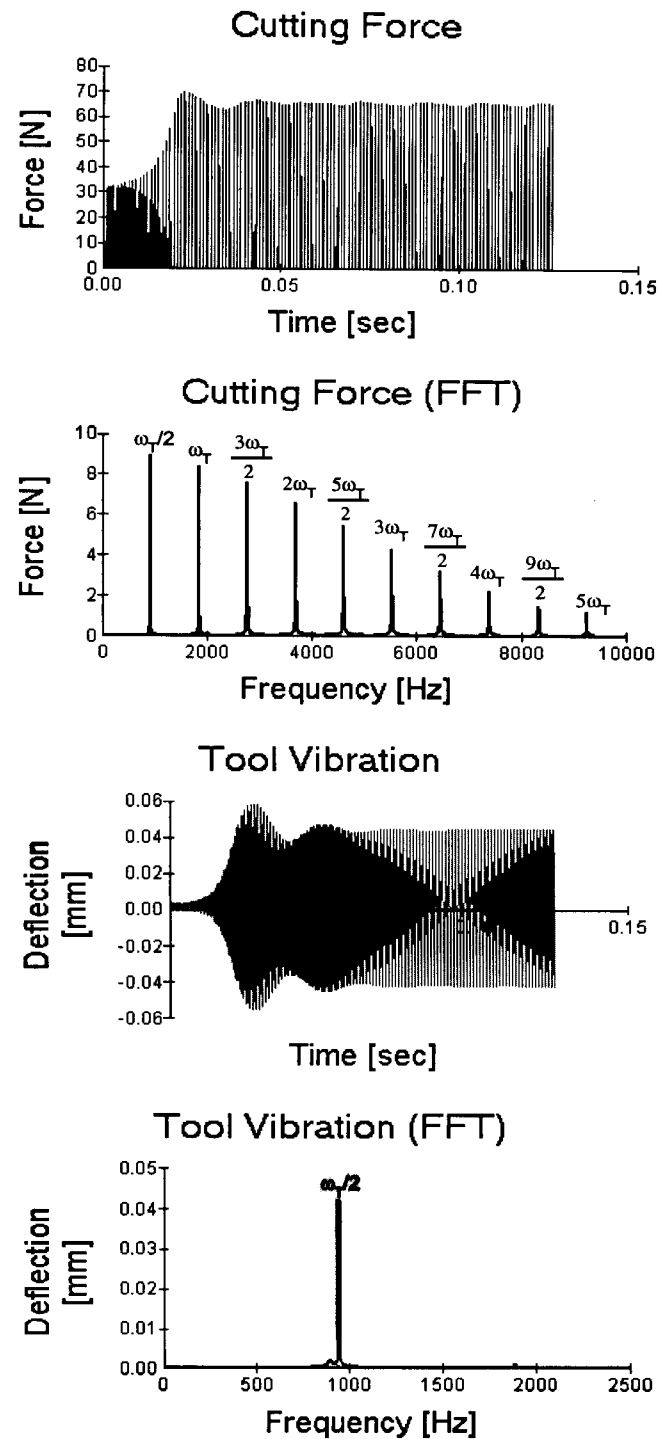


Figure 3.12 : Time Domain Simulation of Cutting Force and Tool Vibration in Y direction, Point C: $n=38000$ rpm, $a=2$ mm, Unstable.

For a better understanding of the reason behind the discrepancies between Time Domain and Multi Frequency Solutions, the elements of stability equation need to be analyzed over the frequency range of interest. Stability equation (Eq. (3.36)) is dependent on two variables for a given cutter:

- 1) Directional coefficients, $\alpha_{yy}^{(n)}$,
- 2) Transfer function and its harmonics, $G_{yy}(i\omega \pm ik\omega_T)$.

Directional coefficients, as shown before in Eq. (3.15), are constant as long as the number of harmonics (k) to be considered in the solution is fixed. Therefore, variation of transfer function at certain spindle speeds, which determines the tooth passing frequency ω_T , needs to be investigated.

Real and imaginary parts of the transfer function and its harmonics at 30000 rpm are shown in Figure 3.13. Middle figure is for positive harmonics of transfer function which are negligibly small for $\omega > 0$, therefore, only first negative harmonic of transfer function, $G_{yy}(\omega - \omega_T)$, has significance within $\omega > 0$ range. When frequencies are swept from ω_{min} to ω_{max} at two different set of frequencies, dominance of transfer functions change. For example, around 900 Hz, $G_{yy}(\omega)$ has a mode, therefore compared to values of the other transfer functions, it is more dominant, i.e. $G_{yy}(\omega \pm k\omega_T) = 0$ for $k = 0, 1, 2, 3$. Parallel to this observation, Eq. (3.36) can be approximated as:

$$\left[1 + \Lambda \frac{N}{2\pi} \alpha_{yy}^{(0)} G_{yy}(i\omega_c) \right] = 0 \quad (3.38)$$

This implies that solution for this system at 30000 rpm must be closer to traditional solution. In fact, this is verified by the stability lobes given in Figure 3.8. Although the behavior of $G_{yy}(\omega \pm \omega_T)$ around 500 Hz looks similar, the differences due to mirror image of the transfer function leads to numerical discrepancies in the calculation of eigenvalues. For example, the solutions obtained from the sweeping of all frequencies ($\omega_{max} > \omega > \omega_{min}$) are found as:

$$a_{lim@552.36Hz} = 1.5382mm, a_{lim@946.9Hz} = 1.5090mm$$

Since the minimum value of depth of cut is critical for stability analysis, $a_{lim@946.9Hz}$ is selected at 30000 rpm and the possible chatter frequency at this point is close to $\omega_{c,MFS} = 946.9Hz$, not to 552.36 Hz which is verified by the time domain simulation results presented in Figure 3.10.

As the spindle speed varies, tooth passing frequency changes, so does the amount of shift of transfer function at its harmonics. The real and imaginary parts of the transfer function at 38000 rpm are shown in Figure 3.14. At this particular speed, both $G_{yy}(\omega)$ and $G_{yy}(\omega - \omega_T)$ have almost same magnitude around 900 Hz, therefore, stability equation (Eq. 3.36) can no longer be approximated as Eq. (3.38). Discarding all the positive harmonics, and two of negative ($k=2,3$) harmonics of transfer function, the stability equation becomes:

$$\det \left\{ [I] + \Lambda \frac{N}{2\pi} \begin{bmatrix} \alpha_{yy}^{(0)} G_{yy}(i\omega_c) & \alpha_{yy}^{(1)} G_{yy}(i(\omega_c - \omega_T)) \\ \alpha_{yy}^{(-1)} G_{yy}(i\omega_c) & \alpha_{yy}^{(0)} G_{yy}(i(\omega_c - \omega_T)) \end{bmatrix} \right\} = 0 \quad (3.39)$$

This explains the difference between stability lobes of traditional chatter and multi frequency solution. As mentioned before, the minimum stable depth of cut at 38000 rpm is obtained around $\omega_{c,MFS} = 950Hz$ which is the frequency at the intersection of $G_{yy}(\omega)$ and $G_{yy}(\omega - \omega_T)$ (see Figure 3.14). Traditional chatter stability equation ($h_r=0$) is solved in order to see the difference between these two solutions and the chatter frequency is obtained as $1026.4 Hz$, which is quite different than $950 Hz$. In fact, time domain simulation results given in Figure 3.12 clearly show that the chatter occurs around $\omega_T/2 = 950Hz$.

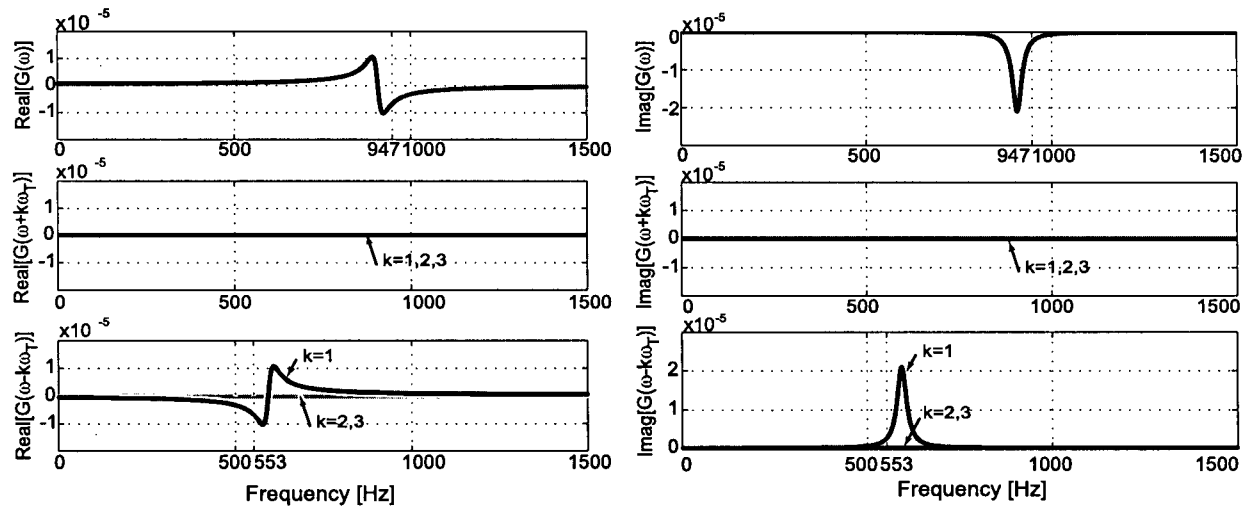


Figure 3.13 : Real and Imaginary Parts of Transfer Function, $h_r=3$, 30000 rpm ($\omega_T = 1500Hz$).

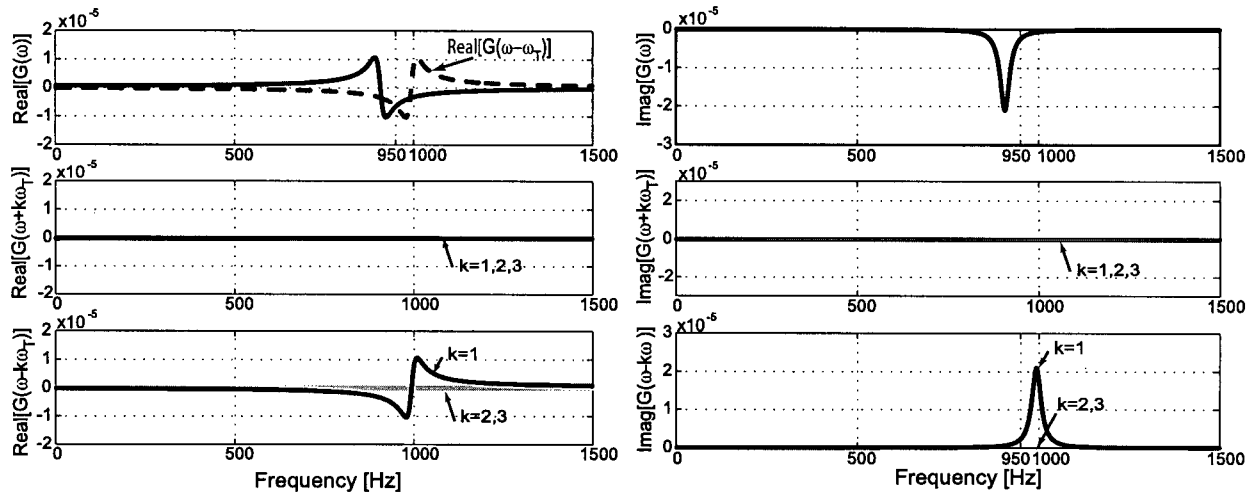


Figure 3.14 : Real and Imaginary Parts of Transfer Function, $h_r=3$, 38000 rpm ($\omega_T = 1900\text{Hz}$).

3.5.2. Low Radial Width of Cut II (One Dimensional - X only)

In this example, face milling with low radial immersion is analyzed (see Figure 3.15). The flexibility of the machine tool can be assumed to appear only in feed (X) direction provided that the flexibilities in both X and Y directions are in the same order of magnitude or the Y direction is comparatively stiffer. In this case, stability equation (Eq.(3.25)) reduces to:

$$\det \left\{ [I] + \Lambda \frac{N}{2\pi} [G_{o,xx}] \right\} = 0 \quad (3.40)$$

where

$$[G_{o,xx}] = \begin{bmatrix} \alpha_{xx}^{(0)} G_{xx}(i\omega_c) & \alpha_{xx}^{(-1)} G_{xx}(i(\omega_c + \omega_T)) & \dots & \dots \\ \alpha_{xx}^{(1)} G_{xx}(i\omega_c) & \alpha_{xx}^{(0)} G_{xx}(i(\omega_c + \omega_T)) & \dots & \dots \\ \alpha_{xx}^{(-1)} G_{xx}(i\omega_c) & \alpha_{xx}^{(-2)} G_{xx}(i(\omega_c + \omega_T)) & \dots & \dots \\ \dots & \dots & \dots & \alpha_{xx}^{(0)} G_{xx}(i(\omega_c - h_r \omega_T)) \end{bmatrix} \quad (3.41)$$

Stepan et al. & Bayly et al. [44] worked on same type of problem. Their experimental set-up was designed to mimic the single degree-of-freedom system with following dynamic parameters: stiffness $k_x = 2.2 \times 10^6 \text{ N/m}$, natural frequency $\omega_n = 146.5 \text{ Hz}$ and damping $\zeta_x = 0.0032$. In this example, same parameters are used in order to compare the results of the proposed model against their simulation results (Figure 3.16). Rest of the parameters used for simulation are: 1-flute cutter with a diameter of 19.05 mm, feed rate = 0.102 mm/rev.flute, cutting force coefficients $K_t = 5.5 \times 10^8 \text{ N/mm}^2$ and $K_r = 0.364$.

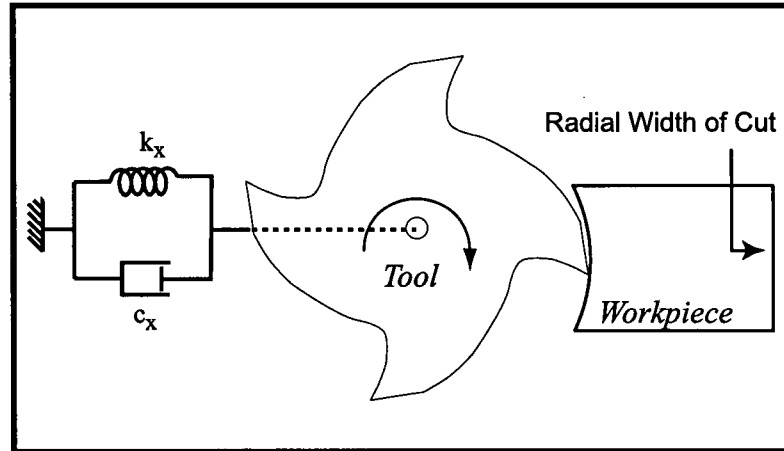


Figure 3.15 : Low Immersion Centre Milling.

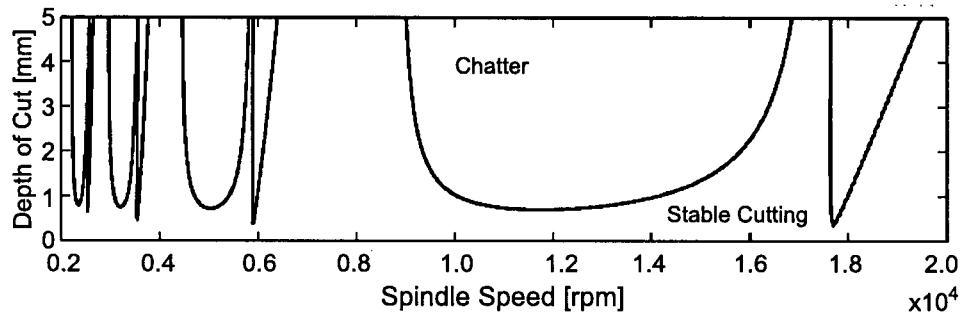


Figure 3.16 : Stability Lobes by Stepan & Bayly et al. [44].

Multi frequency solution is obtained by considering up to five harmonics of tooth passing frequency, $h_r=5$. The detailed portion of the resulting stability lobe is presented in Figure 3.17 along with the traditional stability ($h_r = 0$) and the one obtained in [44]. The Multi Frequency Solution is in good agreement with Stephan & Bayly's stability lobe. The added lobe, which does not appear in traditional solution, is noticeable around 3500 rpm.

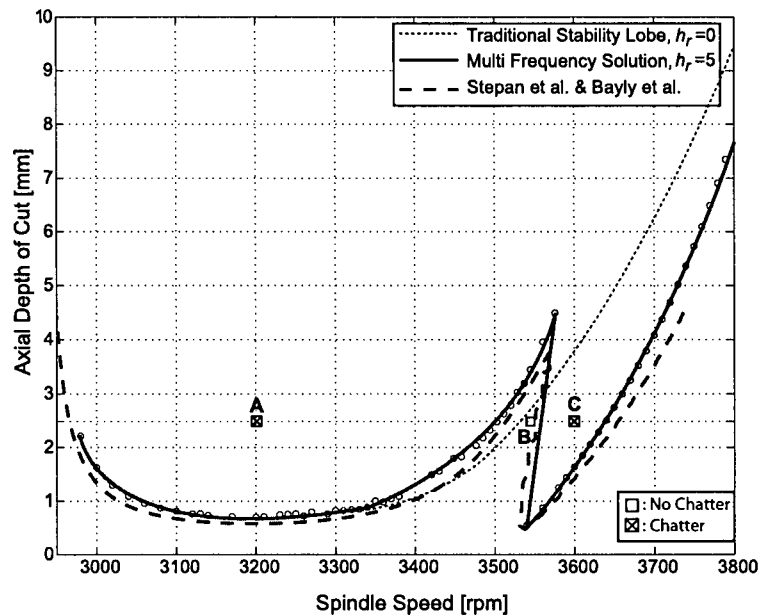


Figure 3.17 : Comparison of Stability Lobes.

Similar to previous example, three different cutting conditions at points *A*, *B* and *C* are simulated in time domain and the cutting force and tool vibration along with their Fast Fourier Transforms are presented in Figures 3.18-3.20, respectively. The judgement of chatter is made based on the ratio of dynamic over static (intended) chip thickness as well as the frequency content of both cutting force and tool vibration. During post-processing, cutting condition was considered to be chattering when the amplification of chip thickness exceeded more than 20% of its static value.

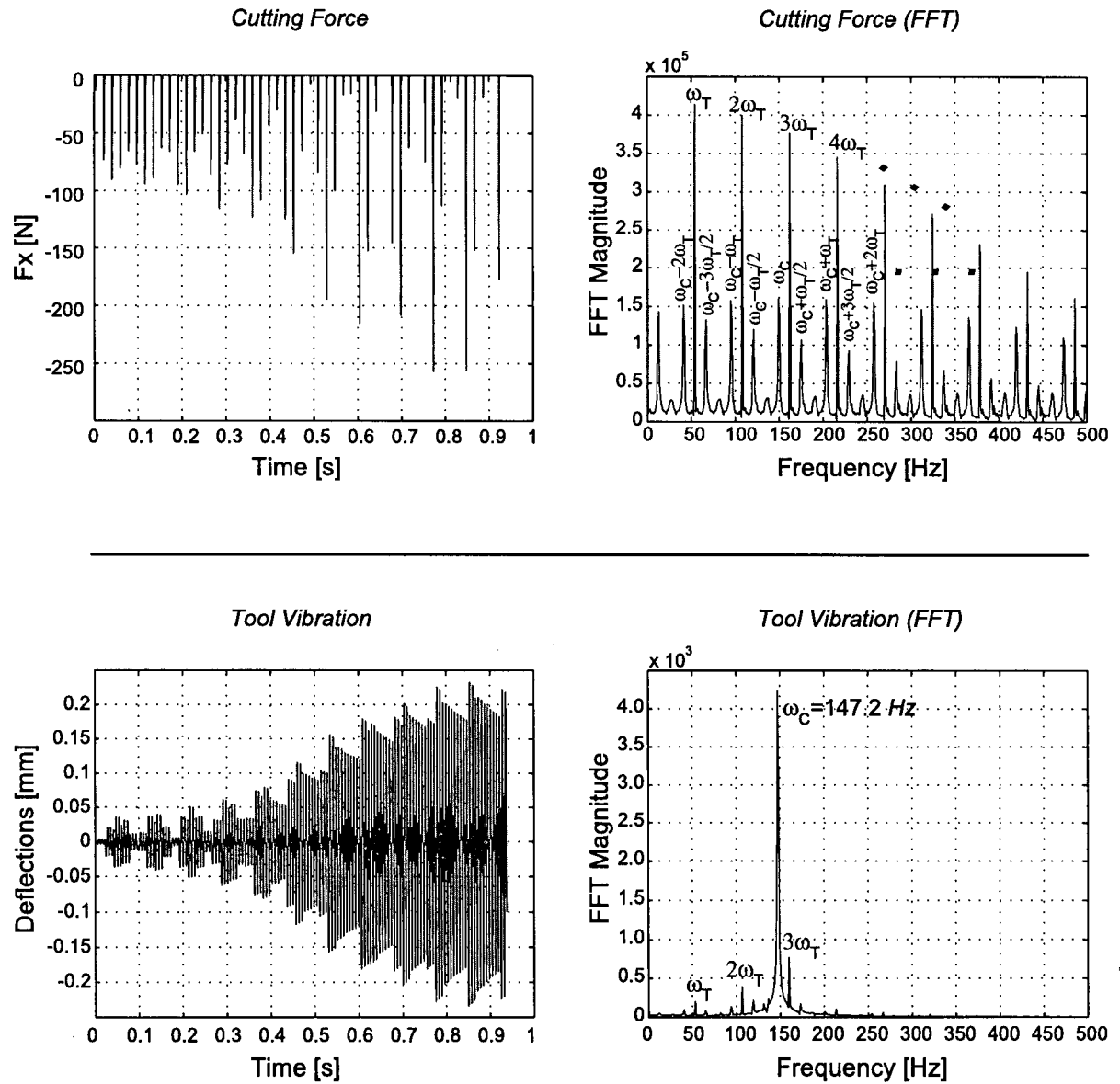


Figure 3.18 : Time Domain Simulation of Cutting Force and Tool Vibration in X direction, Point A: $n=3200 \text{ rpm}$, $a=2.5 \text{ mm}$, Unstable, $\omega_c = 147.2 \text{ Hz}$, $\omega_T = 53.34 \text{ Hz}$.

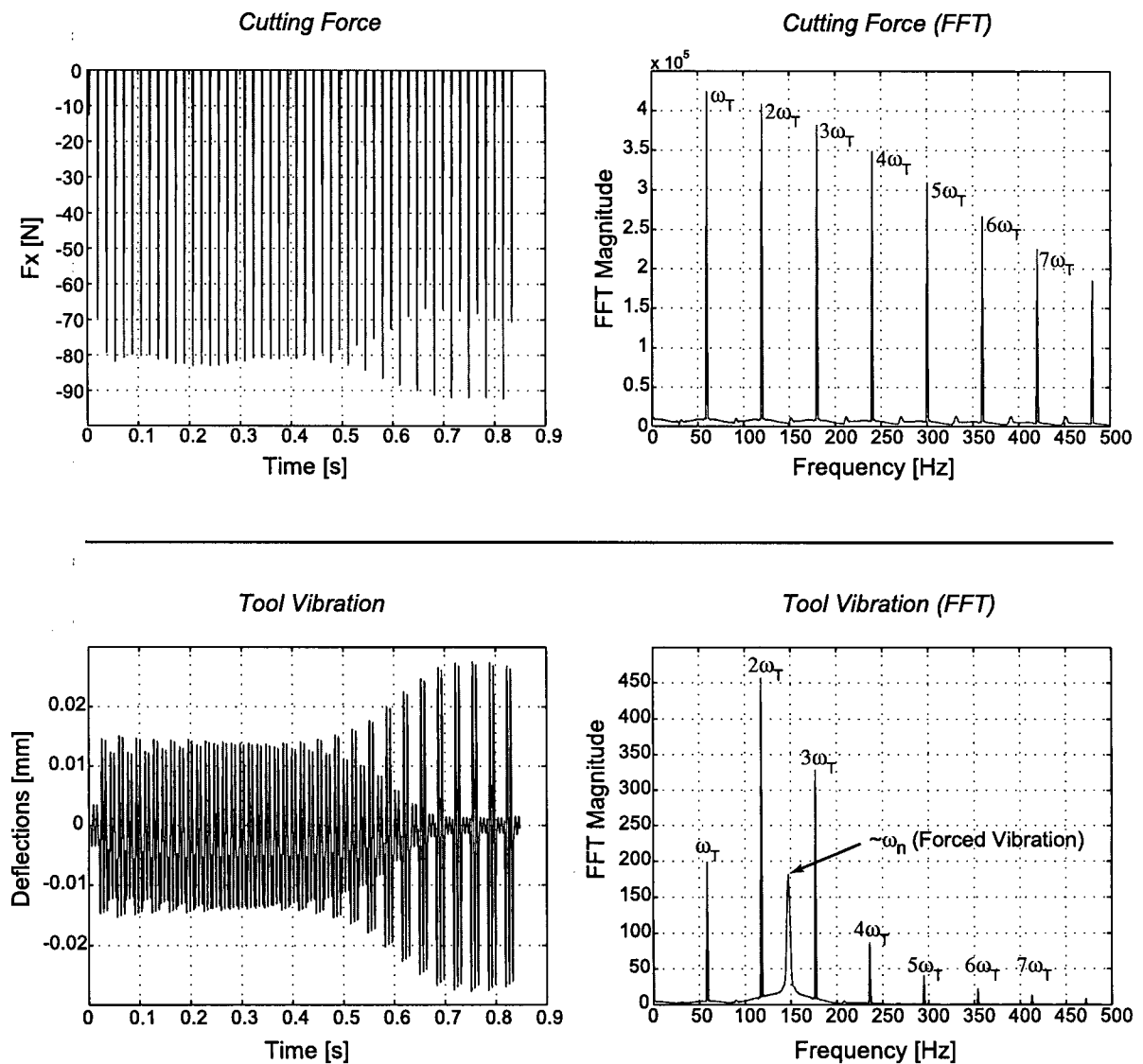


Figure 3.19 : Time Domain Simulation of Cutting Force and Tool Vibration in X direction, Point B: $n=3540$ rpm, $a=2.5$ mm, Stable, $\omega_T = 59\text{Hz}$.

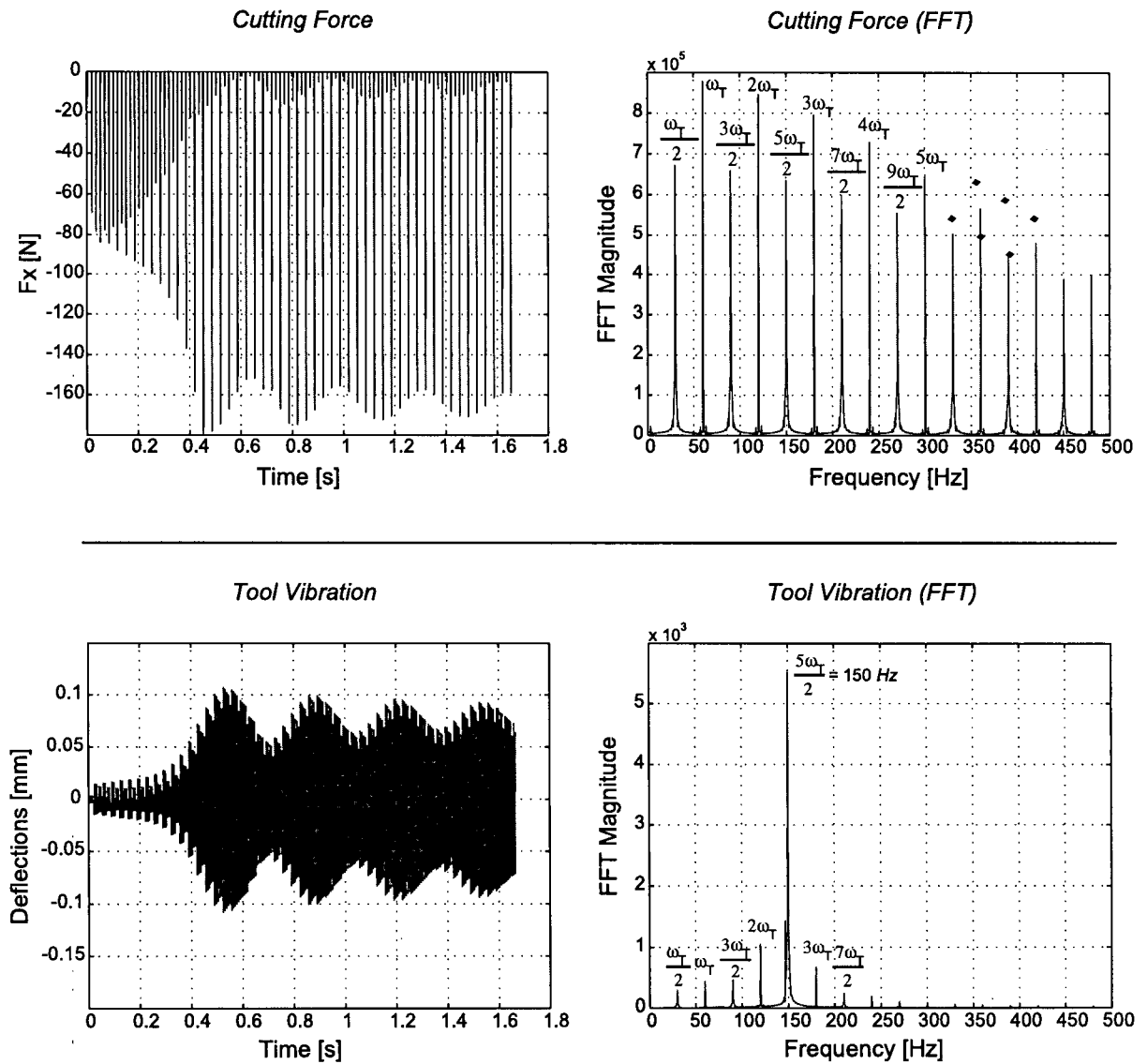


Figure 3.20 : Time Domain Simulation of Cutting Force and Tool Vibration in X direction, Point C: $n=3600$ rpm, $a=2.5$ mm, Unstable, $\omega_T = 60$ Hz.

Note that chatter vibrations occur at 150 Hz which is close to the dominant mode at 146.5 Hz

3.6. Further Analysis on Number of Harmonics

The harmonics of the transfer function is nothing but the shifted form of original transfer function along the frequency axis, as shown in Figure 3.6. The amount of shift is a function of tooth passing frequency (ω_T) which is directly related with spindle speed. This explains why the Multi Frequency Solution converges to traditional one at certain spindle speeds and diverges from it at others. When the first example of this chapter entitled "Low Radial Width of Cut I (One Dimensional - Y only)" is considered, the first two added lobes can be seen around approximately 12000 and 36000 rpm (see Figure 3.8). Earlier, it was commented that the interaction between original and harmonic transfer functions generated the added stability lobe, and the chatter frequency around that spindle speed was obtained to be at the intersection frequency of the real part of those transfer functions as shown in Figure 3.14. This section aims to elaborate on the effect of the number of harmonics on added stability lobe.

Figure 3.21 shows the real part of the transfer functions at a specific spindle speed which the real part of original transfer function intersects with that of the first negative harmonic transfer function ($h_r = -1$) at their minimums. Based on the information given above, chatter frequency for this case becomes:

$$\omega_c = \omega_n(1 + \zeta) \quad (3.42)$$

where ω_n is the natural frequency and ζ is the damping ratio. Inserting values of dynamic parameters, the chatter frequency for this spindle speed is determined as $\omega_c = 922.42 \text{ Hz}$.

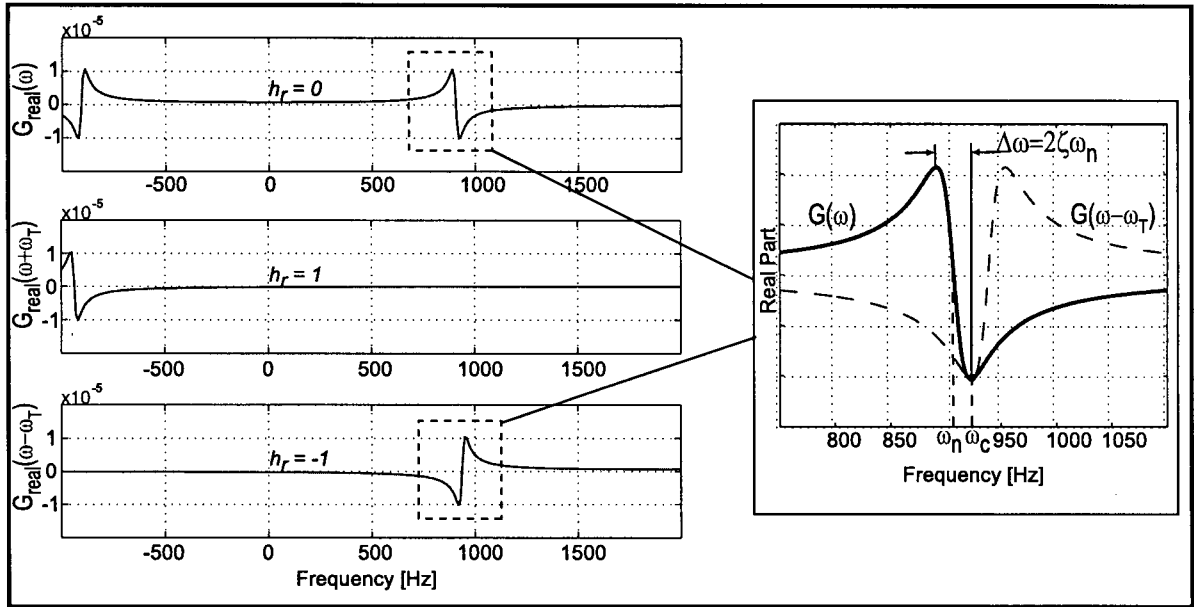


Figure 3.21 : Real part of Transfer Function and its Harmonics at 36897 rpm.

The next step is to identify the spindle speed at which this added lobe is generated. The following relation must be satisfied in order for the special condition presented in Figure 3.21 to happen;

$$|h_r|\omega_T = 2\omega_n + \Delta\omega \quad (3.43)$$

where h_r is the harmonic number, ω_T is the tooth passing frequency and $\Delta\omega = 2\zeta\omega_n$. Replacing tooth passing frequency with $\omega_T = (nN)/60$ where Ω is the spindle speed in (rpm) and N is the total number of flutes, the spindle speed can be solved as:

$$n = 2 \times \frac{60\omega_n(1 + \zeta)}{|h_r|N} \quad (3.44)$$

Finally the spindle speed is obtained as $n=36897 \text{ rpm}$. For verification purposes, the time domain simulation is run at this spindle speed, chatter frequency is obtained as $\omega_{c, TDS} = 917 \text{ Hz}$ which is closed to $\omega_c = 922.42 \text{ Hz}$.

Eq. (3.44) shows the relationship between the spindle speed and the harmonic number. The interpretation of it can be as follows; when h_r is even, the spindle speed corresponds to traditional stability lobe spindle speed; however, when it is odd, a new set of spindle speeds corresponding to added lobe spindle speeds is obtained. Another important outcome of this equation is that the minimum number of harmonics needed to obtain the added lobe at spindle speed n must be h_r . For example, if the stability (Eq. (3.25)) is solved including the first harmonics ($h_r = 1, -1$), only the added lobe at $n=36897 \text{ rpm}$ can be obtained. The next added lobe is obtained by taking at least 3 harmonics into account, i.e. $h_r = 3, -3$, which will lead to spindle speed of $n=12298 \text{ rpm}$. More values can be found in Table 3.1. However, note that the accuracy of the solution meaning the value of minimum axial depth of cut still increases as the number of harmonics is increased as shown earlier in Figure (3.5).

Table 3.1 : Spindle Speed vs Number of Harmonics
($\omega_n = 907 \text{ Hz}$, $\zeta = 0.017$ and $N = 3$).

$ h_r $	Traditional Spindle Speed [rpm]	Added Lobe Spindle Speed [rpm]
1		36897
2	18448	
3		12298
4	9224	
5		7379
\vdots	\vdots	\vdots

Chapter 4

Geometric Modeling of Serrated Cutters

4.1. Introduction

Serrated cutters have more complex geometry compared to the regular cutters like end mills. There is a wide range of serrated cutters with different serration profiles currently used in industry. In this chapter, a mathematical model of a serrated cutter with a general end mill geometry (cylindrical, ballend, tapered,...) and cutting flutes with serrations are introduced. The derivation of the mathematical models is given in the order of increasing complexity. In order to generalize the solution and handle different type of serration profiles, spline fitting technique is used along the cutting flutes.

After the derivation steps, the models are programmed and discretized along the cutter axis to obtain the geometric model which is later going to be used for the force calculations.

4.2. Serrated Cutter with Straight Flutes

The serrated cutters are three dimensional due to not only helix angle but also serrations perpendicular to the axis of the cutter, therefore, the geometric modeling should be three dimensional as well. Before introducing three dimensional solution, it is more convenient to start with a simpler model, two dimensional model where the helix angle is assumed to be zero which inherently assumes that the flutes are straight.

In general, the tooth profile of a serrated cutter is a smooth, periodic function. Smooth profile, i.e. the one without any sharp portions like corners, is easy to grind and prevents the breakage of the serrations due to stress concentration. A typical tooth profile is shown in Figure 4.1. Two important parameters necessary to define this curve are amplitude of the serration wave (a) and wave length of it (L).

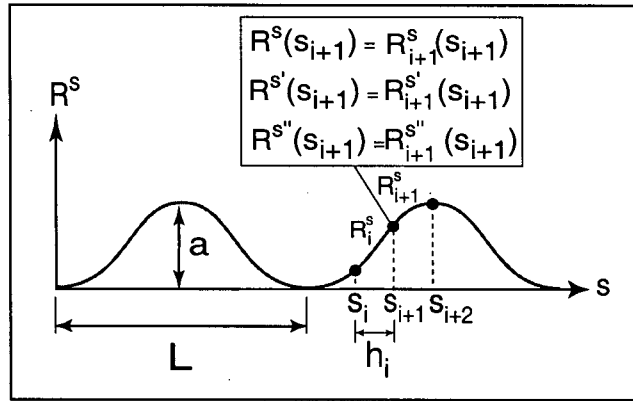


Figure 4.1 : Typical Serrated Cutter Tooth Profile.

In order to generalize the solution and design of cutting edge profile, a spline is fitted for a number of points given along the curve. The spline construction is well defined by Onwubiko [33]. The cubic spline can be expressed as,

$$R_i^s(s) = a_i + b_i(s - s_i) + c_i(s - s_i)^2 + d_i(s - s_i)^3, \quad i = 0, 1, 2, \dots, n-1 \quad (4.1)$$

The points s_i are known as knots and the each curve segment between (s_i, s_{i+1}) is called span (R_i^s). In order to solve for the coefficients, a_i , b_i , c_i and d_i , the coordinates (Eq. (4.3)), the

slopes (Eq. (4.4)) and the curvatures (Eq. (4.5)) at the meeting points of the spline segments should be equal. These conditions are mathematically expressed as follows:

$$R_i^s(s_i) : \text{given as an input, } i = 0, 1, \dots, n \quad (4.2)$$

$$R_{i+1}^s(s_{i+1}) = R_i^s(s_{i+1}), \quad i = 0, 1, \dots, n-2 \quad (4.3)$$

$$\frac{d}{ds}[R_{i+1}^s(s_{i+1})] = \frac{d}{ds}[R_i^s(s_{i+1})], \quad i = 0, 1, \dots, n-2 \quad (4.4)$$

$$\frac{d^2}{ds^2}[R_{i+1}^s(s_{i+1})] = \frac{d^2}{ds^2}[R_i^s(s_{i+1})], \quad i = 0, 1, \dots, n-2 \quad (4.5)$$

Making use of Eqs. (4.2) and (4.3):

From Eq. (4.1), a typical single span of the spline at the two end points (s_i, s_{i+1}) is expressed as,

$$R_i^s(s_i) = a_i \quad (4.6)$$

$$R_i^s(s_{i+1}) = a_i + b_i h_i + c_i h_i^2 + d_i h_i^3 \quad (4.7)$$

where $h_i = s_{i+1} - s_i$. Note that a_i for $i = 0, 1, \dots, n$ is known because it is given as input in the beginning (Eq. (4.2)).

For the successive span of the spline, Eq. (4.6) can be expressed as,

$$R_{i+1}^s(s_{i+1}) = a_{i+1} \quad (4.8)$$

Putting Eqs. (4.7) and (4.8) into (4.3) leads to

$$a_{i+1} = a_i + b_i h_i + c_i h_i^2 + d_i h_i^3 \quad (4.9)$$

Making use of Eq. (4.4):

Differentiation of Eq. (4.1) gives

$$R_i^{s'}(s) = \frac{d}{ds}[R_i^s(s)] = b_i + 2c_i(s - s_i) + 3d_i(s - s_i)^2 \quad (4.10)$$

Once again defining a typical single span of the spline at the two end points (s_i, s_{i+1}) gives

$$R_i^{s'}(s_i) = b_i \quad (4.11)$$

$$R_i^{s'}(s_{i+1}) = b_i + 2c_i h_i + 3d_i h_i^2 \quad (4.12)$$

For the successive span of the spline, Eq. (4.11) is defined as

$$R_{i+1}^{s'}(s_{i+1}) = b_{i+1} \quad (4.13)$$

Substituting Eqs. (4.12) and (4.13) in (4.4) leads to

$$b_{i+1} = b_i + 2c_i h_i + 3d_i h_i^2 \quad (4.14)$$

Making use of Eq. (4.5):

The curvature of spline is simply the second derivative of Eq. (4.1) with respect to parameters which is

$$R_i^{s''}(s) = \frac{d^2}{ds^2}[r_i(s)] = 2c_i + 6d_i(s - s_i) \quad (4.15)$$

A similar procedure with Eq. (4.5) yields to

$$c_{i+1} = c_i + 3d_i h_i \quad (4.16)$$

Solving d_i from Eq.(4.16), substituting into Eqs. (4.9) and (4.14) and solving for b_i gives

$$b_i = \frac{(a_{i+1} - a_i)}{h_i} - \frac{h_i(2c_i + c_{i+1})}{3} \quad (4.17)$$

Note that so far the boundary conditions for spans $R_i^s(s)$ and $R_{i+1}^s(s)$ are applied. If the similar boundary conditions are applied for the spans $R_{i-1}^s(s)$ and $R_i^s(s)$, in the end b_i is solved as

$$b_i = \frac{a_i - a_{i-1}}{h_{i-1}} + \frac{h_{i-1}(c_{i-1} + 2c_i)}{3} \quad (4.18)$$

Finally, equating Eqs. (4.17) and (4.18) yields to the following recursive equation,

$$h_{i-1}c_{i+1} + 2(h_{i-1} + h_i)c_i + h_ic_{i+1} = 3\left(\frac{a_{i+1} - a_i}{h_i} - \frac{a_i - a_{i-1}}{h_{i-1}}\right), \quad i = 1, 2, \dots, n-1 \quad (4.19)$$

Note that the Eq. (4.19) can not be solved unless two additional equations are specified, because the number of unknowns, $n+1$, is two more than the number of equations, $n-1$. These two necessary equations are called boundary conditions of the problem. Possible boundary conditions are:

(i) Natural Spline Boundary Conditions

$$\frac{d^2}{ds^2}[R^s(s_0)] = \frac{d^2}{ds^2}[R^s(s_n)] = 0 \quad (4.20)$$

(ii) Clamped Spline Boundary Conditions

$$\frac{d}{ds}[R^s(s_0)] = BC_1, \quad \frac{d}{ds}[R^s(s_n)] = BC_2 \quad (4.21)$$

Since the derivatives (or slopes) at the end points are known for a desired tooth profile, "clamped spline boundary conditions" are used during design of serrated cutters. Sample profiles for this set of boundary conditions are given in Figure 4.2. Depending on the cutter profile, boundary conditions are selected. For example, the boundary conditions for case (a) in Figure 4.2. will be $BC_1 = 0.0$, $BC_2 = 0.0$, and the ones for case (b) will be $BC_1 = \tan \alpha_1$, $BC_2 = -\tan \alpha_2$.

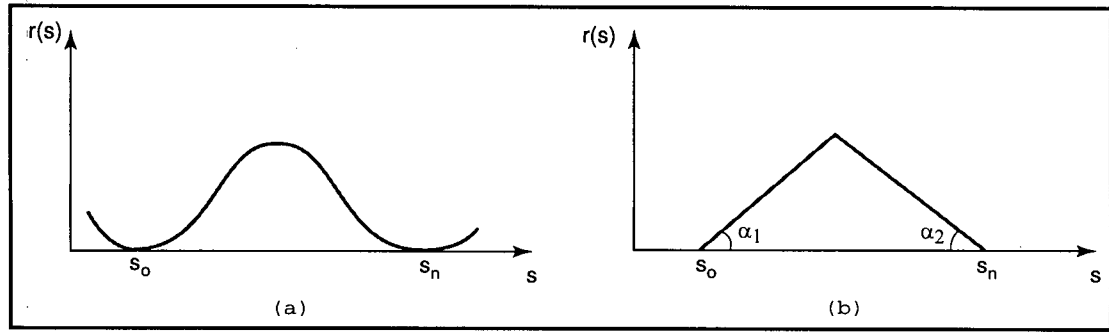


Figure 4.2 : Clamped Spline Examples.

Note that in this part, the effect of helix is ignored, therefore, the flutes are straight along the cutter body. The straight flute cutter can be represented as shown in Figure 4.3. The radial direction (r) shown in Figure 4.3.b is a vector pointing outwards in x-y plane. The radius of the cutter at each point along the cutter axis can be expressed as,

$$R(z) = \frac{D}{2} - R^s(z) \quad (4.22)$$

where D is the main diameter of the cutter. Note that, since the helix angle is assumed to be zero, s -direction in Figure 4.1. coincides with the cutter axis.

The x and y coordinates of the flute at any point along the cutter axis becomes

$$\begin{aligned} X_i(z) &= R(z) \sin \phi_i(z) \\ Y_i(z) &= R(z) \cos \phi_i(z) \end{aligned} \quad (4.23)$$

where ϕ_i (see Figure 4.4.) is the radial immersion of point P on flute number i . The radial immersion (ϕ_i) varies as a function of rotation angle (ϕ_0), flute position (ϕ_{pi}) and the local helix angle at point P ($\psi(z)$).

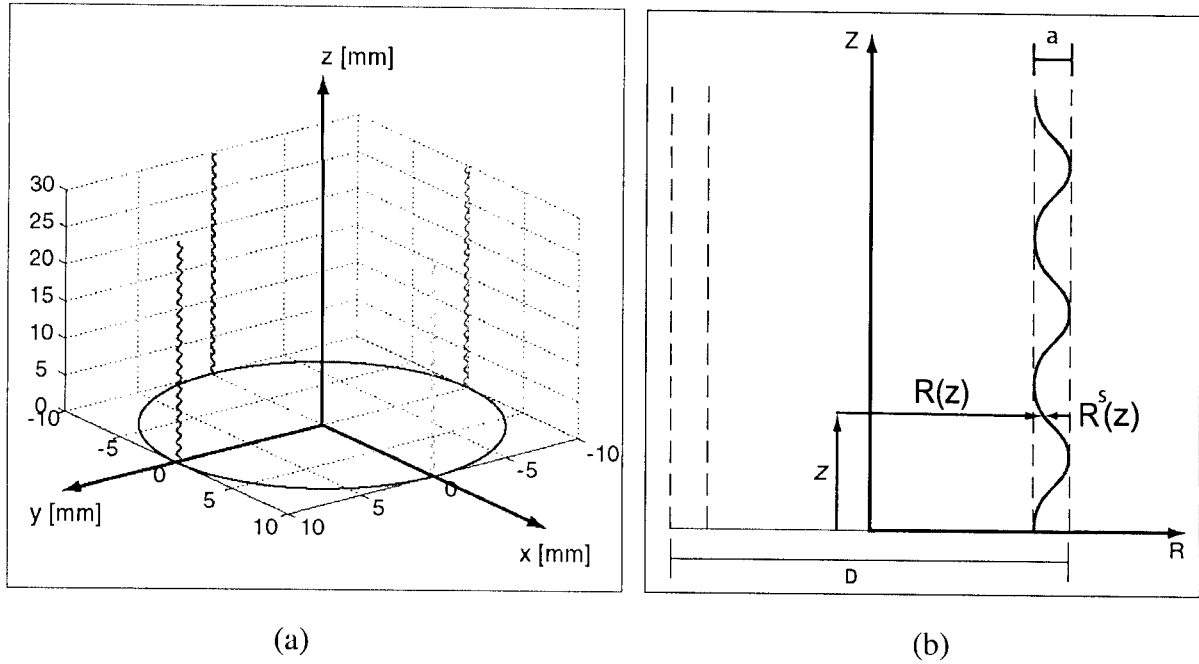


Figure 4.3 : Representation of a Straight Flute Milling Cutter.

From Figure 4.4.,

$$\phi_i(z) = \phi_0 + \phi_{pi} - \psi(z) \quad (4.24)$$

where ϕ_{pi} is the pitch angle between the preceding flutes. For a regular pitch cutter, pitch angle is defined as, $\phi_{pi} = \frac{2\pi}{N}i$, where N is the number of flutes and $i = 0, 1 \dots N-1$.

Note that, for straight flute milling cutter, the local helix angle at any point along the cutter will be,

$$\psi(z) = 0.0 \quad (4.25)$$

In Figure 4.4., P represents any point on the cutter along the flute i and F represents the beginning of that flute which is located at the tip of the cutter.

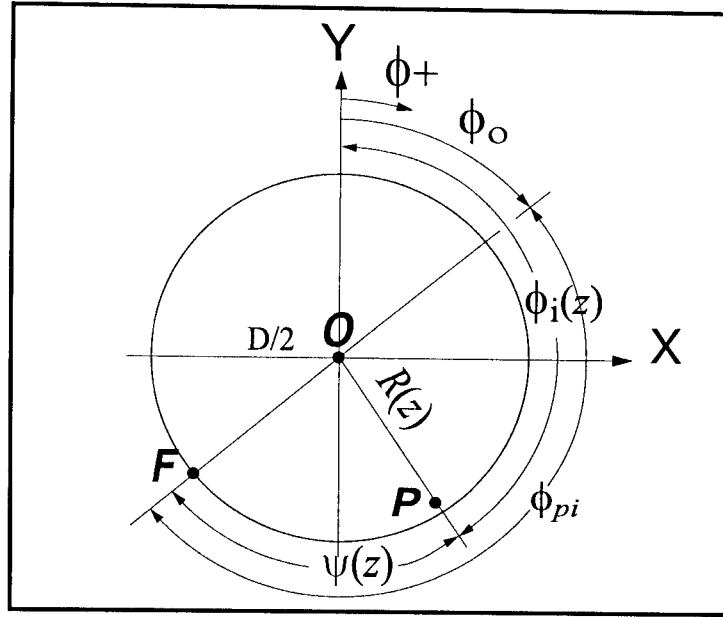


Figure 4.4 : Angle Representations.

4.3. Serrated Cutter with Helical Flutes

The effect of the helix was not added to the geometric model of a general cylindrical serrated cutter in the previous section, which will be considered in this section.

The helix on the cutter makes the flute rotate around the cutter body, i.e., the s -direction being *along the flute* does not coincide with the cutter axis anymore. Figure 4.5. shows the geometric

relation between the axis along the curved helical flute (s -direction) and cutter body axis. Following this geometric relation,

$$s = \frac{z}{\cos i_0} \quad (4.26)$$

where i_0 is the helix angle. As opposed to straight flute discussed in the previous section, the angular position of each axial element on a flute will be different due to helical shape. The angular position for an axial element on flute i at elevation z is defined in Eq.(4.24). For this cutter, the local helix angle is defined as,

$$\psi(z) = k_\mu z \quad (4.27)$$

where

$$k_\mu = \frac{\tan i_0}{\left(\frac{D}{2}\right)} \quad (4.28)$$

Finally, the angular position for an axial element on flute i at elevation z becomes,

$$\phi_i(z) = \phi_0 + \phi_{pi} - k_\mu z \quad (4.29)$$

The vector from the centre of the cutter to an arbitrary point on the flute, shown in Figure 4.5., can be determined as,

$$\mathfrak{R} = R_x i + R_y j + R_z k \quad (4.30)$$

where $R_x = R(z)\sin\phi_i(z)$, $R_y = R(z)\cos\phi_i(z)$, $R_z = z$.

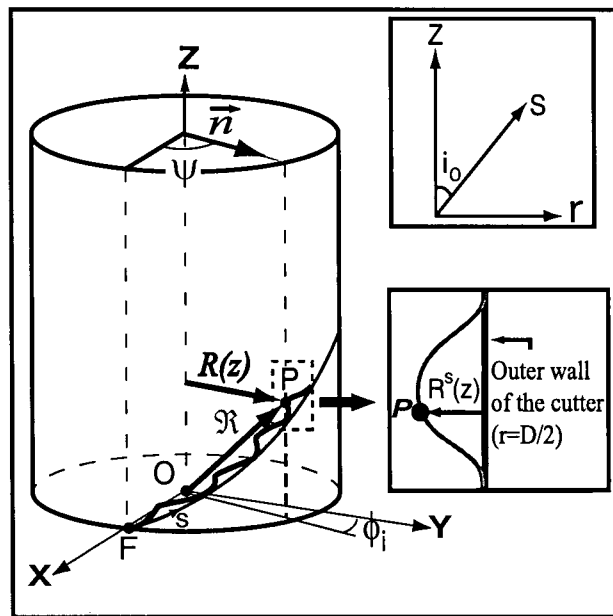


Figure 4.5 : Important Vectors for Mathematical Model of a Cylindrical Cutter.

The vector representation of the curve, i.e. Eq. (4.31), is more convenient during the derivation of geometry.

$$\mathfrak{R}(z) = \begin{Bmatrix} x \\ y \\ z \end{Bmatrix} = \begin{Bmatrix} R(z) \sin \phi_i(z) \\ R(z) \cos \phi_i(z) \\ z \end{Bmatrix} \quad (4.31)$$

Note that, the vector form given above is able to define all the points on the flute in 3-D space, i.e. surface of the cutter. The simulated cutter geometry is given in Figure 4.6.

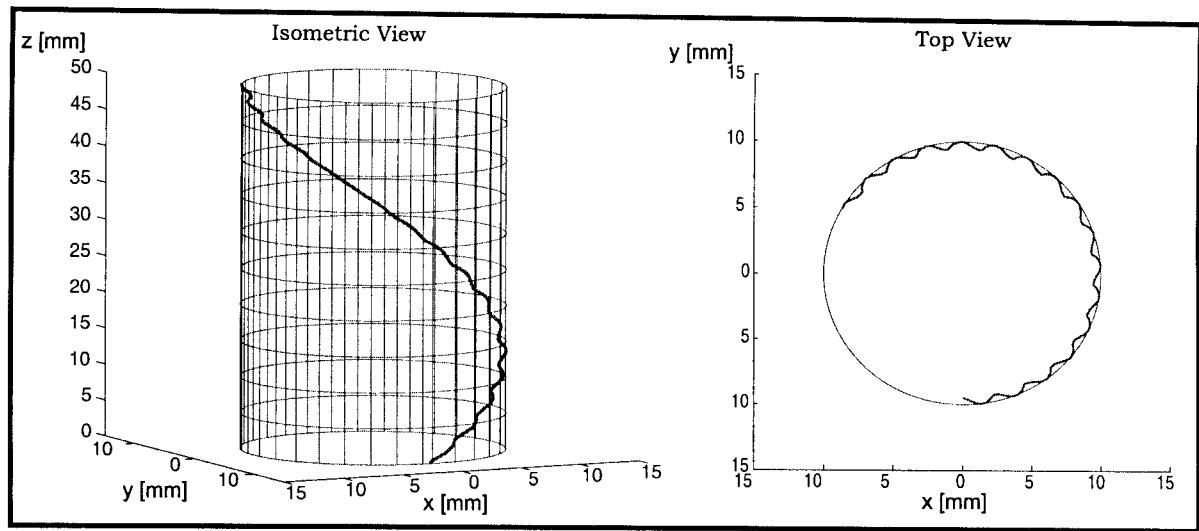
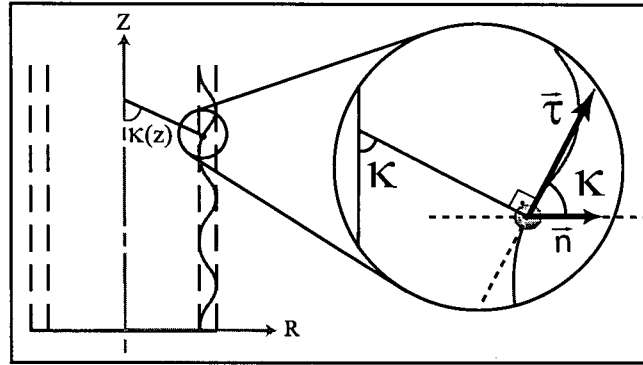


Figure 4.6 : Simulated Cylindrical, Helical Serrated Cutter.

Having determined the geometry of the serrated cutter analytically, it is also possible to express the axial immersion angle (κ), which is necessary for the force calculations and shown in Figure 4.7.

Figure 4.7 : Schematic Representation of κ Angle.

The vector tangent to the surface being in the direction of tangent line can be determined by using Eq. (4.31) as,

$$\vec{\tau}(z) = \frac{d}{dz} \mathcal{R}(z) \quad (4.32)$$

$$\vec{\tau}(z) = \begin{Bmatrix} \cos(\phi_i(z))(-k_\mu)R(z) \\ (-\sin(\phi_i(z)))(-k_\mu)R(z) \\ 1 \end{Bmatrix} + \begin{Bmatrix} \sin(\phi_i(z))\frac{d}{dz}R(z) \\ \cos(\phi_i(z))\frac{d}{dz}R(z) \\ 0 \end{Bmatrix} \quad (4.33)$$

On the other hand, the unit vector pointing outward (\vec{n}) in xy plane can be expressed as,

$$\vec{n}(z) = \begin{Bmatrix} \sin(\phi_i(z)) \\ \cos(\phi_i(z)) \\ 0 \end{Bmatrix} \quad (4.34)$$

From the property of the scalar multiplication of the normal and tangent vectors,

$$\vec{\tau}(z) \bullet \vec{n}(z) = |\vec{\tau}(z)| |\vec{n}(z)| \cos \kappa$$

The axial immersion angle (κ) is found as,

$$\kappa = \arccos \left[\frac{\vec{\tau}(z) \bullet \vec{n}(z)}{|\vec{\tau}(z)|} \right] \quad (4.35)$$

where $\vec{n}(z)$ is a unit normal vector.

From Eqs. (4.33) and (4.34),

$$\vec{\tau}(z) \bullet \vec{n}(z) = \frac{d}{dz} R(z) \quad (4.36)$$

and

$$|\vec{\tau}(z)| |\vec{n}(z)| = \sqrt{\left[\frac{d}{dz} R(z) \right]^2 + [R(z)]^2 k_\mu^2 + 1} \quad (4.37)$$

By substituting them into Eq. (4.35), κ is obtained as,

$$\kappa(z) = \text{acos} \left[\frac{\frac{d}{dz}R(z)}{\sqrt{\left[\frac{d}{dz}R(z)\right]^2 + [R(z)]^2 k_\mu^2 + 1}} \right] \quad (4.38)$$

The radius of the cutter at each axial element, i.e. $R(z)$, was given in Eq. (4.22). Therefore,

$$\frac{d}{dz}R(z) = \frac{d}{dz}\left(\frac{D}{2} - R^s(z)\right) = -\frac{d}{dz}(R^s(z)) \quad (4.39)$$

Considering the Eq. (4.26),

$$\frac{d}{dz}R^s(z) = \left(\frac{ds}{dz}\right) \frac{d}{ds}R^s(s) \Rightarrow \frac{d}{dz}R(z) = \left(\frac{-1}{\cos i_0}\right) \frac{d}{ds}R^s(s) \quad (4.40)$$

4.4. Tapered Helical Ball End Mill with Serrated Flutes

There are two commonly used tapered end mills either having a *constant helix with varying lead length* or *constant lead length with varying helix angle along the taper*. The smooth, periodic serrations are imposed on the flute along the taper with half-apex taper angle (β) as shown in Figure 4.8.

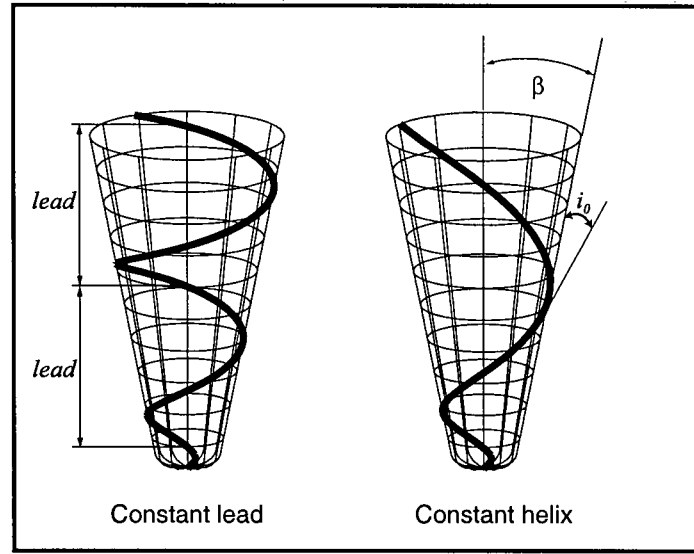


Figure 4.8 : Constant Lead, Constant Helix Tapered End Mills.

4.4.1. Constant Helix Case

On a tapered tool, the helix angle (i_0), shown in Figure 4.8., is defined as the angle between the tangent and the slanted axis passing through a certain point on the cutting edge [34].

The angular position (polar angle) of the vector \Re is defined by extending the definition of constant helix tapered cutter in [34]:

$$\psi(z) = c_1 \ln[1 + c_2(z - z_1)] + \psi_0 \text{ for } z \geq z_1 \quad (4.41)$$

where

$$c_1 = \frac{\tan i_0}{\sin \beta} \quad (4.42)$$

$$c_2 = \frac{\tan \beta}{R_0} \quad (4.43)$$

z_1 is the height of the general end mill and ψ_0 is the lag angle due to the general end shape between $0 \leq z \leq z_1$.

Note that, in Eq. (4.41), the geometry is defined for $z \geq z_1$ where the portion between $0 \leq z \leq z_1$ could be occupied by any type of general end shape like ball end.

Considering ball end mill, the polar angle (or the lag angle) is expressed as [35]:

$$\psi_b(z) = \frac{\tan i_0}{R_{b0}} z \quad \text{for } z \leq z_1 \quad (4.44)$$

where R_{b0} is the ball diameter.

Therefore, for tapered helical ball end mills, the lag angle (ψ_0) due to the portion of the flute on the ball part, which can be seen in Figure 4.9., becomes

$$\psi_0 = \psi_b(z_1) = \frac{\tan i_0}{R_{b0}} z_1 \quad (4.45)$$

This type of end mill is called *Constant Helix Tapered Helical Ball End Mill*. However, if there is no ball end, $z_1 = 0$ and $\psi_0 = 0$.

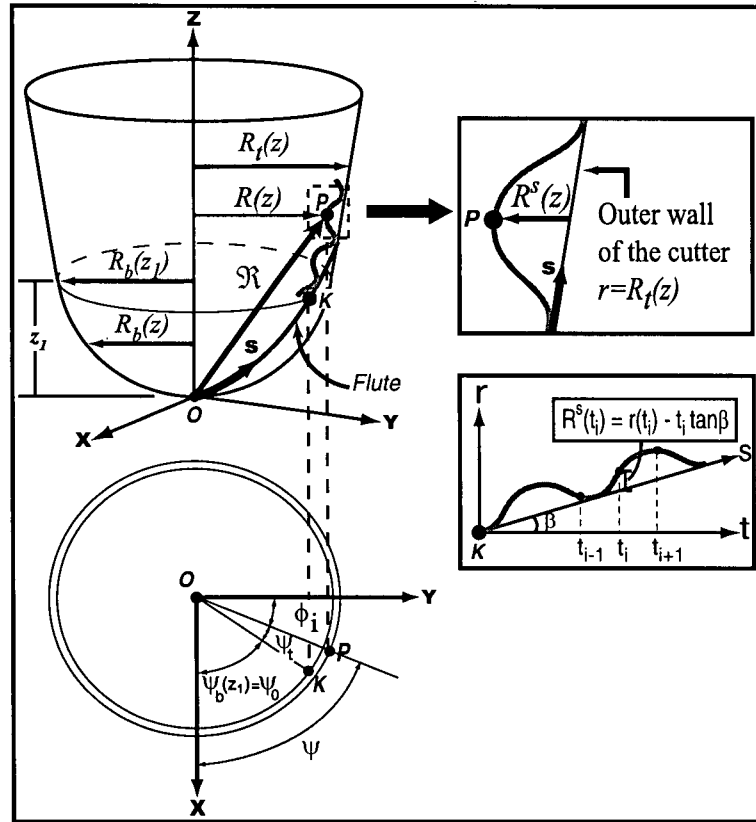


Figure 4.9 : Serrated Tapered Ball End Mill.

The radius of the cutter is changing along the cutter for both tapered and ball parts. The radius for constant helix case along the tapered edge (see Figure 4.9.) is defined as [34]:

$$R_f(z) = [1 + c_2(z - z_1)]R_0 \quad \text{for } z \geq z_1 \quad (4.46)$$

Where as the radius of cutter along the ball part is expressed as [35]:

$$R_b(z) = \sqrt{1 - \left(\frac{z}{R_{b0}} - 1\right)^2} R_{b0} \quad \text{for } z < z_1 \quad (4.47)$$

Note that serrations are imposed only on the taper part. Since the ball part of a tapered ball end mill is small, serrations are ground only on the tapered part. Having said that, the radius along the tapered part with the serration becomes:

$$R(z) = R_t(z) - R^s(z) \quad (4.48)$$

where $R^s(z)$ (shown in Figure 4.9.) is the contribution of the serration and it will be expressed in the later parts of this section.

After expressing all the parameters necessary for the determination of the geometry, the vector \mathfrak{R} in Figure 4.9. can be determined as,

$$\mathfrak{R} = R_x i + R_y j + R_z k \quad (4.49)$$

where

$R_x = R(z) \sin \phi_i(z)$, $R_y = R(z) \cos \phi_i(z)$, $R_z = z$ and $\phi_i(z)$ is the angular position for an axial element on flute i at elevation z ,

$$\phi_i(z) = \phi_0 + \phi_{pi} - \psi(z) \quad (4.50)$$

In vector form, Eq. (4.49) can be expressed as:

$$\mathfrak{R}(z) = \begin{Bmatrix} x \\ y \\ z \end{Bmatrix} = \begin{Bmatrix} R(z) \sin \phi_i(z) \\ R(z) \cos \phi_i(z) \\ z \end{Bmatrix} \quad (4.51)$$

Axial immersion angle (κ) must be defined for the orientation of the forces in the modeling of serrated cutters similar to the definition made for cylindrical serrated cutters before (see Eq. (4.38)).

The vector tangent to the surface, τ (see Figure 4.10.), can be determined as,

$$\dot{\tau} = \frac{d\mathfrak{R}(z)}{dz}$$

Using Eqs. (4.48) and (4.49),

$$\dot{\tau} = \begin{bmatrix} \tau_x \\ \tau_y \\ \tau_z \end{bmatrix} = \begin{bmatrix} \left(\frac{dR_i(z)}{dz} - \frac{dR^s(z)}{dz} \right) \sin \phi_i(z) \\ \left(\frac{dR_i(z)}{dz} - \frac{dR^s(z)}{dz} \right) \cos \phi_i(z) \\ 1 \end{bmatrix} + \begin{bmatrix} R(z) \cos \phi_i(z) \frac{d\phi_i(z)}{dz} \\ -R(z) \sin \phi_i(z) \frac{d\phi_i(z)}{dz} \\ 0 \end{bmatrix} \quad (4.52)$$

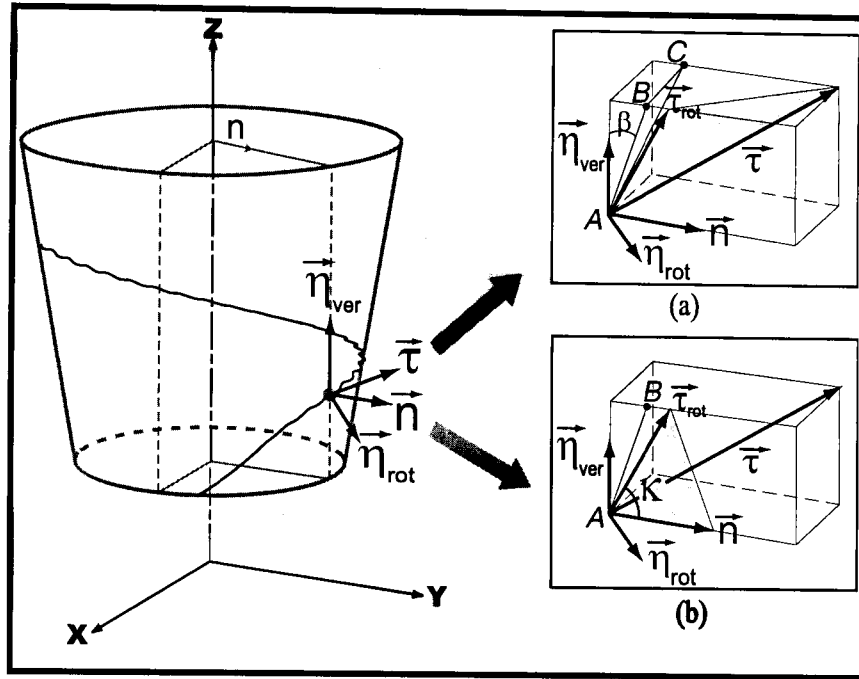


Figure 4.10 : Vector Definitions for Tapered Cutters.

Before mathematical derivations, the vectors and their roles in the determination steps of κ are explained.

In Figure 4.10.:

- (*) Line AB represents the slanted axis of the tapered envelope.
- (*) \vec{n}_{ver} is a vector in the direction of cutter axis, i.e., along z axis.
- (*) \vec{n}_{rot} is a unit vector which is perpendicular to line AB.
- (*) \vec{n} is a vector pointing outwards, i.e. perpendicular to the cutter axis, and in radial direction. This vector is defined in Eq.(4.34).
- (*) $\vec{\tau}_{rot}$ is the rotated form of $\vec{\tau}$ about \vec{n}_{rot} . Note that the rotation takes place in plane shown shaded in Figure 4.10.a. The angle between lines AB and AC is equal to helix angle, i_0 .
- (*) Half-apex taper angle, β , is the angle between line AB and \vec{n}_{ver} .

(*) Axial immersion angle (κ) is the angle between $\vec{\tau}_{rot}$ and \vec{n} . Note that it is defined in the shaded plane shown in Figure 4.10.b.

Combining Eqs.(4.41), (4.46) and (4.52), tangent vector for constant helix tapered serrated cutter is obtained as,

$$\vec{\tau} = \begin{bmatrix} \tau_x \\ \tau_y \\ \tau_z \end{bmatrix} = \begin{bmatrix} \left(c_2 R_0 - \frac{dR^s(z)}{dz}\right) \sin \phi_i(z) \\ \left(c_2 R_0 - \frac{dR^s(z)}{dz}\right) \cos \phi_i(z) \\ 1 \end{bmatrix} + \begin{bmatrix} R(z) \cos \phi_i(z) \left(\frac{-c_1 c_2}{1 + c_2(z - z_1)}\right) \\ -R(z) \sin \phi_i(z) \left(\frac{-c_1 c_2}{1 + c_2(z - z_1)}\right) \\ 0 \end{bmatrix} \quad (4.53)$$

To obtain $\vec{\tau}_{rot}$, the tangent vector, $\vec{\tau}$, is rotated about $\vec{\eta}_{rot}$ by using rotation matrix, $[Rot]$.

$$\vec{\tau}_{rot} = [Rot]_{3 \times 3} \vec{\tau} \quad (4.54)$$

Rotation matrix, $[Rot]$ is defined by Zeid [36] as,

$$[Rot] = \begin{bmatrix} \eta_{rotx}^2 \nu\theta + c\theta & \eta_{rotx} \eta_{roty} \nu\theta - \eta_{rotz} s\theta & \eta_{rotx} \eta_{rotz} \nu\theta + \eta_{roty} s\theta \\ \eta_{rotx} \eta_{roty} \nu\theta + \eta_{rotz} s\theta & \eta_{roty}^2 \nu\theta + c\theta & \eta_{roty} \eta_{rotz} \nu\theta - \eta_{rotx} s\theta \\ \eta_{rotx} \eta_{rotz} \nu\theta - \eta_{roty} s\theta & \eta_{roty} \eta_{rotz} \nu\theta + \eta_{rotx} s\theta & \eta_{rotz}^2 \nu\theta + c\theta \end{bmatrix} \quad (4.55)$$

where $c\theta = \cos\theta$, $s\theta = \sin\theta$ and $v\theta = 1 - \cos\theta$. For our case, the orientation of the axis of rotation is defined by the unit vector which is equal to $\vec{\eta}_{rot}$, and θ is the angle of rotation which is equal to helix angle, i_0 .

Note that $\vec{\eta}_{rot} = \eta_{rotx}\vec{i} + \eta_{roty}\vec{j} + \eta_{rotz}\vec{k}$ and for a tapered body (see Figure 4.11.),

$$\eta_{rotx} = \cos\beta \sin\phi_i(z) \quad (4.56)$$

$$\eta_{roty} = \cos\beta \cos\phi_i(z) \quad (4.57)$$

$$\eta_{rotz} = -\sin\beta \quad (4.58)$$

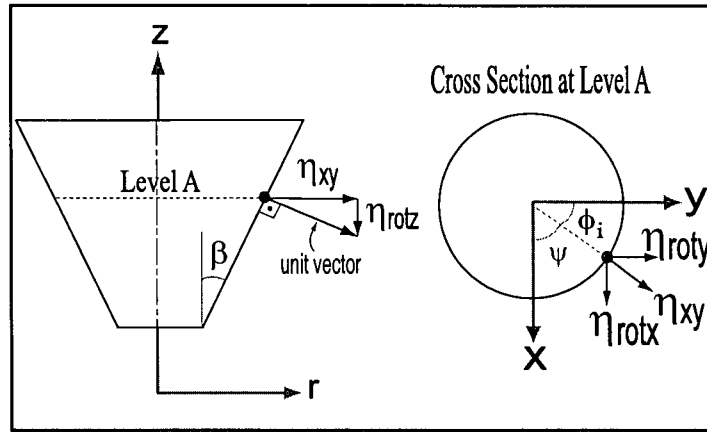


Figure 4.11 : Representation of $\vec{\eta}_{rot}$.

Once $\vec{\tau}_{rot}$ and \vec{n} (Eq. (4.34)) are determined, the axial immersion angle (κ) can be obtained from the scalar multiplication of vectors as stated in Eq. (4.35),

$$\kappa = \arccos \left[\frac{\vec{\tau}_{rot} \cdot \vec{n}}{|\vec{\tau}_{rot}|} \right] \quad (4.59)$$

To summarize steps to be followed for the determination of κ :

- (*) Obtain cutter geometry (Eq. (4.51))
- (*) Determine the tangent vector (Eq. (4.52))
- (*) Rotate the tangent vector (Eq. (4.54)) about an axis (Eqs. (4.56)-(4.58)) to obtain rotated tangent vector
- (*) Determine angle between rotated tangent vector and the unit vector in radial direction (Eq. (4.34)) by using Eq. (4.59)

Mathematical model for $R^s(z)$ in Eq. (4.48) will be handled later on. The notation for the serration is same as shown in Figure 4.1. However, due to the taper angle there are some differences in the derivation part.

According to manufacturer, the serrations are ground along the flute with a tilted grinding wheel ensuring that the grinding wheel is always perpendicular to the flute. Similar to the cylindrical serrated cutter, s-axis shown in Figure 4.1., is the axis along the flute without taking the serrations into account.

The relationship between cutter axis (z) and s-axis can be found by using the arc length. The arc length between z and z_1 is:

$$s = \int_{z_1}^z \sqrt{\left(\frac{dR_{tx}}{dz}\right)^2 + \left(\frac{dR_{ty}}{dz}\right)^2 + \left(\frac{dR_{tz}}{dz}\right)^2} dz \quad (4.60)$$

where $R_{tx} = R_t(z)\sin\phi_t(z)$, $R_{ty} = R_t(z)\cos\phi_t(z)$, $R_{tz} = z$

When the integration in Eq. (4.60) is performed for constant helix tapered cutter,

$$s = \sqrt{(c_2 R_0)^2 (1 + c_1^2) + 1} \cdot (z - z_1) \quad (4.61)$$

Since the envelope of the cutter is not vertical, i.e. there is a taper angle on it, the serrations, which are perpendicular to the flute, have to be rotated as seen in Figure 4.12. in order to obtain the change in radius, i.e. r direction. Note that, in Figure 4.12., EC is the distance before the rotation of spline, where as, DC is the one after the rotation of spline. Since the points are rotated, parameter t is defined for spline fitting, therefore, in Eq. (4.1), instead of " s ", parameter " t " is used (see Figure 4.12.). Note that parameter " t " has no physical meaning.

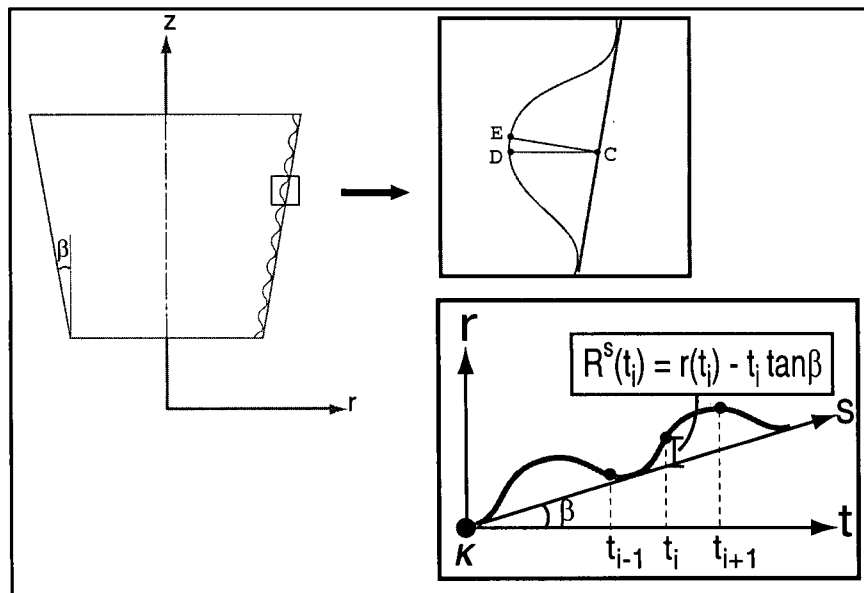


Figure 4.12 : Rotated Spline.

To summarize, unlike cylindrical serration case, the spline points are rotated by half-apex taper angle (β), then the spline is fitted. Then for a given axial height (z), corresponding arc length (s) is found by Eq. (4.60). From that, the corresponding "t" value is found by

$$t = s \cos \beta \quad (4.62)$$

Finally, the contribution of serration (see Figure 4.12.) can be found as

$$R^s(z) = R^s(t) = [r(t) - t \tan \beta] \quad (4.63)$$

where $r(t)$ is the spline fitted to the rotated knots.

Once the relationships between the axes are found, the derivation of serration term in Eq. (4.52) can be found as

$$\frac{d}{dz} R^s(z) = \left[\frac{d}{dt} R^s(t) \right] \frac{dt}{dz} = \left(\frac{d}{dt} r(t) - \tan \beta \right) \frac{dt}{dz} \quad (4.64)$$

For constant helix:

$$\frac{dt}{dz} = \sqrt{(c_2 R_0)^2 (1 + c_1^2) + 1} \cos \beta \quad (4.65)$$

4.4.2. Constant Lead Case

The procedure is similar to the constant helix case which was explained in the section. The only difference is in the equations.

The angular position (polar angle) of the vector \mathfrak{R} is defined by extending the definition of constant lead tapered cutter in [37]:

$$\psi(z) = c_3(z - z_1) + \psi_0 \quad \text{for } z \geq z_1 \quad (4.66)$$

where

$c_3 = \frac{\tan i_s}{R_0}$, $i_s = \text{atan}\left(\frac{2\pi R_0}{\text{lead} \cos \beta}\right)$ (nominal helix angle), ψ_0 defined in Eq. (4.45) and z_1 shown in Figure 4.9.

The radius for constant lead case along the tapered edge is defined as [37]:

$$R_t(z) = [1 + c_2(z - z_1)]R_0 \quad \text{for } z \geq z_1 \quad (4.67)$$

Note that it is equal to the constant helix case. As expected, the radius change along the cutter axis is independent of flute type, i.e. constant helix or lead.

The arc length calculated from Eq. (4.60) for constant lead case is found to be

$$s = \left[\frac{1}{2c_2} \left(\chi \sqrt{(\lambda_1 + \lambda_2 \chi^2)} + \frac{\lambda_1}{\sqrt{\lambda_2}} \ln [\sqrt{\lambda_2} \chi + \sqrt{(\lambda_1 + \lambda_2 \chi^2)}] \right) \right] - S_0 \quad (4.68)$$

where $\chi = 1 + c_2(z - z_1)$, $S_0 = \frac{1}{2c_2} \left(\sqrt{(\lambda_1 + \lambda_2)} + \frac{\lambda_1}{\sqrt{\lambda_2}} \ln(\sqrt{\lambda_2} + \sqrt{(\lambda_1 + \lambda_2)}) \right)$,

$$\lambda_1 = (c_2 R_0)^2 + 1 \text{ and } \lambda_2 = (c_3 R_0)^2$$

And lastly the $\frac{dt}{dz}$ in Eq. (4.64) for constant lead case can be obtained as,

$$\frac{dt}{dz} = \frac{\cos \beta \lambda_1 \lambda_2 \chi + \lambda_2^2 \chi^3 + \lambda_1 \sqrt{\lambda_2 (\lambda_1 + \lambda_2 \chi^2)} + (\sqrt{\lambda_2})^3 \chi^2 \sqrt{(\lambda_1 + \lambda_2 \chi^2)}}{\sqrt{\lambda_2} \sqrt{(\lambda_1 + \lambda_2 \chi^2)} [\sqrt{\lambda_2} \chi + \sqrt{(\lambda_1 + \lambda_2 \chi^2)}]} \quad (4.69)$$

Chapter 5

Modeling of Milling Forces

5.1. Introduction

The milling operation is an intermittent cutting process using a cutter with one or more teeth [25], therefore, it is a periodic process that is a function of spindle speed, number of teeth and pitch angles¹. In this chapter, the modeling of the milling forces for serrated cutters is discussed. To be more specific, the applied cutting force model, cutting force coefficient identification methods and cutting force model for serrated cutters are explained.

Cutting forces are calculated by a computer program which divides the cutter into thin disc-like elements for each flute. At every time increment, the chip load is calculated for each element by subtracting the workpiece surface from the tool, then the force on each element is determined. The total force on the cutter for that instant is found by integration of the forces along the cutter axis, i.e. for each element. Then cutter is rotated with an amount of differential angle which is determined by spindle speed and time increment, and the procedure given above is repeated until the desired number of revolutions are achieved. Note that, the positions of the cutter and workpiece are calculated for each time step and used for the calculation of the chip thickness which is not approximate but exact.

1. Pitch angle is the angle between successive teeth on the milling cutter

5.2. Mechanics of Milling

In milling, the workpiece, which is clamped to the table, is fed to the rotating tool, which is held in a spindle (see Figure 5.1.a). Due to simultaneous rotation and feed, the tool follows a trochoidal path [2].

The generated cutting forces are varying, and periodic either at each tooth or spindle period depending on the arrangement of the tooth spacing or the pitch angles. The tangential, radial and axial cutting forces appear in three orthogonal directions. Depending on the geometry of the cutter and the flute profile, the magnitude of the cutting forces varies. The force diagram of a general milling operation is shown in Figure 5.1.b. The variation of the chip thickness (h), which leads to varying force during cutting, can be also seen clearly in Figure 5.1. The varying chip thickness is the one of the most fundamental differences between turning and milling.

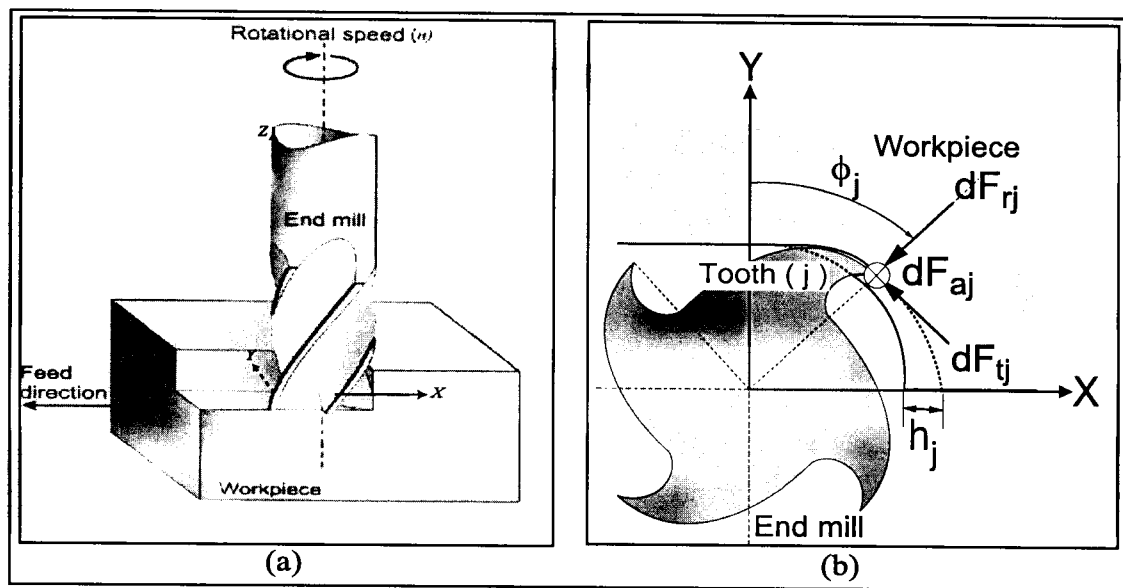


Figure 5.1 : (a) Milling Operation, (b) General Milling Force Diagram.

The elemental cutting forces in tangential, radial and axial directions contributed by one tooth are resolved into three cutting forces in orthogonal machine coordinates; X, Y and Z (see Eq. (5.1)):

$$\begin{aligned} dF_{xj}(\phi_j, z) &= -dF_{tj}(\phi_j, z)\cos\phi_j - dF_{rj}(\phi_j, z)\sin\phi_j \\ dF_{yj}(\phi_j, z) &= dF_{tj}(\phi_j, z)\sin\phi_j - dF_{rj}(\phi_j, z)\cos\phi_j \\ dF_{zj}(\phi_j, z) &= dF_{aj}(\phi_j, z) \end{aligned} \quad (5.1)$$

Note that the immersion angle for flute j (ϕ_j) is

$$\phi_j = \phi + j\phi_p - k_{i_0}z \quad (5.2)$$

and measured clockwise from positive Y axis, where $k_{i_0} = \frac{2\tan i_0}{D}$, i_0 is the helix angle, D is the diameter of the tool and z is the axial position of the point where the immersion angle is defined.

The total cutting force generated by one flute is computed by integrating the elemental forces along the in cut portion of this flute;

$$\begin{aligned}
F_{xj}(\phi_j) &= \int_{z_{j,1}(\phi)}^{z_{j,2}(\phi)} dF_{xj}(\phi_j, z) dz \\
F_{yj}(\phi_j) &= \int_{z_{j,1}(\phi)}^{z_{j,2}(\phi)} dF_{yj}(\phi_j, z) dz \\
F_{zj}(\phi_j) &= \int_{z_{j,1}(\phi)}^{z_{j,2}(\phi)} dF_{zj}(\phi_j, z) dz
\end{aligned} \tag{5.3}$$

where $z_{j,1}(\phi)$ and $z_{j,2}(\phi)$ are the lower and upper limits of the engagement of the flute j .

Finally, the total forces in X (feed), Y (normal) and Z (axial) directions can be found by contribution of all teeth,

$$\begin{aligned}
F_x &= \sum_{j=0}^{N-1} F_{xj}(\phi_j) \\
F_y &= \sum_{j=0}^{N-1} F_{yj}(\phi_j) \\
F_z &= \sum_{j=0}^{N-1} F_{zj}(\phi_j)
\end{aligned} \tag{5.4}$$

where N is the number of flutes on the cutter.

5.3. Linear-Edge Force Model

The linear edge force model was used by Armarego and Epp [12] in formulating the milling forces for zero helix cutters. This model uses linear force coefficients, and provides a reasonable physical interpretation of the cutting process. However, due to lack of acceptable model for the prediction of the edge forces, they need to be determined experimentally. Although edge forces are not independent of the chip thickness as suggested by this model, it is still acceptable in terms of first order approximation [38]. This model expresses the elemental tangential (dF_t), radial (dF_r), and axial (dF_a) cutting forces acting on flute j (Figure 5.1) as,

$$\begin{aligned} dF_{tj}(\phi_j, z) &= [K_{te} + K_{tc}h_j(\phi_j, z)]dz \\ dF_{rj}(\phi_j, z) &= [K_{re} + K_{rc}h_j(\phi_j, z)]dz \\ dF_{aj}(\phi_j, z) &= [K_{ae} + K_{ac}h_j(\phi_j, z)]dz \end{aligned} \quad (5.5)$$

where $h_j(\phi_j, z)$ is the uncut chip thickness; dz is the differential length in cutter axis; K_{tc} , K_{rc} , K_{ac} are cutting force coefficients due to the shear in the shear plane and K_{te} , K_{re} , K_{ae} are the edge cutting force coefficients due to the rubbing of the tool to the workpiece, in tangential, radial and axial directions, respectively. Note that dz is selected to be narrow enough to ignore any kind of variations like chip thickness along the element.

5.4. Cutting Force Coefficient Identification

There are three important parameters for the determination of the cutting coefficients, the shear stress (τ), the shear angle (ϕ_c) and the friction angle (β_a). These parameters can be determined from orthogonal cutting tests for different rake angles (α_n) and cutting velocities [39]. The

shear angle is an angle between the cutting speed (V) and the shear plane. The friction angle is defined on the rake face and the cutting edge is assumed to be sharp with no radius on it. These three parameters depend on both material and process and they are identified from the cutting experiments by using the orthogonal cutting model proposed by Merchant [39]. Orthogonal and oblique cutting geometries are shown in Figure 5.2.

During orthogonal cutting, two forces, namely feed/radial (F_r) and tangential (F_t) are generated. By using these forces, the shear stress, the shear angle and the friction angle can be obtained as,

$$\tau = \frac{F_t \cos \phi_c - F_r \sin \phi_c}{b \frac{h}{\sin \phi_c}} \quad (5.6)$$

$$\phi_c = \text{atan} \left(\frac{r_c \cos \alpha_r}{1 - r_c \sin \alpha_r} \right) \quad (5.7)$$

$$\beta_a = \alpha_r + \text{atan} \left(\frac{F_f}{F_t} \right) \quad (5.8)$$

where h is the uncut chip thickness, b is the width of cut, α_r is the rake angle and r_c is the chip ratio which is defined as a function of uncut chip thickness (h_c) and chip thickness (h) as,

$$r_c = \frac{h}{h_c} \quad (5.9)$$

5.5. Orthogonal to Oblique Cutting Transformation

The helical end milling is nothing but an oblique cutting, i.e. the cutting edge is no longer perpendicular to the cutting speed but it is inclined with amount of inclination angle (i) which is called helix angle for an end mill (see Figure 5.2).

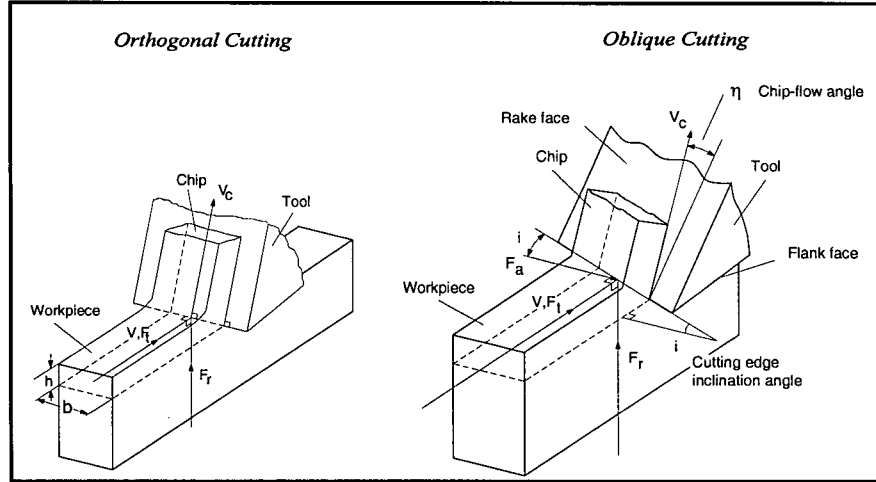


Figure 5.2 : Orthogonal and Oblique Cutting Geometry [25].

Armarego [40] expressed the cutting force coefficients for oblique cutting as follows,

$$\begin{aligned}
 K_{tc} &= \frac{\tau}{\sin \phi_n} \frac{\cos(\beta_n - \alpha_n) + \tan i \tan \eta \sin \beta_n}{\sqrt{\cos^2(\phi_n + \beta_n - \alpha_n) + \tan^2 \eta \sin^2 \beta_n}} \\
 K_{rc} &= \frac{\tau}{\sin \phi_n \cos i} \frac{\sin(\beta_n - \alpha_n)}{\sqrt{\cos^2(\phi_n + \beta_n - \alpha_n) + \tan^2 \eta \sin^2 \beta_n}} \\
 K_{ac} &= \frac{\tau}{\sin \phi_n} \frac{\cos(\beta_n - \alpha_n) \tan i - \tan \eta \sin \beta_n}{\sqrt{\cos^2(\phi_n + \beta_n - \alpha_n) + \tan^2 \eta \sin^2 \beta_n}}
 \end{aligned} \tag{5.10}$$

where

$$\begin{aligned}
\tan(\phi_n + \beta_n) &= \frac{\cos \alpha_n \tan i}{\tan \eta - \sin \alpha_n \tan i} \\
\tan \beta_n &= \tan \beta_a \cos \eta \\
\tan \phi_n &= \frac{r_c (\cos \eta / \cos i) \cos \alpha_n}{1 - r_c (\cos \eta / \cos i) \sin \alpha_n}
\end{aligned} \tag{5.11}$$

where ϕ_n is the normal shear angle in oblique cutting, α_n is the normal rake angle and η is the chip flow angle.

The following assumptions can be made for determining the cutting force coefficients for the oblique cutting process from orthogonal cutting database [18]:

$$\phi_n \equiv \phi_c, \quad \alpha_n \equiv \alpha_r, \quad \eta \equiv i \tag{5.12}$$

The last assumption in Eq. (5.12) is the adaption of Stabler chip flow rule [41] which is acceptable approximation for force prediction. Friction coefficient (β_a) and shear stress (τ) are same in both orthogonal and oblique cutting operations for same cutting conditions and material.

The edge cutting force coefficients in tangential and radial directions, i.e. K_{te} , K_{re} , are calculated from the orthogonal cutting data by simply finding the force axis intercept of the force-feed rate graph where feed rate is zero. In the verification part of this thesis, these edge cutting force coefficients are expressed as a function of rake angle and cutting speed in order to be more accurate, however, as it will be seen later, their dependencies on these parameters can easily be neglected. The edge cutting force coefficient in axial direction K_{ae} is taken as zero, which is known to be very small in oblique cutting [42].

5.6. Mechanics of Milling with Serrated Cutters

The mechanics of milling for serrated cutters is presented in this section. The direction conventions, force diagram and chip thickness for serrated cutters are shown in Figures 5.3.a and b, respectively. In Figure 5.3, a cylindrical cutter is used as a model for the sake of simplicity. However, this does not restrict the generalization of the solution, i.e., same formulation can be applied to any type of cutter. The only difference between serrated cutter and regular end mill, in terms of force diagram, is the effect of axial immersion angle (κ). For example, κ is always equal to 90 degrees for a cylindrical end mill, whereas it varies along the flute for a cylindrical serrated cutter.

Once again, the cutting forces in tangential, radial and axial directions, being contributed by one tooth, are resolved into cutting forces in machine coordinates; X, Y and Z:

$$\begin{aligned} dF_{xj}(\phi_j, z) &= -dF_{rj}(\phi_j, z) \sin \kappa \sin \phi - dF_{aj}(\phi_j, z) \cos \kappa \sin \phi - dF_{tj}(\phi_j, z) \cos \phi \\ dF_{yj}(\phi_j, z) &= -dF_{rj}(\phi_j, z) \sin \kappa \cos \phi - dF_{aj}(\phi_j, z) \cos \kappa \cos \phi + dF_{tj}(\phi_j, z) \sin \phi \\ dF_{zj}(\phi_j, z) &= dF_{rj}(\phi_j, z) \cos \kappa - dF_{aj}(\phi_j, z) \sin \kappa \end{aligned} \quad (5.13)$$

Finally the transformation matrix between tangential-radial-axial forces and X-Y-Z forces can be obtained as,

$$\begin{bmatrix} dF_{xj}(\phi_j) \\ dF_{yj}(\phi_j) \\ dF_{zj}(\phi_j) \end{bmatrix} = \begin{bmatrix} -\sin \kappa \sin \phi & -\cos \phi & -\cos \kappa \sin \phi \\ -\sin \kappa \cos \phi & \sin \phi & -\cos \kappa \cos \phi \\ \cos \kappa & 0 & -\sin \kappa \end{bmatrix} \begin{bmatrix} dF_{rj}(\phi_j) \\ dF_{tj}(\phi_j) \\ dF_{aj}(\phi_j) \end{bmatrix} \quad (5.14)$$

where

$$\begin{aligned}
 dF_{tj}(\phi_j, z) &= [K_{te} + K_{tc}h_j(\phi_j, \kappa, z)]db \\
 dF_{rj}(\phi_j, z) &= [K_{re} + K_{rc}h_j(\phi_j, \kappa, z)]db \\
 dF_{aj}(\phi_j, z) &= [K_{ae} + K_{ac}h_j(\phi_j, \kappa, z)]db
 \end{aligned}
 \tag{5.15}$$

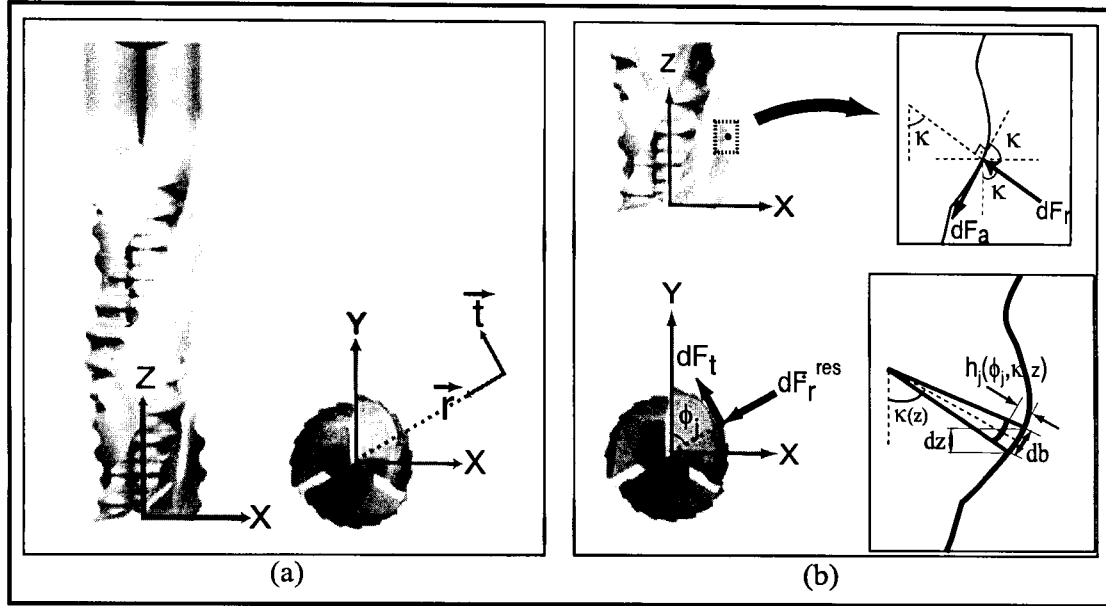


Figure 5.3 : (a) Direction Convention, (b) Force Diagram, Chip Thickness.

In Eq. (5.15), db is the projected length of an infinitesimal cutting flute in the direction along the cutting velocity. Note that, db is consistent with the chip width in classical oblique cutting, which is defined in Eq. (5.5). From, Figure 5.3, db can be defined as,

$$db = \frac{dz}{\sin \kappa} \tag{5.16}$$

5.7. Experimental Verification of Cutting Forces

Having determined the mathematical model of the cutter geometry and cutting forces, they were implemented in a simulation program where cutting forces can be calculated for different cutting conditions. In order to verify the outcomes of the program, cutting experiments were conducted under the same set of cutting conditions, i.e., feed rate, depth of cut and spindle speed. During experiments, the axial depth of cuts were selected in such a way that the chatter (self-excited) vibrations were prevented, therefore, static cutting force data were collected.

The cutting force coefficients were obtained by "Orthogonal to Oblique Cutting Transformation" technique presented before. The orthogonal tests were performed on Aluminium 7050-T7451 under different feed rates ranging from 0.025 mm/rev to 0.3 mm/rev and cutting speeds from 500 m/min to 1250 m/min on Hardinge Superslant CNC turning centre. In order to capture the effect of rake angle, tools with rake angles ranging from 0° to 16° were used. The measured orthogonal cutting force data were used to obtain the shear stress (τ), the shear angle (ϕ_c) and the friction angle (β_a) which were defined in Eqs. (5.6),(5.7),(5.8). Finally, by considering the effect of each parameter, orthogonal to oblique transformation model was obtained as:

$$\begin{aligned}\tau &= 297.0528 + 1.0474\alpha_r \\ \phi_c &= 24.2013 + 36.6678h + 0.0049V_c + 0.2995\alpha_r \\ \beta_a &= 18.7883 + 6.7008h - 0.0076V_c + 0.2581\alpha_r\end{aligned}\tag{5.17}$$




where h [mm] is the instantaneous chip thickness, V_c [$\frac{m}{min}$] is the cutting speed and α_r [rad] is the rake angle. The units for the rest is as follows; τ in [$\frac{N}{mm^2}$], ϕ_c in [$^\circ$], β_a in [$^\circ$].

And the edge cutting force coefficients [$\frac{N}{mm}$]:

$$\begin{aligned} K_{te} &= 23.4071 - 0.0014 V_c - 0.2555 \alpha_r \\ K_{re} &= 35.1607 - 0.0011 V_c - 0.5076 \alpha_r \\ K_{ae} &= 0.0 \end{aligned} \quad (5.18)$$

Several milling tests had been conducted by using three different type of cutters, the properties of those are given in Table 5.1. After mentioning the basic steps of the experimental verification, in the last part of this chapter, the comparison of real experimental data versus the simulated data will be presented. Sample test results and corresponding cutting conditions are given in Figures 5.4-5.6. (3 fluted cylindrical), Figure 5.7. (4 fluted cylindrical) and Figure 5.8. (4 fluted tapered ballend).

Table 5.1 : Cutters Used for Experimental Verification.

Cutter Type	Serration		No of flute	Profile	Figure No
	Height [mm]	Wave Length [mm]			
Cylindrical (Sandvik R216.33-20040-AC 38U-H10F)	0.289	3.66	3		5.4-6
Cylindrical (Sandvik R216.34-20040-BC 38K-I020)	0.296	1.94	4		5.7
Tapered Ballend (Pratt&Whitney, Canada)	0.564	2.12	4		5.8

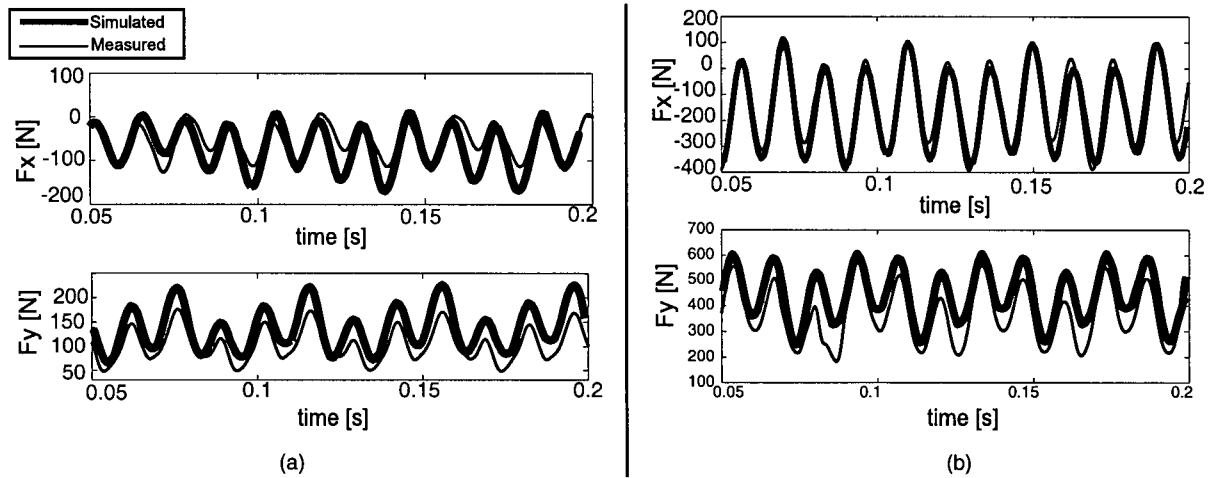


Figure 5.4 : Full Immersion at 1500 rpm, (a) 7 mm Axial Depth of Cut, 0.02 mm/tooth.rev Feed Rate; (b) 8 mm Axial Depth of Cut, 0.08 mm/tooth.rev Feed Rate.

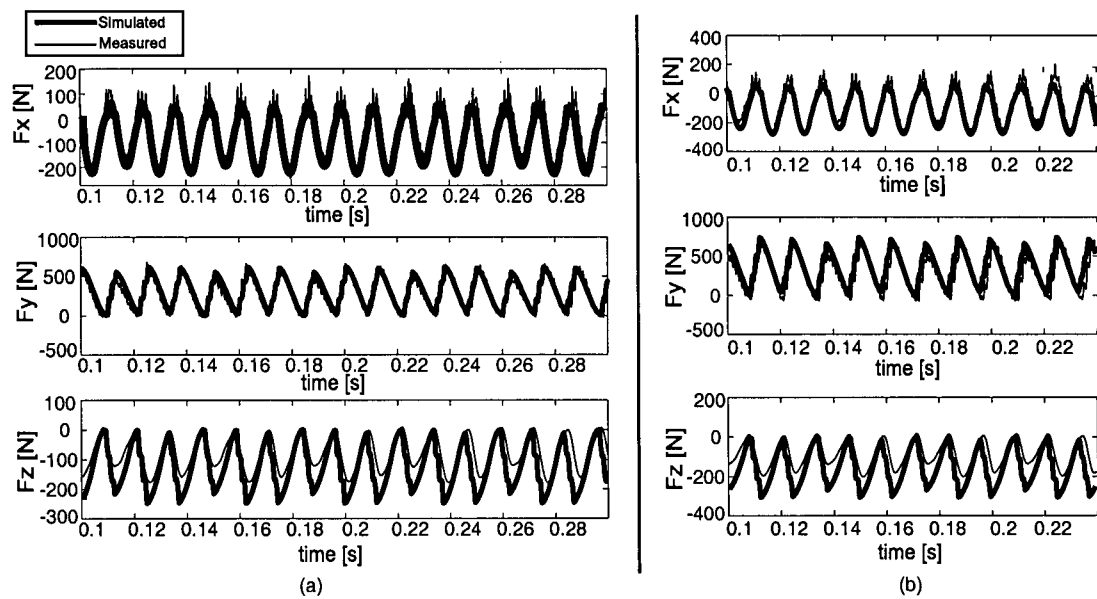


Figure 5.5 : Half Immersion Down Milling at 1600 rpm, 8 mm Axial Depth of Cut (a) 0.08 mm/tooth.rev Feed Rate; (b) 0.10 mm/tooth.rev Feed Rate

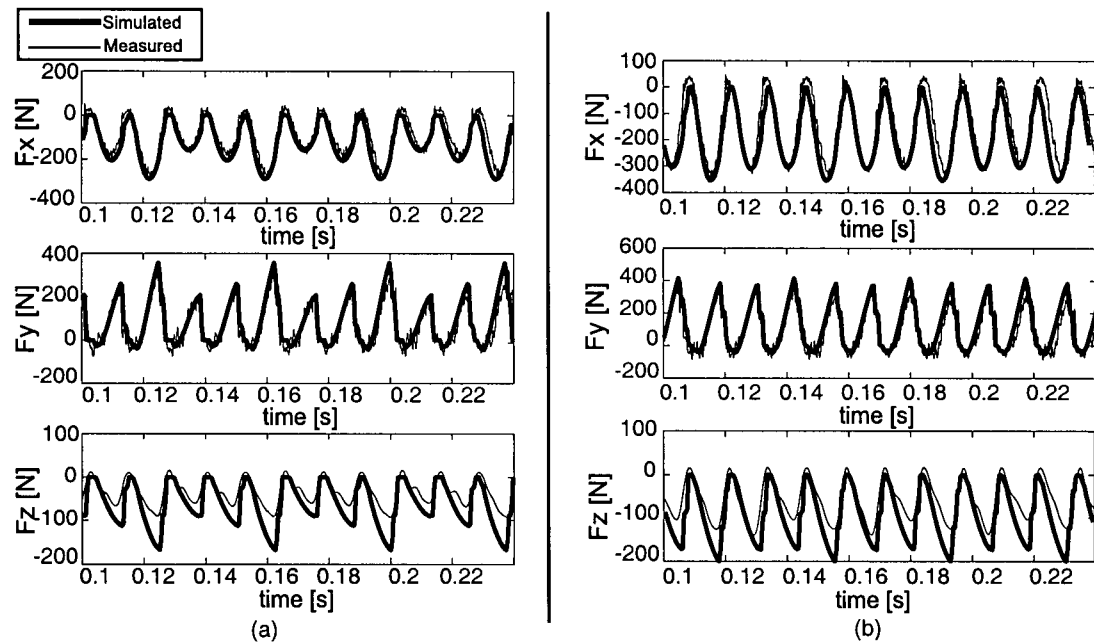


Figure 5.6 : Half Immersion Down Milling at 1600 rpm, 0.08 mm/tooth.rev Feed Rate
(a) 4 mm Axial Depth of Cut; (b) 6 mm Axial Depth of Cut.

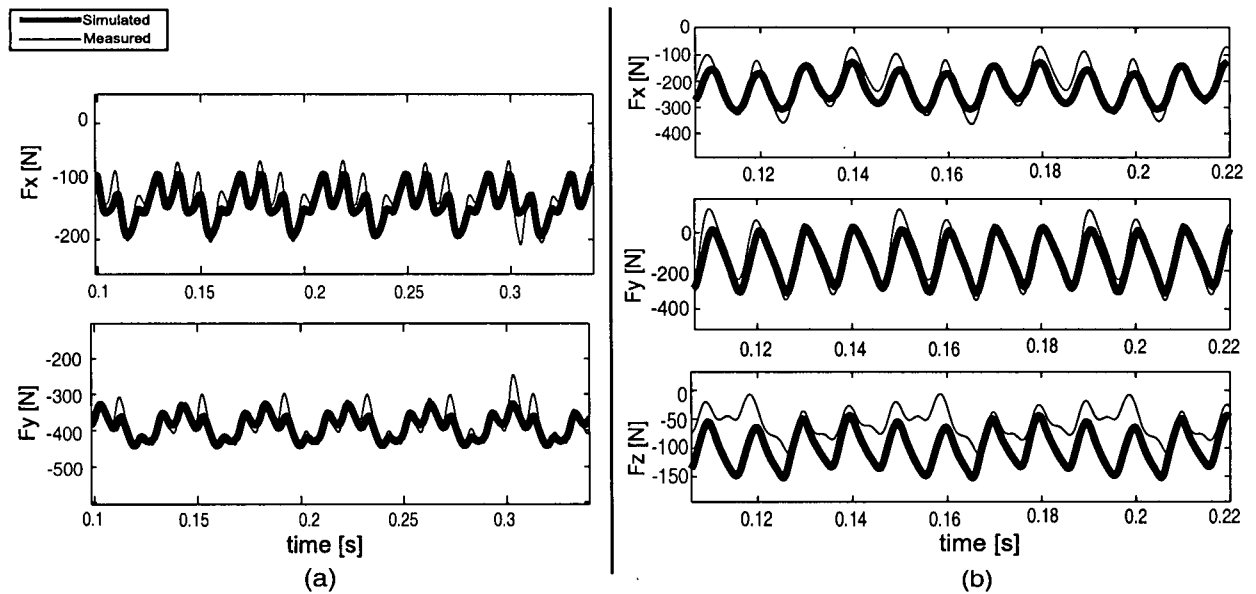


Figure 5.7 : Full Immersion at 1500 rpm, (a) 7 mm Axial Depth of Cut, 0.02 mm/tooth.rev Feed Rate; (b) 8 mm Axial Depth of Cut, 0.08 mm/tooth.rev Feed Rate.

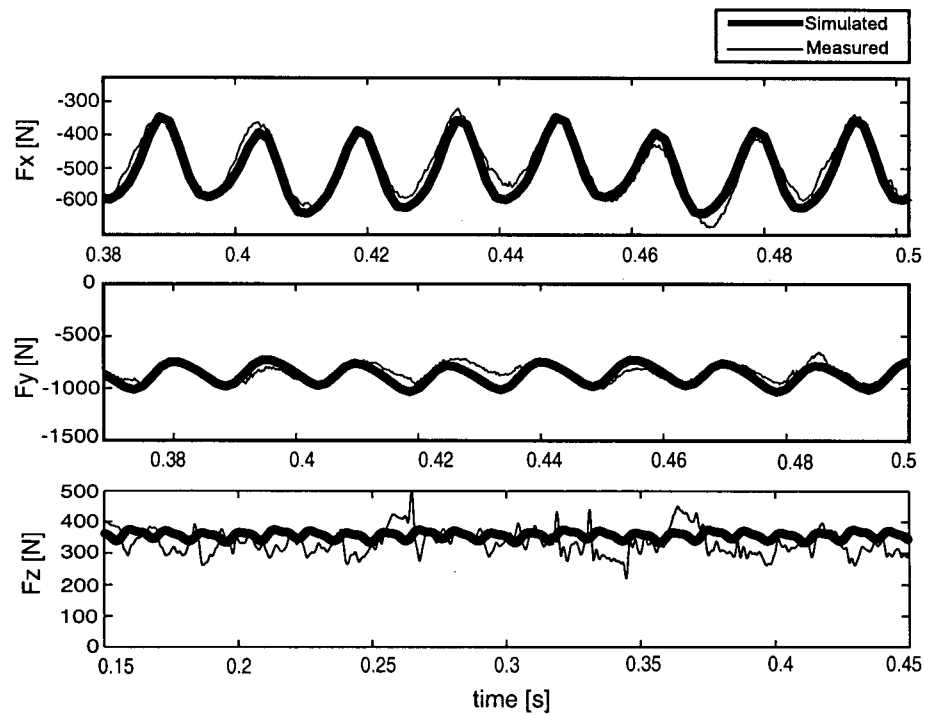


Figure 5.8 : Full Immersion, 15 mm Depth of Cut, 0.04 mm/tooth.rev at 1000 rpm.

As stated before, serrated cutters are used to reduce cutting forces during roughing operations. The Figure 5.9 shows the simulated cutting forces obtained by regular and serrated cutter. The reduction in the cutting forces are obvious.

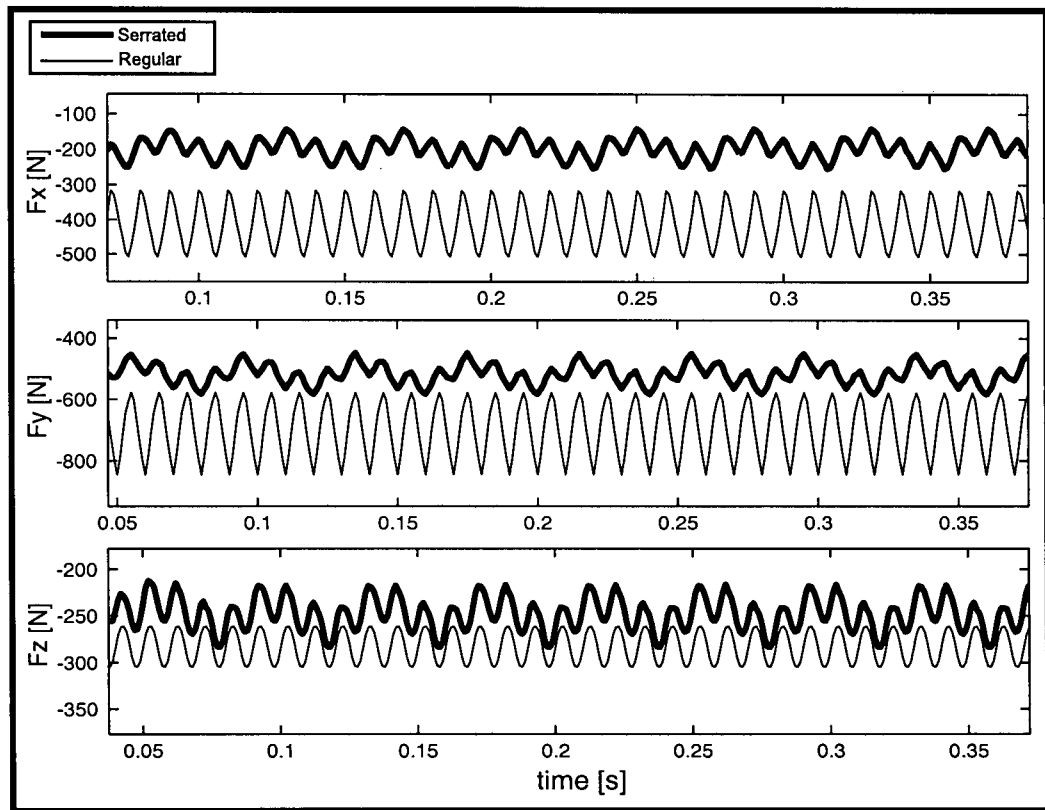


Figure 5.9 : Simulated Cutting Forces: 4 fluted Cylindrical Helical Endmill, 1500 rpm, 0.05 mm/tooth.rev, 10 mm Depth of Cut.

5.8. Chatter Stability

The driving force behind the design of special cutters like serrated end mills is to attain higher depth of cuts without disturbing the stability of the system which may lead to unstable chatter vibrations. Chatter vibrations are one of the biggest problems encountered during metal cutting operations. Two main causes of chatter are defined as mode coupling and regeneration of waviness. When the relative vibration between the workpiece and the tool exists simultaneously in at least two directions in the plane of orthogonal cutting, mode coupling occurs. However,

Tlusty [47] shows that the system's stability against mode coupling is higher and the dominant mode of chatter results from regeneration mechanism. Regeneration of waviness occurs due to waviness of the surface generated by a vibrating tooth, which is going to be removed by a successive tooth. Since the chip thickness is defined by the width of the removed material and the cutting forces are directly proportional to it, depending on the waves on either side of the chip, the cutting forces may grow and lead to unstable vibrations called chatter vibrations. Figure 5.10 shows the static and dynamic chips for milling.

A special condition occurs when the vibration marks on either side of the chip are in phase (see Figure 5.10). In this case, the chip thickness still remains constant, and the system goes under forced vibrations which do not grow indefinitely.

An accurate calculation of dynamic chip thickness along the cutter is necessary for the determination of chatter stability in time domain. The judgement of the chatter is done by comparing the dynamic chip load with the intended chip load, i.e. static chip thickness at that particular radial location of the cutter. If the ratio of these two parameters exceeds a pre-specified value, the system is decided to be under unstable vibrations, i.e., chatter vibrations. The flow chart of this computation is given in Figure 5.11.

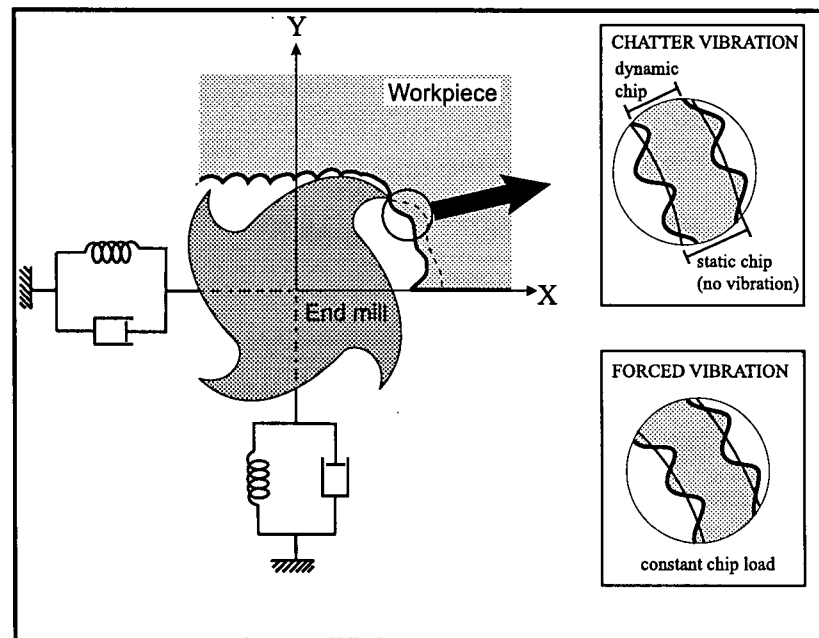


Figure 5.10 : Static and Dynamic Chip.

In time domain, the stability lobe diagram (spindle speed versus axial depth of cut) is obtained by following the steps presented below:

- (*) Cutting tool geometry, feedrate, machine/workpiece dynamics, starting depth of cut (a), cutter orientation and immersion, workpiece material and cutting coefficients are specified.
- (*) Spindle speed range (start & end values) as well as step size are specified. Some parameters such as maximum and minimum axial depth of cuts are initialized.
- (*) The cutter and workpiece are divided into differential axial elements, and the locations of these elements are stored in two separate arrays (cutter, workpiece). These arrays are updated at each time step during the simulation (see Figure 5.12). Length of an each element needs to be small enough to capture the effect of serrations on the process. In this thesis, this length is determined by a proper

conversion (as explained in Geometric Modeling chapter) ensuring that one repetitive section of the serration is divided into ten portions.

- (*) For a given spindle speed, a static time domain simulation is run. At steady state, the maximum static uncut chip thickness, $h_{\text{static,max}}$, is determined by scanning axial elements on each flute and finding the maximum displacement of the serration into workpiece. Since the dynamics are not considered, the effect of forces on the deflection of the machine/workpiece is ignored. Therefore, this part of the simulation does not take long computation time.
- (*) Including the dynamics of the structures (machine/workpiece), another time domain simulation is run until a steady-state chatter condition is reached. Cutting forces determined at each time step are used to calculate dynamic response of the structure from a dynamic model in state space using Runge-Kutta 4th order iteration. This procedure is well explained in [13]. Once again, each flute is scanned along the axis of the cutter and the largest dynamic chip thickness, $h_{\text{dynamic,max}}$, is found.
- (*) The chatter parameter, ρ , is evaluated as $\rho = \frac{h_{\text{dynamic,max}}}{h_{\text{static,max}}}$
- (*) If ρ is found to be bigger than a limiting value, ρ_{limit} , the chatter vibration occurs, otherwise, the system is stable. ρ_{limit} is a user defined parameter and taken as 1.2 for the time domain simulations in this thesis.
- (*) If the process is stable, a_{min} is set to value of a , and steps above are followed by doubling a . Otherwise, a_{max} is set to the value of a , and a is halved before the simulation is run again.
- (*) Simulation is run until desired resolution is obtained, i.e., $(a_{\text{max}} - a_{\text{min}}) < a_{\text{tol}}$

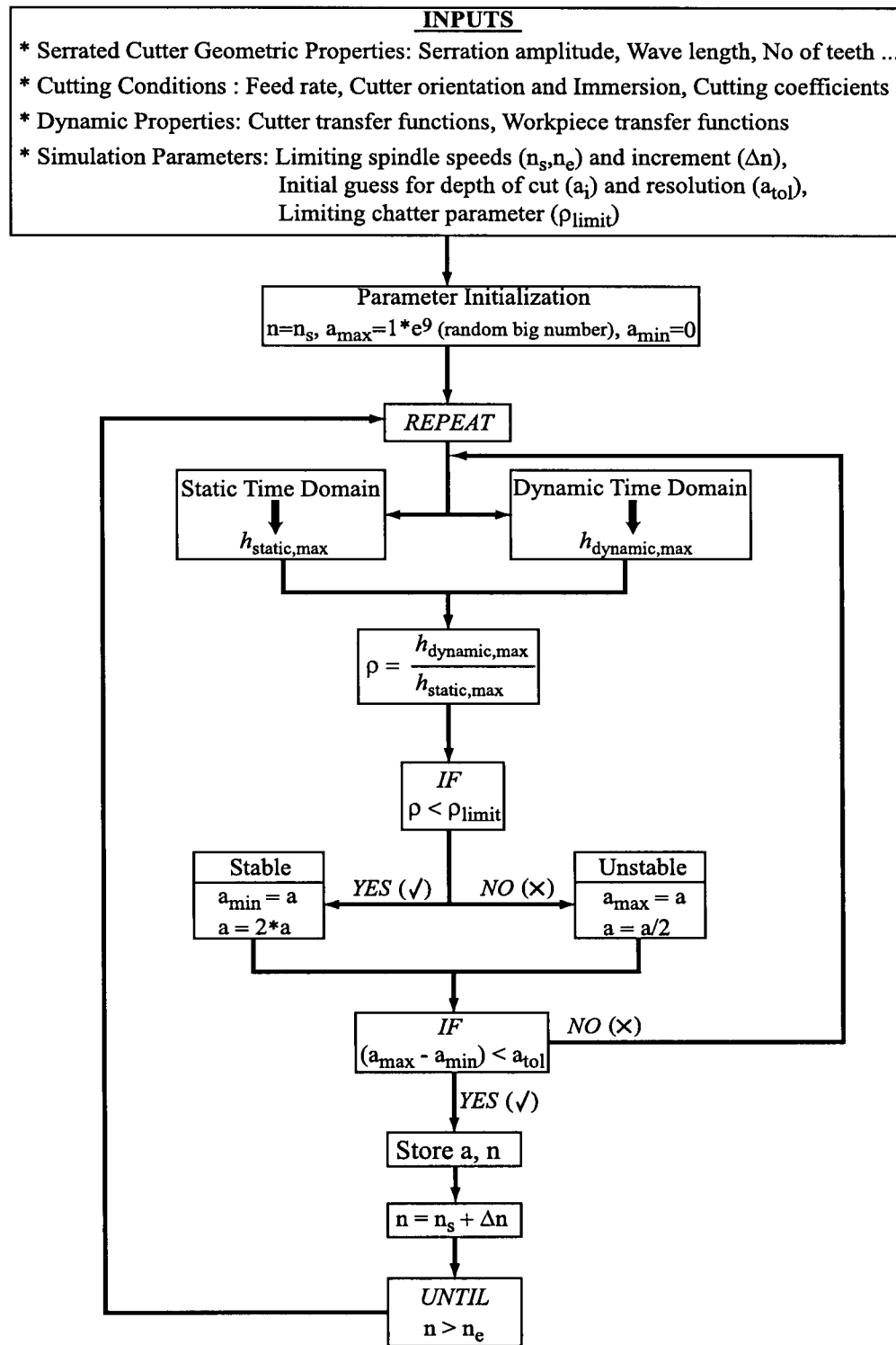


Figure 5.11 : Flow Chart of Time Domain Simulation.

There are important remarks to be made for the time domain simulation. First of all, computation time is long because the exact kinematics and dynamics of the cutter and workpiece are considered. Second, the transient region before the simulation reaches a steady state must be ignored and should not be used in the calculation of chip thickness (neither dynamic nor static). Finally, the nonlinearities involved in the process like tool jumping out of the cut can be modelled with this kind of time domain simulation.

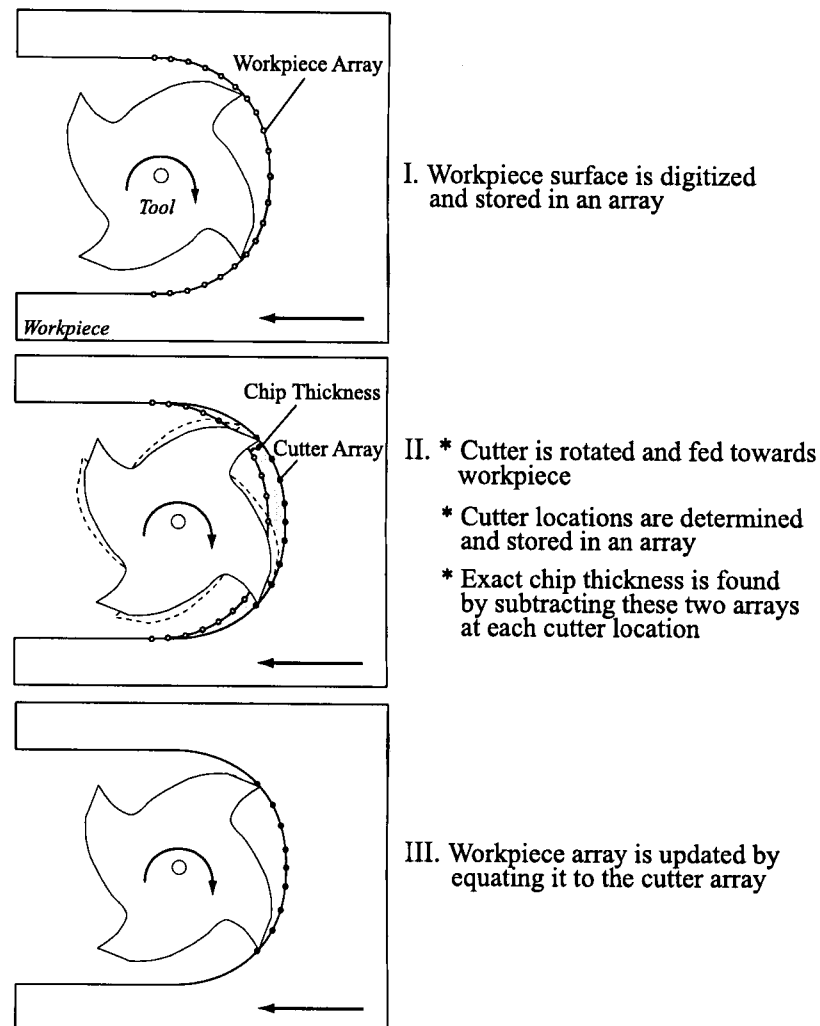


Figure 5.12 : Exact Chip Thickness Determination in Time Domain Simulation.

5.9. Experimental Verification of Chatter Stability

The proposed model has been tested to simulate chatter vibration stability lobes in time domain. Dynamic characteristics of the structure is determined by measuring the transfer function. In reality, the spindle is a continuous beam with infinite number of elements connected to each other with infinite number of springs and dampers. In order to make the analysis possible, this structure is approximated with a discrete beam as shown in Figure 5.13. In this model, spindle dynamics are lumped at (r) nodes.

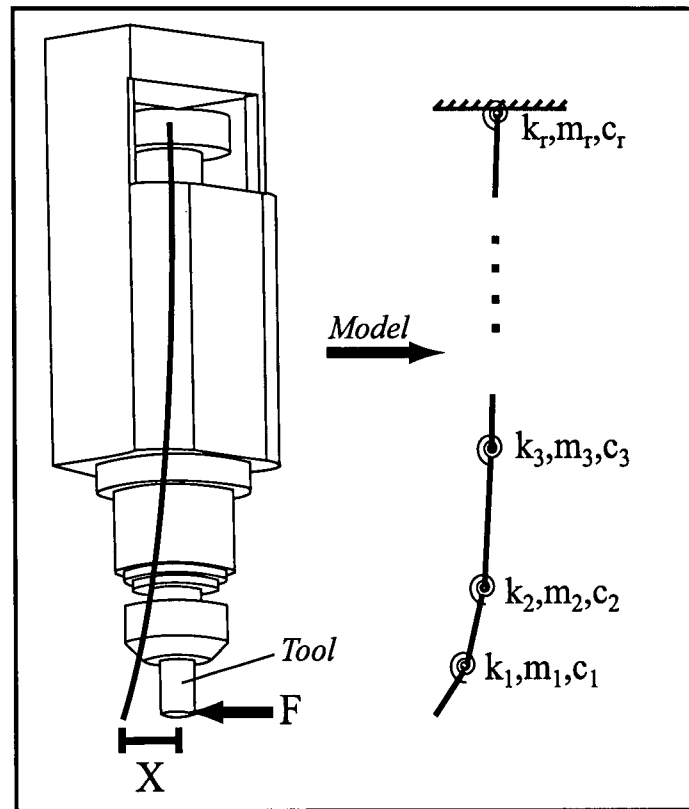


Figure 5.13 : Spindle Model.

During cutting, only tool is contact with the workpiece, therefore, the transfer function at the tool tip is enough for the simulation. In frequency domain, the transfer function (G) at the tool tip for (r) number of modes is found by superimposing the effect of each mode at the point of interest:

$$G(i\omega) = \frac{X}{F}(i\omega) = \sum_{j=1}^r \frac{\omega_{nj}^2/k_j}{(\omega_{nj}^2 - \omega^2) + i2\xi_j\omega_{nj}c_j} \quad (5.19)$$

where $\omega_{nj} = \sqrt{k_j/m_j}$ is the natural frequency of mode j , $\xi_j = c_j/(2\sqrt{k_jm_j})$ is the damping ratio and m_j , k_j , c_j are modal mass, stiffness and damping constant, respectively.

The transfer function of the cutter used during the experiments was measured while it was in the spindle. By using an in-house developed transfer function measurement software, Frequency Response Functions (FRFs) were determined from a force pulse generated by the impact of an instrumented hammer (Kistler 9722A2000) and the response signal measured with an accelerometer (PCB 353B11) stuck on the cutting tool tip. The measured FRFs were then approximated with a curve fit to obtain the dynamic parameters of the structure in both X and Y directions, which are presented in Table 5.2. Magnitudes of both measured and fitted transfer functions can be seen in Figure 5.14.

Table 5.2 : Dynamic Parameters in X and Y Directions.

<i>X Direction</i>			<i>Y Direction</i>		
ω_n [Hz]	ζ [%]	k [N/m]	ω_n [Hz]	ζ [%]	k [N/m]
480	1.52	1.21e+8	470	2.81	8.38e+8
530	2.8	3.02e+8	533	2.67	1.41e+8
893	3.03	1.22e+8	884	2.41	9.85e+7
1216	3.33	2.56e+7	1155	1.61	1.32e+8
1433	4.11	9.48e+7	1270	2.80	5.89e+7
2085	2.94	5.62e+7	1946	2.44	3.89e+7
2691	2.65	9.71e+7	2670	1.89	1.09e+8

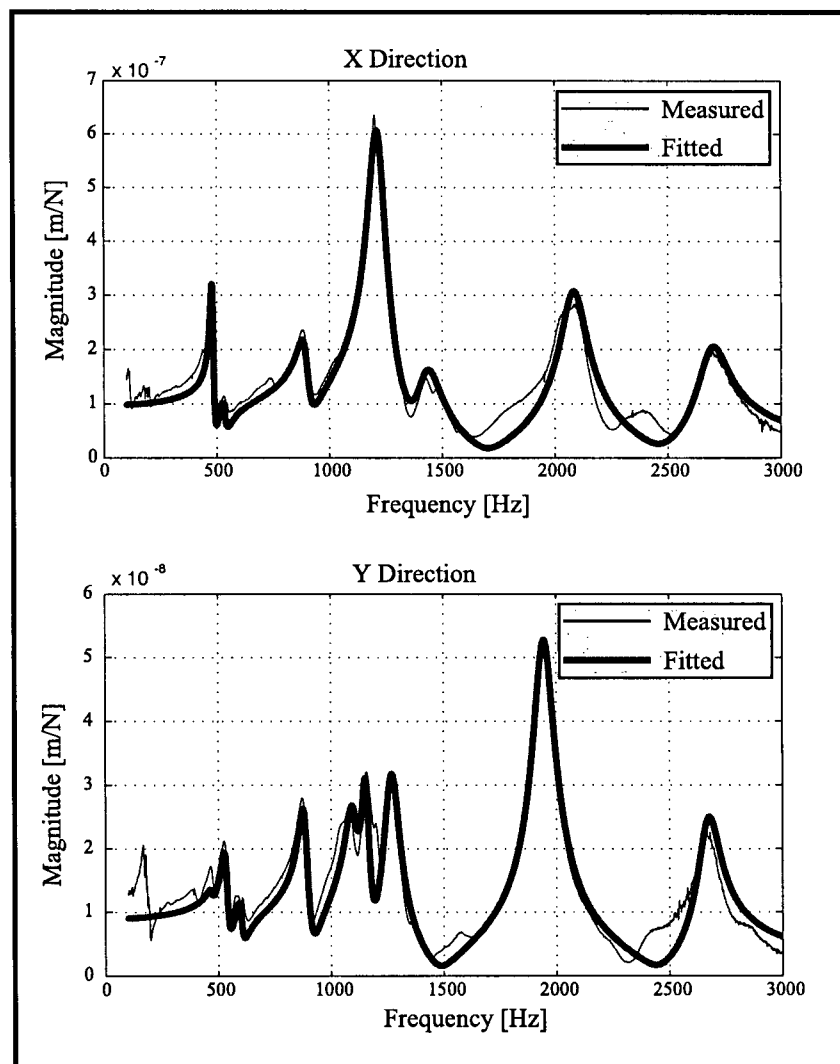


Figure 5.14 : Transfer Functions Obtained at the Tool Tip.

Comparison of stability lobes with and without serrated cutting edges are given in Figure 5.15. It can be seen that the serrated cutter increased the absolute chatter stability limit from 2 mm to 9 mm, which corresponds to 450% increased in the productivity rate, for the particular spindle and tool/holder structure given here. During experiments, at each cutting point, the cutting forces and sound pressure were measured and their Fast Fourier Transforms (FFTs) were investigated. Examples of a chatter (operating point A) and a non-chatter (operating point B) conditions are presented in Figure 5.16. The judgement of chatter was made by checking whether the spectrum had higher amplitude at the modal frequency in comparison to tooth passing frequency, as well as the surface finish. Although serrations left counter profile on the surface generated, the vibration marks were still distinguishable.

Since the chatter stability is linearly decreased with the axial depth of cut, and considered to be independent of chip thickness, the chatter vibration free depth of cuts are increased with the serrated cutters. The reason behind this can be explained by apparent depth of cut phenomenon (the apparent instantaneous cutting edge contact), which is illustrated in Figure 5.17. The waves represent the serrations on flutes, for simplicity, the flutes are selected to be straight, i.e. helix angle is zero. Since there is a phase shift between consecutive flutes, each of them remove different portions from the workpiece along the axial depth of cut as they are fed towards the workpiece by an amount of feed rate (c). At steady state, the length of the intersection of the flute with the workpiece along the cutter axis, which is " $a_1 + a_2$ ", becomes less than the actual depth of cut, " a ". This dimension is named as apparent depth of cut. It is obvious that the decrease in the depth of cut with a serrated cutter is compensated with the feed rate which varies along the flute and

ends up to be more than intended feed rate (c) at some points and zero at others (points where flute does not even touch the workpiece).

Another reason for an increased stability is the disturbance of the regenerative phase shift. Serration profiles have phase shift from one flute to next. This leads to varying pitch angle between two successive teeth that disturbs the regenerative phase shift at each tooth period and prevents the build up of chatter vibration energy in the system.

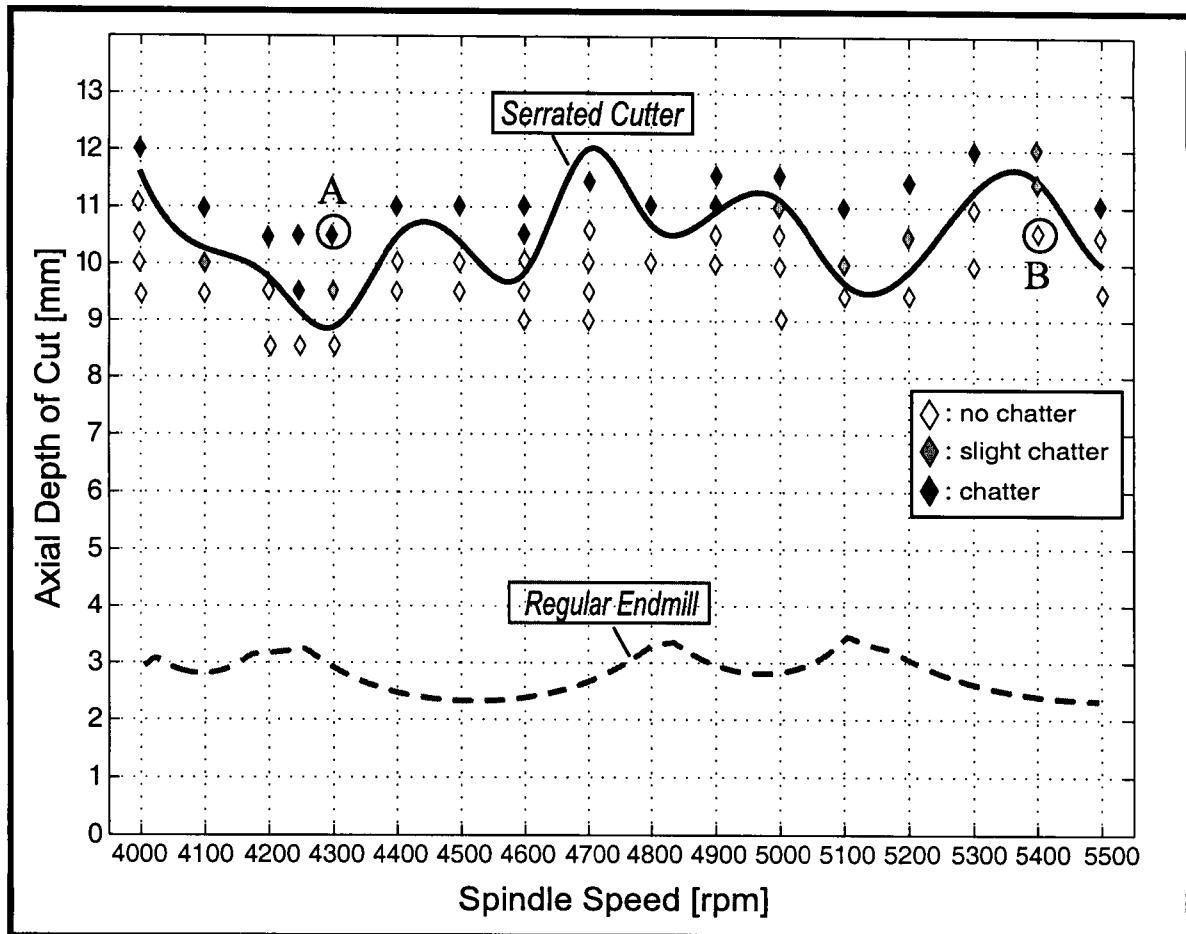


Figure 5.15 : Measured and Simulated Stability Lobes for 3 fluted Cylindrical Serrated Endmill, $c=0.04$ mm/rev.tooth, Material: Al 7050, Experimental Results.

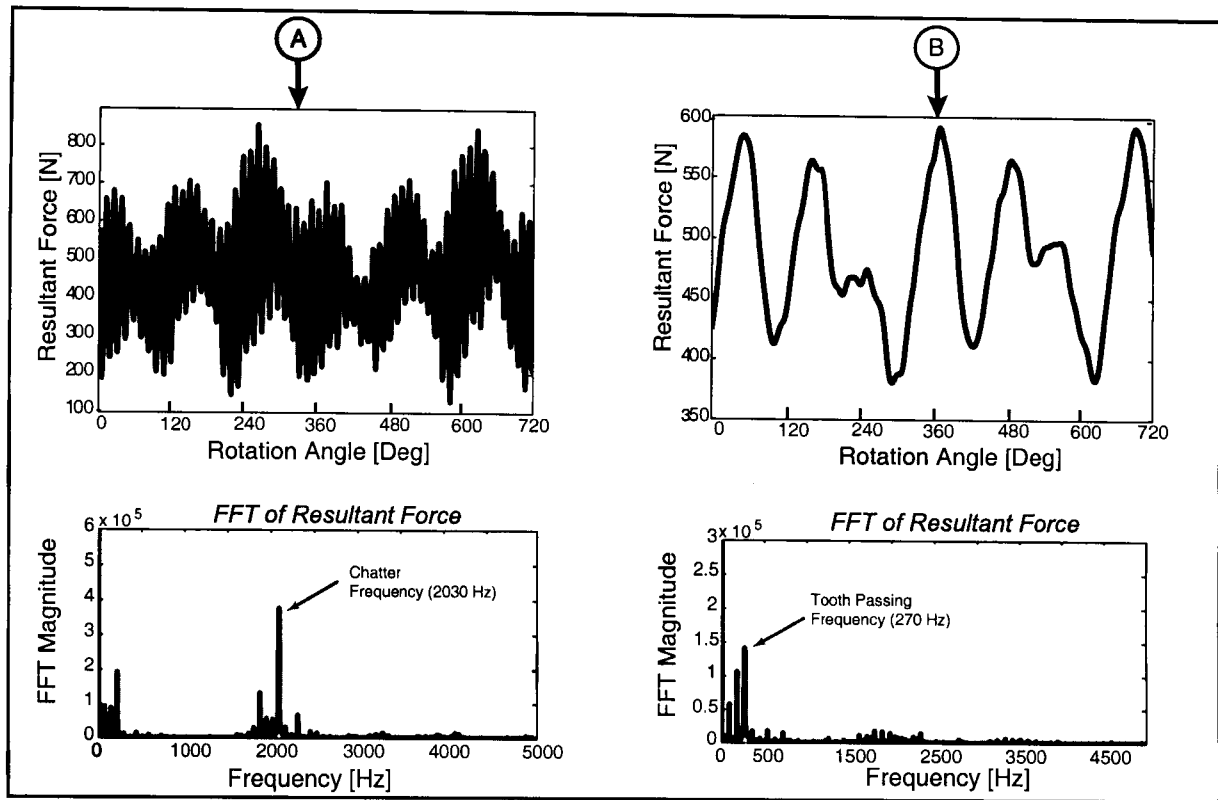


Figure 5.16 : Experimental Results: Force and FFT at 4300 (A) and 5400 rpm (B), $a=10.5$ mm.

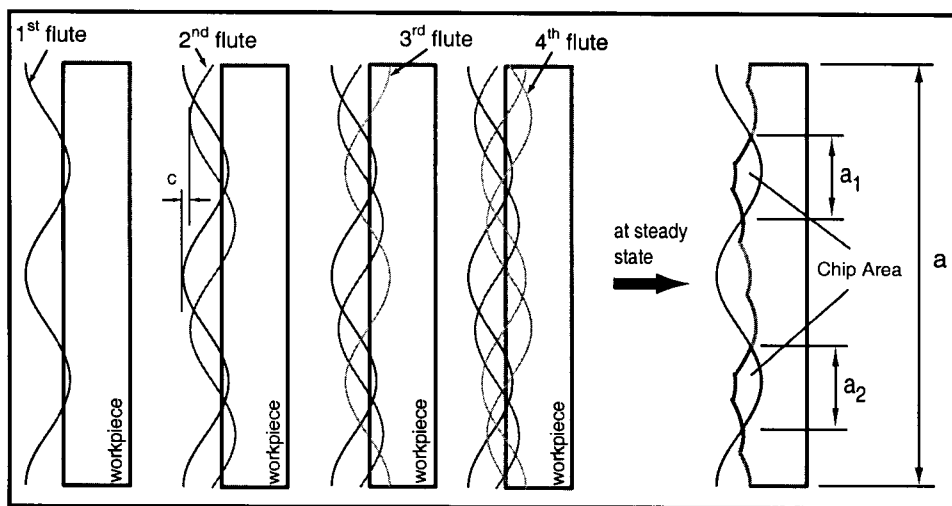


Figure 5.17 : Effect of Serrations on Depth of Cut.

Conclusion

The mechanics and dynamics of rough and finish milling operations are studied in this thesis.

The primary source of chatter is due to regeneration in chip thickness. When the waves generated on the upper and lower surfaces of the chip are out of phase with more than 180 degrees, the system becomes unstable and chatter vibrations grow until either tool breaks or jumps out of cut due to saturation of the displacement range. The waves can be forced to being close to in-phase by matching the tooth passing and chatter frequencies, which are possible only at high spindle speeds used in finish milling. Specially designed tools, such as serrated or variable pitch cutters, can prevent the phase being locked into an unstable value, i.e. 180 degrees or higher. This thesis presents modeling of low speed milling with serrated cutters, and high speed milling with small radial immersions.

The serrations or waves on the flutes are modeled mathematically by fitting the profile with a cubic spline. The coordinates and curvature of the splined edge at each point along the flute are mathematically modeled, and integrated to the previously developed dynamic, time domain milling simulation program. The chip thickness at each point is calculated along the vector normal to the cutting edge while considering rotation of the spindle, linear feed motion of the part and vibrations of both cutter and work-piece structures. The differential cutting force acting at each point along the cutting edge is evaluated by using orthogonal to oblique cutting transformation mechanics. The differential forces are integrated to identify the total cutting force acting in three Cartesian Coordinates of the machine, and applied on the structural, lumped dynamic model of the

machine. The simulation is continued in discrete time domain for few spindle revolutions, and the cutting forces, torque, power, vibrations and surface form errors are predicted. The time domain simulations are compared against experimentally measured forces and chatter vibrations. It is shown that when the serrated cutter with waves can increase the chatter stability by removing up to 2-4 times deeper cut than the regular end mills. The degree of stability is determined by the wave geometry, feed rate as well as the structural dynamics of the tool.

When the radial immersion is low, the periodic cutting force waves have short duration with sharp rise or drop, creating significant number of harmonics in frequency domain. Recent publications ([44], [46]) claim that the chatter stability solution previously developed by Budak and Altintas [31] at UBC would not be able to predict added stability lobes, but their methods could. The thesis shows that when the harmonics are added to the chatter frequency, and the corresponding Frequency Response Functions are considered in the directional coefficient matrix, the added stability lobes can also be predicted by the frequency domain chatter stability theory of Budak & Altintas [31]. The mathematical proof and its verification using the exact time domain solution are presented. Furthermore, the physics behind the added stability lobes at integer multiples of half tooth passing frequencies are explained, proven mathematically and in time domain simulations. The model's accuracy is also verified by comparing the predictions against specially designed experiments presented by the same researchers who presented alternative methods ([44], [46]).

Future Research Directions

The chatter stability of milling has significant room for further study. The optimal spacing and selection of serration waves would be challenging, especially if it can be modeled in frequency domain analytically. In multi frequency case, the thesis considered only one mode in one direction. The real industrial applications have multiple modes at least in two directions. Furthermore, the structural dynamics of the thin web and long end mill may vary along the spindle axis, creating a complex stability problem for frequency domain solutions.

Bibliography

- [1] Budak E., 1994, *Mechanics and Dynamics of Milling Thin Walled Structures*, University of British Columbia, Ph.D. Thesis.
- [2] Martellotti M.E., 1941, *An Analysis of the Milling Process*, Transactions of ASME, pp. 677-700.
- [3] Martellotti M.E., 1945, *An Analysis of the Milling Process Part II: Down Milling*, Transactions of ASME, Vol.67, pp. 233-251.
- [4] Airey J., Oxford C.J., 1921, *On the Art of Milling*, Transactions of ASME, Vol.43, pp.549.
- [5] Parsons F., 1923, *Power Required for Cutting Metal*, Transactions of ASME, Vol.49, pp.193-227.
- [6] Sawin N.N., 1926, *Theory of Milling Cutters*, Mechanical Engineering, Vol.48, pp.1203-1209.
- [7] Salomon C., 1926, *Die Frasarheit*, Werkstttstechnik, Vol.20, pp.469-474.
- [8] Boston O.W., Kraus C.E., 1932, *Elements of Milling*, Transactions of ASME, Vol.54, pp.74-104.
- [9] Boston O.W., Kraus C.E., 1932, *Elements of Milling-Part ii*, Transactions of ASME, Vol.56, pp.355-371.
- [10] Montgomery D., 1991, Altintas Y., *Mechanism of Cutting Force and Surface Generation in Dynamic Milling*, Transactions of ASME Journal of Engineering for Industry, Vol.113, pp.160-168.
- [11] Lee P., 1995, *Mechanics and Dynamics of Ball End Milling*, Master's Thesis, University of British Columbia.
- [12] Armarego, E.J.A., Epp, C.J., 1970, *An Investigation of Zero Helix Peripheral Up-Milling*, International Journal of Machine Tool Design and Research, Vol. 10, pp.273-291
- [13] Campomanes M.L., 1998, *Dynamics of Milling Flexible Structures*, Master's Thesis, University of British Columbia.
- [14] Sutherland J.W., DeVor R.E., 1986, *An Improved Method for Cutting Force and Surface Prediction in Flexible End Milling System*, Transactions of ASME Journal of Engineering for Industry, Vol.108, pp.269-279.

- [15] Tlusty J., Ismail F., 1981, *Basic Nonlinearity in Machining Chatter*, Annals of the CIRP, Vol. 30, pp. 21-25.
- [16] Kline W.A., DeVor R.E., Zdeblick W.J., 1980, *A Mechanistic Model for the Force System in End Milling with Application to Machining Airframe Structures*, In North American Manufacturing Research Conference Proceedings Society of Manufacturing Engineers, Vol. 18, pp.297, Dearborn, MI.
- [17] Altintas Y., Spence A., *End Milling Force Algorithms For Cad Systems*, Annals of CIRP, Vol.50(1), pp.169-175
- [18] Budak E., Altintas Y., Armarego E.J.A., 1996, *Prediction of Milling Force Coefficients from Orthogonal Cutting Data*, Transactions of ASME, Vol.118, pp. 216-224.
- [19] Armarego E.J.A., Brown R.H., 1969, *The Machining of Metals*, PreticeHall.
- [20] Tlusty J., McNeil P., 1970, *Dynamics of Cutting Forces in End Milling*, Annals of the CIRP, Vol.24, pp.21-25.
- [21] Ehmann K.F., Kapoor S.G., DeVor R.E., Lazoglu I., 1997, *Machining Process Modelling: A Review*, ASME J. Manuf. Sci. Eng., Vol.119, pp. 655-663.
- [22] Tlusty J., Ismail F., Zaton W., 1982, *Milling Cutters with Irregular Pitch*, Technical Report, Mc Master Engineering.
- [23] Campomanes M.L., 2002, *Kinematics and Dynamics of Milling with Roughing Endmills*, Metal Cutting and High Speed Machining, Kluwer Academic/Plenum Publishers.
- [24] Merdol S.D., Altintas Y., 2002, *Mechanics and Dynamics of Serrated Cutters*, ASME IMECE, (in print)
- [25] Altintas Y., 2000, *Manufacturing Automation*, Cambridge University Press.
- [26] Engin S., Altintas Y., 2001, *Mechanics and Dynamics of General Milling Cutters Part I: Helical End Mills*, International Journal of Machine Tools and Manufacture, Vol.41, pp.2195-2212.
- [27] Tlusty J., 1965, *A Method of Analysis of Machine Tool Stability*, Proceeding MTDR, pp.5-14.
- [28] Tobias S.A., 1965, *Machine Tool Vibration*, Blackie and Sons Ltd.
- [29] Merritt H.E., 1965, *Theory of Self-Excited Machine Tool Chatter*, ASME Journal of Engineering for Industry, Vol. 87, pp.447-454.
- [30] Minis I., Yanushevsky T., 1993, *A New Theoretical Approach for the Prediction of Machine Tool Chatter in Milling*, ASME Journal of Engineering for Industry, Vol. 115, pp.1-8.

- [31] Budak E., Altintas Y., 1995, *Analytical Prediction of Stability Lobes in Milling*, CIRP Annals, Vol. 44, No.1, pp.357-362.
- [32] Hutton G. S., Tian J., 2001, *Chatter Instability in Milling Systems with Flexible Rotating Spindles-A New Theoretical Approach*, Jrn of Manufacturing Science and Eng., Vol. 123.
- [33] Onwubiko C, 1989, *Foundations of Computer-Aided Design*, West Publishing, MN, pp135.
- [34] Ramaraj, T.C., Eleftheriou, E., 1994, *Analysis of the Mechanics of Machining with Tapered End Milling Cutters*, Transactions of the ASME, Vol.116, pp. 398-404.
- [35] Lee, P.P.W., 1995, *Mechanics and Dynamics of Ballend Milling*, Master of Applied Science Thesis.
- [36] Zeid, I., 1991, *CAD/CAM Theory and Practice*, McGraw-Hill.
- [37] Engin, S., 1999, *Mechanics and Dynamics of Milling with Generalized Geometry*, Doctor of Philosophy Thesis.
- [38] Brown R.H., Armarego E.J.A., 1964, *Oblique Machining with a Single Cutting Edge*, International Journal of Machine Tool design and Research, Vol.4, pp. 9-25.
- [39] Merchant, M.E., 1944, *Basic Mechanics of the Metal Cutting Process*, Transactions of ASME Journal of Applied Mechanics, pp. 168-175.
- [40] Armarego E.J.A., 1993, *Material Removal Process : An Intermediate Course*, The University of Melbourne, pp. 48-49.
- [41] Stabler G.V., 1964, *The Chip Flow Law and Its Consequences*, Advances in Machine Tool Design and Research, pp. 243-251.
- [42] Armarego E.J.A., Whitfield R.C., 1985, *Computer Based Modelling of Popular Machining Operations for Force and Power Predictions*, Annals of the CIRP, Vol. 34, pp. 65-69.
- [43] Altintas Y., Engin S., Budak E., 1999, *Analytical Stability Prediction and Design of Variable Pitch Cutters*, Journal of Manufacturing Science and Engineering, Vol. 121, pp. 173-178.
- [44] Insperger T., Stepan G., Bayly P. V., Mann B. P., *Multiple Chatter Frequencies in Milling Processes*, Journal of Sound and Vibration, accepted, to appear in (2002).
- [45] Tlusty J., 2000, *Manufacturing Processes and Equipment*, Prentice Hall.
- [46] Davies M.A., Pratt J.R., Dutterer B., Burns T.J., *Stability Prediction for Low Radial Immersion Milling*, 2000, Annals of the CIRP, Vol.49., p.41.
- [47] Koenigsberger F., Tlusty J., 1967, *Machine Tool Structures-Vol.I : Stability Against Chatter*, Pergamon Press.